

Self-organization in systems of anisotropic particles

William Leneal Miller III

Submitted in partial fulfillment of the
requirements for the degree
of Doctor of Philosophy
under the Executive Committee
of the Graduate School of Arts and Sciences

COLUMBIA UNIVERSITY

2012

©2012

William Leneal Miller III

All Rights Reserved

ABSTRACT

Self-organization in systems of anisotropic particles

William Leneal Miller III

This dissertation presents studies on self-organization in soft matter systems. A wide variety of systems is studied, with the goal of understanding both the nonequilibrium and the equilibrium properties of this important process.

In Chapter 2, we study the self-assembly of asymmetric Janus colloidal particles. We identify and systematically describe the effect of the ratio of hydrophobic to hydrophilic surface area on the nonequilibrium processes and structure formation.

In Chapter 3, we examine systems of hard, aspherical particles. We demonstrate that the thermodynamics of self-organization of a system of these aspherical particle (either a system of identical particles or a polydisperse system of different-shaped particles) is well-predicted by a simple relationship between the crystallization pressure and two measures of particle asphericity borrowed from other fields.

In Chapter 4, we shift focus to systems of soft particles in two dimensions and on the surface of a sphere. Soft particles are particles with a finite interaction potential at zero distance; such particles exhibit a surprisingly large variety of ordered structures at equilibrium. A similar phenomenon is seen when the study is extended to soft particles on the surface of a sphere.

In Chapter 5, we study the free energy of two-component polymer brush systems in which polymers of different length are patterned in alternating stripes of specified widths on the surface of a cylinder. We present the dependence of the free energy on the polymer lengths and stripe width and a qualitative explanation of its functional form.

Finally, in Chapter 6, we approach the reverse self-assembly problem. That is, we describe an algorithm for answering the reverse (and much more difficult) question,

“Given a specific desired target self-assembled structure, what interparticle interactions will yield a system which will self-assemble into that structure?” We also describe a new model of interparticle interaction which should be able to generate interparticle interaction geometries with a high degree of flexibility.

Table of Contents

1	Introduction	1
1.1	Soft matter physics	1
1.2	Self-organization	2
1.2.1	Classical nucleation theory	3
1.2.2	Self-assembly and the critical micellar concentration	8
1.3	Exploring “anisotropy space”	11
1.4	Frequently-used numerical methods	12
1.4.1	Measuring crystalline order using spherical harmonics: $\bar{\mathbf{q}}_l$	13
1.4.2	Calculating free energies: thermodynamic integration	14
1.5	Organization of this dissertation	16
2	Self-assembly of asymmetric Janus particles	18
2.1	Introduction	18
2.2	Simulation details	20
2.3	Structure formation	22
2.4	Self-assembly pathways	23
2.5	Conclusions	34
3	Phase behavior of hard aspherical particles	36
3.1	Introduction	36
3.2	A model of hard aspherical particles	37

3.3	Shape-polydisperse systems	40
3.4	Monodisperse systems: coexistence pressures	45
3.5	Monodisperse systems: predicting crystallization	48
3.6	The character of crystals of aspherical particles	51
3.7	Conclusions	54
4	Two-dimensional packing of soft particles on planes and spheres	56
4.1	Introduction	56
4.2	Simulation details	59
4.3	Soft particles in planar geometries	63
4.4	Soft particles on spheres: the soft generalized Thomson problem	67
4.5	Polymers at high density: shortfalls of the Hertzian model	73
4.6	Conclusions	74
5	Free energy of alternating two-component polymer brushes on cylindrical templates	77
5.1	Introduction	77
5.2	Simulation details	79
5.3	One-component systems: $N_2 = 0$	82
5.4	Two-component systems: $N_2 \neq 0$	89
5.5	Conclusions	93
6	Exploiting classical nucleation theory for reverse self-assembly	95
6.1	Introduction	95
6.2	Sampling the interaction shape Ω	100
6.3	Sampling the interaction strength E	101
6.4	Numerical tests	102
6.5	Limitations	105
6.6	Beyond the Kern-Frenkel model	109
6.7	Conclusions	112

List of Figures

1.1	An illustration of a spherical crystal in the presence of a fluid	4
1.2	ΔG vs. r in classical nucleation theory	7
1.3	Anisotropy space	12
1.4	The distribution of q_6 and N_X for liquid, bcc, and fcc systems	15
2.1	Angular dependence of the interparticle potential	22
2.2	Phase diagram for amphiphilic colloidal particles	24
2.3	Radius of gyration vs. aggregate size	26
2.4	Angular probability distribution function between neighboring particles	27
2.5	Snapshots of bilayer formation	29
2.6	Snapshots of cage formation	30
2.7	Probability distribution function of cluster size	31
2.8	Degree of crystallinity of aggregates vs. hydrophobic area	32
2.9	Aggregate size vs. time for $\theta_{\max} = 160^\circ$	33
3.1	Model particles for different values of σ_0 and N_b	39
3.2	A and q distributions for different values of σ_0 and N_b	43
3.3	Coexistence pressures for shape-polydisperse systems vs. Aq	44
3.4	Coexistence pressure vs. Aq for monodisperse systems of aspherical particles	46
3.5	Crystallizability of monodisperse aspherical particles vs. A and q	49
3.6	Rotational and translational diffusion for aspherical particles	52

4.1	Rescaled potential $\frac{V(r)}{\varepsilon}$ for the three values of α used in this study	61
4.2	Temperature vs. number density for $\alpha = \frac{5}{2}$	63
4.3	Temperature vs. number density for $\alpha = \frac{3}{2}$ and $\alpha = \frac{7}{2}$	65
4.4	Two-dimensional crystal phases formed in these systems	66
4.5	Energy density difference between hexagonal and square lattices vs. α	68
4.6	Snapshots of soft particles on a spherical surface	70
4.7	Global minima for small numbers of particles on a sphere, $\alpha = \frac{3}{2}$	71
4.8	Global minima for small numbers of particles on a sphere, $\alpha = \frac{5}{2}$	72
4.9	Phase diagrams of different models of polymers tethered to colloids	75
5.1	Snapshots of initial and equilibrium configurations for $L_p = 6$ and $L_p = 30$	81
5.2	Free energy and α as a function of L_p	84
5.3	Sketch of expected chain configurations for $L_p = 1, 2, and } 4$	87
5.4	α vs. the rescaled $\frac{L_p}{h_B}$	90
5.5	α vs. the rescaled $\frac{L_p}{h_B}$ for different values of N_2	91
6.1	Generic self-assembly diagram for patchy spherical particles	98
6.2	Force vs. θ for square cubic and 2D square crystals	104
6.3	MC trajectories in interaction space for the design of simple cubic crystals	106
6.4	Phase diagrams for simple cubic and 2D square crystals	107
6.5	F vs. θ for different values of the order parameter q_{cut}	109
6.6	Illustration of the structure of the <i>Adaptive Pixel Model</i>	111

Acknowledgments

First, I would like to thank my advisor, Prof. Angelo Cacciuto, for giving me the honor of being his first graduate student and being a never-ending source of ideas and knowledge. Angelo always encouraged me to work hard and tackle interesting problems with his enthusiasm and support; working with him has been a pleasure, and I honestly can't imagine a better mentor. I hope that this dissertation will effectively convey the exciting work we did together.

I am also grateful to my defense committee: Prof. Bruce Berne and Prof. David Reichman, who have served on my graduate committee for the past five years and provided insightful feedback on my second-year defense and original research proposal, and, along with Prof. Luis Campos and Prof. Sanat Kumar, have taken the time out of their incredibly busy schedules to read my dissertation and attend my defense.

Scientific research is a collaborative effort, and I have benefited from exceptional collaboration with other members of the Cacciuto group. In particular, I had the privilege of working extensively with Dr. Behnaz Bozorgui Katherine Klymko, Dr. Josep Pàmies, and Maya Sen. I would also like to thank Leo PeBenito and Clarion Tung, with whom my collaboration has been less direct but no less valuable, and especially Andela Šarić – for large parts of the past four years, the two of us have *been* the Cacciuto group.

I would like to thank my many friends here at Columbia. They made graduate school much more enjoyable, and I wish them all the best as they transition from school to the real world.

I want to express my sincere gratitude to my family. They have always been my strongest supporters, and have always been there for me unconditionally; my academic success would not have been possible without the encouragement my parents have given me since I was a child.

Finally, of course, I am thankful to Christine Vanos. Graduate school isn't easy, but she made it much easier, and I'm looking forward to spending the rest of my life with her.

William L. Miller

For my family

Chapter 1

Introduction

1.1 Soft matter physics

Broadly speaking, the results presented in this dissertation involve those physical systems in which nontrivial collective behavior emerges from the competition among hydrophobicity, entropy, and elasticity. These systems are a subset of the broad field of soft matter physics, also referred to as complex fluids. In general, soft matter physics revolves around materials in which their constituents have a size in the range 10 nm – 1 μm , their dynamics are mostly diffusive, and thermal fluctuations play an important role – that is, the relevant energy scales of important physical behaviors of these systems are comparable with the thermal energy at room temperature: roughly 0.6 $\text{kcal}\cdot\text{mol}^{-1}$. I will be primarily concerned with colloids and polymers; other systems such as liquids, gels, and biological materials (such as membranes) are also included in this field.

Soft materials exhibit a number of characteristics not seen in “hard” condensed matter. One of the most important is the formation of mesoscopic structures, which are intermediate in scale between the individual components (e.g. colloids or polymers) and the bulk, macroscopic system. Soft matter systems also tend to undergo large fluctuations due to their relatively low energy density, and their most interest-

ing equilibrium properties tend to be dominated by entropy rather than energy. The result is that soft matter systems often exhibit unique behaviors which are difficult to predict.

An example of such complicated dynamics is in the crystallization of binary systems of hard colloids; that is, systems containing hard, purely repulsive spheres of two different sizes [1]. Because these particles cannot overlap and interact only via their hard repulsions, the energy in such systems is by definition zero. However, a wide range of three-dimensional crystalline structures is found, depending on the relative sizes and concentrations of the two components; these interesting effects must necessarily be due solely to the configurational entropy of the system.

Over the last fifty years, a large effort has been devoted to establishing the theoretical and numerical tools with which to characterize and predict the phase behavior of complex fluids. Most studies have focused on systems where the effective interactions between the main components are solely dependent on the interparticle separation. However, recent advances in synthesis of nanoparticles [2–9] have allowed for unprecedented control over the shape and surface chemistry of colloidal particles; it has also become feasible to engineer interactions between star polymers or dendrimers by controlling their overall chemical and topological properties [10]. The result is an unlimited number of potential building blocks whose organization, either from a dilute fluid by aggregation due to interparticle attractions or from a dense fluid by an externally-applied pressure, have the potential to form a large variety of structures with novel functional, mechanical, and optical properties.

1.2 Self-organization

This dissertation deals with the process by which these mesoscopic and/or the full macroscopic structures form. The work presented is the result of Monte Carlo and molecular dynamics simulations on a wide variety of systems representing a small

subset of the variety described above, directed at studying the ways in which the details of interparticle interactions affect how self-organization occurs.

This self-organization of structures can be considered as divided between two broad situations: formation of macroscopic structures, which can be modeled by classical nucleation theory, and aggregation into mesoscopic structures, which is described in the framework of self-assembly theory.

1.2.1 Classical nucleation theory

Although the generic features of particle aggregation can be described, at least phenomenologically, in terms of simple thermodynamic arguments [11–15], the details of the self-organization process are far from being understood, even in the simple case of aggregation of isotropic particles into macroscopic three-dimensional crystals. For more complex particles, it is difficult to predict, *a priori*, the equilibrium self-assembled state, and, even more interestingly, the nonequilibrium pathways associated with it. [16].

The thermodynamics of crystal formation can be described, to a first approximation, within the framework of classical nucleation theory (CNT). In this theory, the nucleation and eventual crystallization of a system is described as a simple interplay between two competing thermodynamic forces; however, it includes some fairly severe approximations which make it applicable only for a qualitative understanding of the process.

Consider a system of N particles interacting via some potential. Within this system is a roughly spherical nucleus of n crystalline particles surrounded by a fluid of the remaining $(N - n)$ particles (note that for small n , the approximation of a spherical shape is a poor one). Figure 1.1 shows an illustration of this system. There are two major contributions to the free energy of this nucleus: the free energy gain associated with the formation of the more stable crystal phase, and the free energy cost due to the interface between the fluid and the solid phase. Below I will focus on

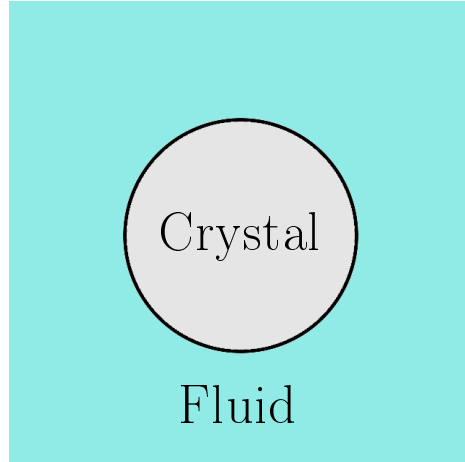


Figure 1.1: An illustration of the system considered in classical nucleation theory; a spherical crystal embedded in a fluid phase. The dark border indicates the interface.

these two terms in more detail.

For a typical scenario of a system of particles interacting via a short-ranged attractive potential, at sufficiently large density ρ , the free energy associated with the growth of the crystal is favorable because the chemical potential difference, $\Delta\mu$, between the fluid and crystalline phases becomes negative. The condition that $\Delta\mu < 0$ is generally due to a combination of several factors; the most obvious contribution is a direct consequence of favorable interparticle energetics. A particle in a crystal has, on average, more neighbors than one in the fluid, and thus, crystallization leads to an energy gain. However, a favorable $\Delta\mu$ may also arise in systems featuring purely repulsive interparticle interactions, and the origin of this effect is more subtle.

For illustration, consider a system of hard spheres. These particles interact via the potential

$$V = \begin{cases} \infty & \text{if } r < r_0 \\ 0 & \text{otherwise} \end{cases}, \quad (1.1)$$

where r is the distance between particles and r_0 is the particle diameter; therefore, as in the example system discussed in Section 1.1, their phase behavior is completely

determined by their configurational entropy – the interaction energy within such a system is by definition always zero. However, very early computer simulations [17, 18] showed that even these simple systems showed a transition from a fluid to a stable, face-centered cubic (fcc) crystal.

The existence of a stable crystalline phase for hard spheres implies that beyond some density ρ , the configurational entropy of the ordered, crystalline phase is higher than that of a disordered phase. However, intuition and a simple consideration of the system neglecting the correlation between particles due to their excluded-volume (repulsive) interactions in the hard sphere system leads one to the conclusion that the disordered phases is higher in entropy at every density. This indicates that excluded-volume effects must be vital for this transition, and indeed, it is clear that such effects must be important at high ρ .

At high enough density ρ , the disordered fluid phase becomes over-compressed – the particles can no longer easily diffuse past each other and the system becomes stuck in a disordered but “jammed” state. The key to understanding the existence of the crystalline state of hard spheres then is that the amount of free volume available to each particle in a fcc crystal is larger than that available to each particle in an over-compressed fluid. Each particle in the crystal is therefore a bit freer to move than the particles in the disordered fluid – and so the system has a slightly higher configurational entropy.

Thus, even in purely repulsive systems such as hard spheres, when the density ρ is large enough, the free energy of crystallization, $\Delta\mu$, is negative, due to the gain in configurational entropy upon self-organization.

This negative $\Delta\mu$ results in a linear decrease of the Gibbs free energy with the number of crystalline particles in the interior of the nucleus; for large-enough spherical nuclei, it is approximately

$$\Delta G_\mu(r) \simeq \frac{4}{3}\pi r^3 \rho \Delta\mu, \quad (1.2)$$

where r is the radius of the nucleus and ρ is the crystal density. The chemical poten-

tial difference $\Delta\mu$ can easily be determined numerically; however, what is important for this qualitative understanding of classical nucleation is that in order for crystal nucleation to occur, $\Delta\mu$ must be negative.

The second major term in the full free energetic description of crystal nucleation is the free energy cost associated with the creation of an interface between the crystal nucleus and the fluid phase. One can think of this term as arising from the loss of entropy of a particle bound to the surface versus one in the fluid, without benefit of a full complement of favorable interactions with neighbors (for attractive particles) or the full configurational entropy gain of increased free volume (for purely repulsive ones) experienced by a particle in the interior. It is described by the surface tension γ , a quantity the value of which, like $\Delta\mu$, is unimportant for our purposes except that it must be positive. The interfacial free energy is then the product of the surface area times the surface tension

$$\Delta G_\gamma(r) = A\gamma = 4\pi r^2\gamma. \quad (1.3)$$

We thus find the total Gibbs free energy of the crystal nucleus, as a function of the nucleus size r ,

$$\Delta G \simeq \frac{4}{3}\pi r^3\rho\Delta\mu + 4\pi r^2\gamma. \quad (1.4)$$

Taking the derivative of this quantity and setting the result equal to zero, a local maximum in the free energy is located at

$$r^* \simeq \frac{2\gamma}{\rho|\Delta\mu|}, \quad (1.5)$$

or, in terms of the number of particles in the cluster,

$$n^* \simeq V_c\rho \simeq \frac{4}{3}\pi (r^*)^3 \rho \simeq \frac{32\pi}{3\rho} \left(\frac{\gamma}{|\Delta\mu|}\right)^3. \quad (1.6)$$

This is termed the “critical nucleus size”, and represents a transition point: 50% of particles of size r^* would be expected to melt back to the fluid phase, and 50% would be expected to grow into very large crystals. In fact, in this approximation,

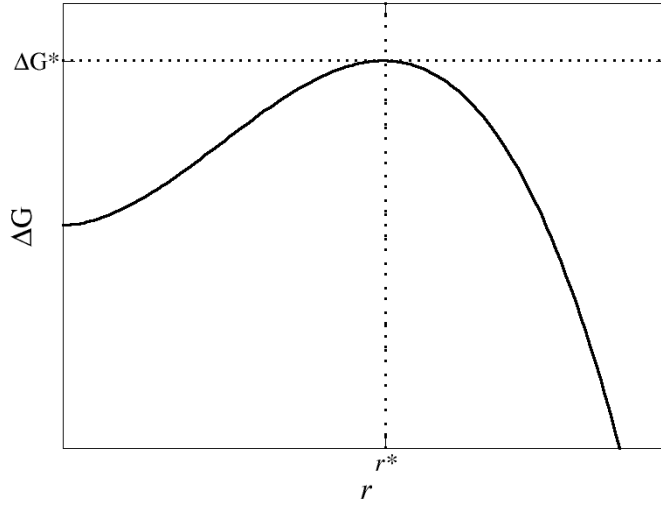


Figure 1.2: A plot of ΔG vs. r for a crystal nucleus surrounded by a fluid. The critical nucleus is at the point where the dotted lines, indicating ΔG^* and r^* , cross.

nuclei larger than r^* would be expected to grow until they included every particle in the system.

Plugging the critical radius r^* into the expression for ΔG derived above yields the free energy cost of the critical nucleus,

$$\Delta G^* \simeq \frac{16\pi\gamma^3}{\rho^2\Delta\mu^2}. \quad (1.7)$$

An illustration of the form of this free energy landscape is plotted in Figure 1.2.

In order for large, crystalline aggregates to form via classical nucleation, a balance must be achieved in ΔG^* ; because the rate of crystal nucleation $\tau \propto e^{-\beta\Delta G^*}$ (where $\beta \equiv (k_B T)^{-1}$), if it is too large, a critical nucleus will not be observed over experimentally relevant timescales, and thus the barrier will never be crossed in practice. However, if ΔG^* is too small, several critical nuclei will occur throughout the system. While it may be possible for these disparate nuclei to coalesce into a single large crystalline cluster, the segregation of the system into several small clusters can make it more difficult for a large cluster to form.

In general, the handles by which we can affect ΔG^* , as expressed in equation 1.7, are indirect and through $\Delta\mu$ and γ – in particular, their values will depend on the temperature and concentration of the surrounding fluid, and these parameters can in principle be adjusted by altering the position in $\rho - T$ phase space so that ΔG^* will have some “optimal” value at which one crystal will form on an experimentally-accessible time scale. Chapter 6 explores other methods for adjusting ΔG^* .

Finally, a comment regarding the problems with the approximations involved with CNT. As briefly mentioned above, the assumption of a spherical nucleus breaks down for small nuclei; furthermore, the substitution of $n = \frac{4}{3}\pi r^3\rho$ relies on the nucleus being large and homogeneous, and the surface tension γ may have a weak dependence on the curvature of the surface and thus the size of the nucleus.

One last important assumption that is made in CNT and is not necessarily valid for any system is that the symmetry of the crystalline nucleus is the equilibrium structure of the final macroscopic crystal. For example, the equilibrium structure of a crystalline hard sphere system is fcc; however, during the nucleation process, the forming nucleus contains other crystal structures; particularly, a not-insignificant fraction of hexagonal close-packed (hcp) defects, in a structure referred to as random-stacked close-packed (rhcp) [19].

1.2.2 Self-assembly and the critical micellar concentration

Classical nucleation theory deals with the formation of macroscopic crystals from a fluid phase; when systems form several finite-sized mesoscopic structures, a different theoretical framework becomes more appropriate. Several biological structures are formed in this way, including viral capsids and biological membranes.

For example, biological membranes are formed by self-assembly of lipids: amphiphilic molecules with hydrophilic head groups and hydrophobic tails consisting of hydrocarbon chains. When these molecules are placed in water, the hydrocarbon tails will aggregate together due to their hydrophobicity, forming specific structures.

Amphiphilic molecules tend to be shaped roughly like a truncated cone, with the hydrophilic head group representing the base of the cone and the hydrocarbon tails representing the tip – thus, when they self-assemble, they can form various shapes depending on their aspect ratio, $\xi = \frac{V}{ah}$, where V , a , and h are the volume, base area, and height of this cone, respectively. When $\xi = \frac{1}{3}$ (a cone) the equilibrium structure is a sphere, and when $\xi = 1$ (a cylinder), a lamellar, planar structure is formed. These lamellar structures can then stack, with their hydrophobic surface facing each other, to form planar bilayers. When ξ is slightly less than 1, these bilayers curve and can loop back on themselves, forming vesicles with hydrophobic surfaces on both the exterior and interior; values of ξ between $\frac{1}{3}$ and 1 form various non-spherical micelles.

Self-assembly of micellar structures sets in at a defined concentration of monomers known as the critical micellar concentration (cmc), c^* . It can be approximately calculated as follows.

Consider a system of N lipids in a volume V . They self-assemble into aggregates of size α , defined as the number of molecules in the aggregate; the number of molecules in aggregates of size α is N_α , and the number of such aggregates is $n_\alpha = \frac{N_\alpha}{\alpha}$. The partition function for non-interacting micelles is given by

$$Q^{(\text{id})} = \prod_{\alpha=1} N \frac{1}{n_\alpha!} \left(\frac{V q_\alpha^{\text{int}}}{\Lambda_\alpha^3} \right)^{n_\alpha}, \quad (1.8)$$

where q_α^{int} is the internal partition function of an aggregate of size α . Given this, the chemical potential per lipid molecule in an aggregate of size α is

$$\mu_\alpha = \frac{k_B T}{\alpha} \ln \left(\frac{x_\alpha}{\alpha} \right) + \epsilon_\alpha, \quad (1.9)$$

where $x_\alpha = \frac{N_\alpha}{N}$ is the mole fraction of the lipids that belong to aggregates of size α and $\epsilon_\alpha = -\frac{k_B T}{\alpha} \ln \left(\frac{q_\alpha^{\text{int}} v}{\lambda_\alpha^3} \right)$, where v is the volume per lipid molecule.

If all aggregates are in equilibrium, then all of these chemical potentials are equal, $\mu_\alpha = \mu$ for all α . Then

$$x_\alpha = \alpha x_1^\alpha e^{(\alpha(\epsilon_1 - \epsilon_\alpha)/k_B T)}, \quad (1.10)$$

where k_B is the Boltzmann constant ($k_B \simeq 1.38 \times 10^{-23} \text{ J} \cdot \text{K}^{-1}$) and T is the system temperature.

The cmc, x_c , is defined as the mole fraction at which the total mole fraction of aggregates with $\alpha \geq 2$ is equal to x_1 ,

$$\sum_{\alpha \geq 2} x_\alpha = x - x_1 = x_1. \quad (1.11)$$

If the geometry of the lipids is such that a micelle of a specific size α^* is favored, then ϵ_α will have a minimum at that value $\alpha = \alpha^*$, so that $\frac{\partial \epsilon_{\alpha^*}}{\partial \alpha} = 0$.

$$\sum_{\alpha \geq 2} x_\alpha \simeq x_{\alpha^*} = x_1 = \frac{x_c}{2}. \quad (1.12)$$

Subsituting Equation 1.10 into Equation 1.12 yields an expression for the cmc,

$$x_c \simeq 2e^{\beta(\epsilon_{\alpha^*} - \epsilon_1)}. \quad (1.13)$$

This is the approximate mole fraction at which half of the lipid molecules in the system are members of an aggegrate of size α^* .

It is important to note that the calculation of the cmc considers only thermodynamic factors, and does not consider kinetic ones at all. If most of the particles in the system are members of aggregates, the primary process by which large aggregates form from smaller ones is Ostwald ripening, which requires the dissolution of a smaller aggregate followed by the deposition of its component particles on the surfaces of others.

However, if the equilibrium aggregate size is α^* , there will be some range of aggregate sizes smaller than α^* for which the free energy of the aggregates is lower than the free energy of individual particles. Thus, the dissolution of these aggregates incurs a free energetic penalty; it is possible for the system to become trapped in a metastable state in which some or all of the aggregates in the system are smaller than the equilibrium size α^* , because these aggregates will not dissolve to allow for the growth of others over experimentally accessible timescales.

1.3 Exploring “anisotropy space”

Whether we are considering aggregation of particles into macroscopic three-dimensional crystals or finite-sized clusters, the shape and the interaction patterns between the single components greatly affects the structure of the final aggregates.

The advances in particle synthesis mentioned above have led to the opening of a vast, multidimensional space of particle anisotropy. In order to fully explore the possibilities for self-organization in this new space, exploration outside of the traditional $\rho - T$ phase diagram is required. Following Glotzer and Solomon [20], I will refer to this multidimensional phase space as “anisotropy space”.

Every chapter of this dissertation, and indeed much of the work in the field of soft matter physics, can be thought of as exploration along one or more axes in anisotropy space. For example, in Chapter 2, we explore the axis of degree of hydrophobicity in a system of asymmetric Janus particle, from 0% (purely repulsive spheres) to 100% (particles with an isotropic attractive potential). In Chapter 3, we introduce two anisotropy axes, labeled A and q , which allow us to characterize aspherical particles with respect to purely isotropic hard spheres.

Most work in this field involves exploration of the forward self-organization problem; that is, one or more axes of anisotropy are chosen, and the effect of that anisotropy on the behavior of systems of those particles is determined. Chapter 6 attempts to address the reverse problem: given a defined set of anisotropy axes (in this case, interaction energy and patch size), this work attempts to find the region or regions in phase space which will yield desired system behavior, such as self-organization into a specified target structure.

In principle, anisotropy space is infinite; even the region of anisotropy space accessible by current particle synthesis methods (or found in nature) is very large. Thus, an important part of the challenge in exploring this space is identifying which regions of the space are both experimentally accessible and likely to yield nontrivial results. In the case of this dissertation, “nontrivial results” generally means crystallization that

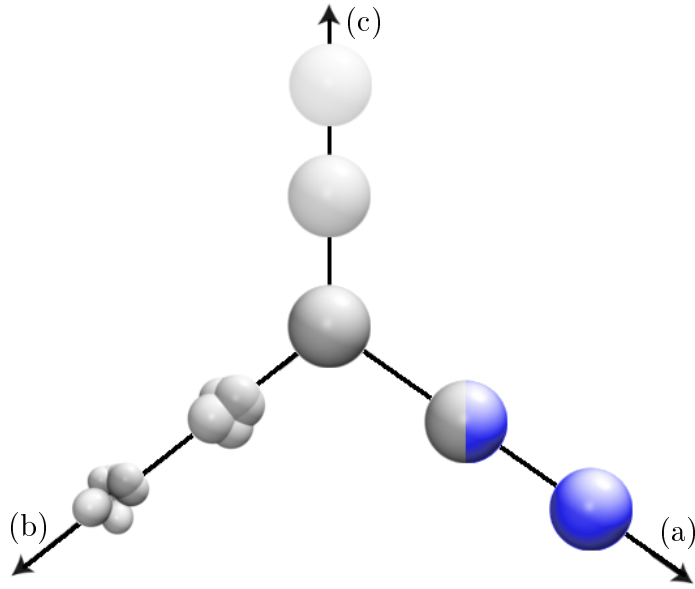


Figure 1.3: An illustrated example of anisotropy space, with a hard sphere as the origin (“zero anisotropy”) and axes of (a) degree of hydrophobicity (Chapter 2), (b) asphericity (Chapter 3), and (c) softness (Chapter 4) (figure adapted from Glotzer and Solomon [20]).

in some way differs (for example, in thermodynamics, mechanism, or crystal structure) from that of the relevant isotropic reference – most often, some approximation of a hard sphere.

1.4 Frequently-used numerical methods

In this section, I will briefly describe two methods that are used frequently throughout this work. First, a method by which crystalline order can be differentiated from the surrounding fluid will be discussed; next, an algorithm for calculating free energy differences with respect to a reference state is demonstrated.

1.4.1 Measuring crystalline order using spherical harmonics:

$$\bar{\mathbf{q}}_l$$

The crystallinity of a system can be measured quantitatively using a local bond-order parameter originally introduced by Steinhardt *et al.* [21] and used, for example, in [22, 23] and many others. This method uses l -fold symmetric spherical harmonics to numerically differentiate crystal structures of that symmetry (most commonly, $l = 6$, so that body-centered cubic [bcc], fcc, or hcp structures are detected) from the fluid.

For a given particle i , we define $q_l(i)$ as follows:

$$q_l(i) = \left(\frac{4\pi}{13} \sum_{m=-l}^l |q_{lm}(i)|^2 \right)^{1/2}, \quad (1.14)$$

where

$$q_{lm}(i) = \frac{1}{N_b(i)} \sum_{j=1}^{N_b(i)} Y_{lm}(\hat{\mathbf{r}}_{ij}) . \quad (1.15)$$

The sum in this equation is over all neighboring particles j of particle i , where a particle is defined as “neighboring” if it is within some cutoff r_q of particle i ; $N_b(i)$ is the number of such neighboring particles to particle i . $Y_{lm}(\hat{\mathbf{r}}_{ij})$ is the m -component spherical harmonic evaluated for the normalized vector $\hat{\mathbf{r}}_{ij}$ from particle i to particle j .

This parameter, $q_l(i)$, is sensitive to the degree of orientational correlations between vectors joining neighboring particles – in a fluid, there are no preferred orientations and so the correlations decay rapidly, whereas in a crystal, the vectors are strongly correlated. We can thus calculate a quantitative measure of the degree of crystallinity, and define two particles as “connected” within a crystalline structure if the correlation between neighboring particles,

$$\mathbf{q}_l(i) \cdot \mathbf{q}_l(j) = \sum_{m=-l}^l q_{lm}(i) \cdot q_{lm}^*(j), \quad (1.16)$$

is greater than some cutoff value q_{cut} . Alternatively, the values of $\mathbf{q}_l(i) \cdot \mathbf{q}_l(j)$ can be averaged, for each particle i , over all neighbors j , yielding a single value $\bar{q}_l(i)$ –

comparing the result to a cutoff q_{cut} allows particle i to be defined as “crystalline” or “non-crystalline.” The number of connected particles to particle i is denoted $N_X(i)$. Figure 1.4 shows distributions of q_6 , q_4 , and N_X values in liquid, bcc, and fcc systems, in order to illustrate the power of these measures for delineating crystalline vs. noncrystalline systems.

This order parameter will be used extensively throughout this dissertation. In most cases, the six-fold symmetric q_6 will be used; in Chapter 6, q_4 is used, and some comments will be presented on the use of q_4 and q_6 values to differentiate between crystals of four- and six-fold symmetry.

1.4.2 Calculating free energies: thermodynamic integration

It is often desirable to compute the free energy of a system with respect to some reference. One method for doing so, and the one that will be used in this dissertation (particularly, Chapter 5), is thermodynamic integration [25].

The Helmholtz free energy, F , is related to the canonical partition function Q as follows:

$$\begin{aligned} F &= -k_B T \ln Q(N, V, T) \\ &\equiv -k_B T \ln \left(\frac{\int d\mathbf{p}^N d\mathbf{r}^N \exp[-\beta \mathcal{H}(\mathbf{p}^N, \mathbf{r}^N)]}{\Lambda^{dN} N!} \right), \end{aligned} \quad (1.17)$$

where \mathcal{H} is the Hamiltonian of the system; \mathbf{p} and \mathbf{r} are the momenta and positions of all particles in the system, respectively; d is the dimensionality; N is the number of particles; V is the volume; T is the temperature; and the thermal de Broglie wavelength $\Lambda \equiv \frac{\hbar}{\sqrt{2\pi m k_B T}}$.

Assume that we can write the potential energy in a three-dimensional system, V_λ , as a linear function of some coupling parameter λ , such that for $\lambda = 0$, V_λ equals some reference potential V_{ref} , and for $\lambda = 1$, V_λ equals the potential of interest V :

$$V_\lambda = (1 - \lambda)V_{\text{ref}} + \lambda V = V_{\text{ref}} + \lambda(V - V_{\text{ref}}). \quad (1.18)$$

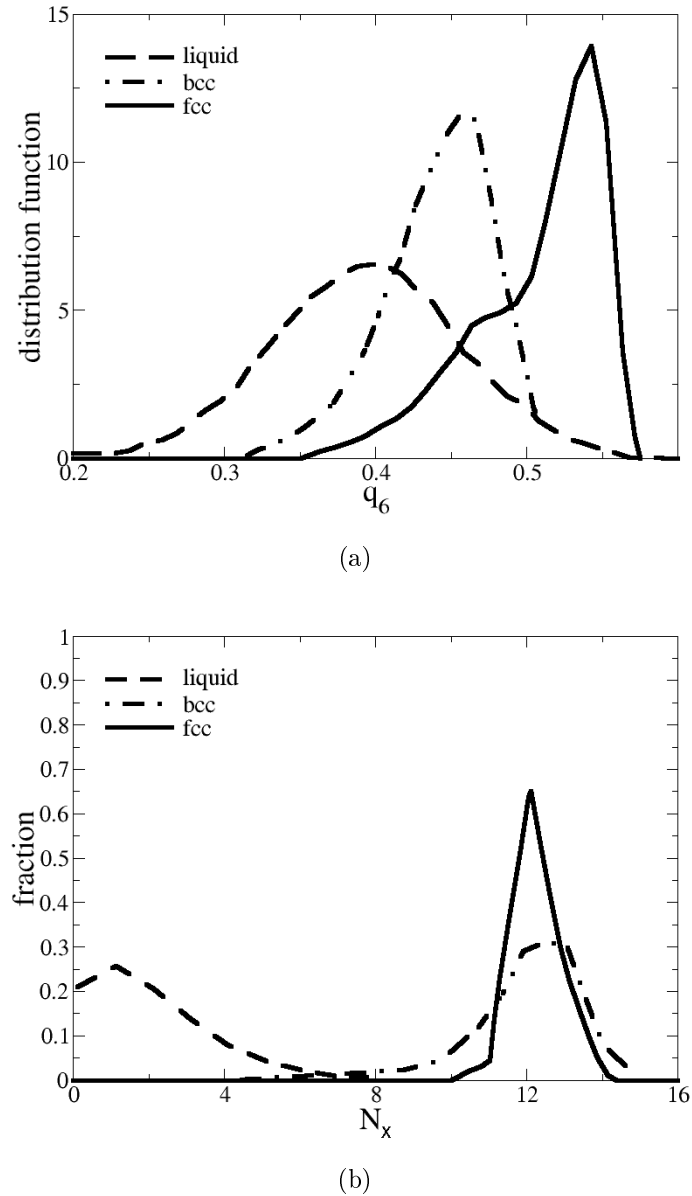


Figure 1.4: The distribution of (a) q_6 and (b) N_X for liquid, bcc, and fcc systems (figures created from data in ten Wolde *et al.* [24]). While the q_6 values are different for the three systems, note that the number of connections N_X is the strongest distinguisher between crystalline and noncrystalline systems, due to the fact that it accounts for relative orientation between neighboring particles.

Then, for a given value of lambda, the partition function $Q(N, V, T, \lambda)$ is given by

$$Q(N, V, T; \lambda) = \frac{1}{\Lambda^{3N} N!} \int d\mathbf{r}^N e^{-\beta V_\lambda}. \quad (1.19)$$

The derivative of F with respect to λ can then be written

$$\begin{aligned} \left(\frac{\partial F(\lambda)}{\partial \lambda} \right)_{N,V,T} &= -\frac{1}{\beta} \frac{\partial}{\partial \lambda} \ln Q(N, V, T; \lambda) \\ &= \frac{\int d\mathbf{r}^N \left(\frac{\partial V_\lambda}{\partial \lambda} \right) e^{-\beta V_\lambda}}{\int d\mathbf{r}^N e^{-\beta V_\lambda}} \\ &\equiv \left\langle \frac{\partial V_\lambda}{\partial \lambda} \right\rangle_\lambda, \end{aligned} \quad (1.20)$$

where the notation $\langle \dots \rangle_\lambda$ is used to denote the ensemble average for a system with potential energy function V_λ .

The energy difference between the system with the potential of interest V and the reference system with potential V_{ref} can then be found by integrating

$$\Delta F \equiv F(\lambda = 1) - F(\lambda = 0) = \int_{\lambda=0}^{\lambda=1} d\lambda \left\langle \frac{\partial V_\lambda}{\partial \lambda} \right\rangle_\lambda. \quad (1.21)$$

Thus, the free energy difference ΔF can be calculated by integrating a derivative of the readily accessible quantity, the total potential, with respect to λ . In practice, this is done by sampling at several values of $\lambda \in [0, 1]$ and integrating numerically.

1.5 Organization of this dissertation

This dissertation is organized as follows.

In Chapter 2, we discuss the self-assembly of particles with partially hydrophobic and partially hydrophilic surfaces, and determine the effect of the ratio of the two areas. It is based on work published in [26].

Chapter 3 presents studies of the thermodynamics of crystallization in systems of aspherical particles, and identifies order parameters via which the crystallization coexistence pressure can be predicted. It is based on work published in [27] and [28].

A study of the packing of soft particles in two dimensions is presented in Chapter 4. A few different soft interaction potentials are considered and a wide variety of crystalline structures of different overall symmetry result. It is based on work published in [29].

Chapter 5 contains the results of a study of two-component polymer brushes grafted to cylinders in alternating stripes. The dependence of the free energy on stripe width and the lengths of the polymers is considered. It is based on work published in [30].

Finally, in Chapter 6, we present an algorithm for the reverse self-assembly problem; that is, the determination of an optimal interaction potential given a desired target crystal structure. We speculate possible expansions of the method and present a new model for interparticle interaction that should allow a great deal of flexibility in such algorithms. It is based on work published in [31].

Chapter 2

Self-assembly of asymmetric Janus particles

2.1 Introduction

Spontaneous assembly of components into large ordered aggregates is a ubiquitous phenomenon in nature, and is observed across all length scales. Aggregation of proteins into functional nanomachines [32], formation of viral capsids [33, 34], packing of phospholipids into biological membranes [35] and assembly of colloidal particles into macroscopic crystals [36] are just a few manifestations of this fundamental process. Because of advances in particle synthesis [2–6], it is now possible to produce colloidal particles that are anisotropic both in shape and surface chemistry, thus providing an unlimited variety of building blocks that can spontaneously assemble into an unprecedented number of structures holding promise for the development of materials with novel functional, mechanical, and optical properties.

Janus particles are spherical colloidal particles the surfaces of which have one hydrophobic and one hydrophilic hemisphere. In aqueous solution, the effect of this surface anisotropy is to introduce an attraction between hydrophobic hemispheres of neighboring particles and a simple hard-sphere repulsion between the hydrophilic

ones. Janus particles are important because they represent what is probably the simplest model for the study of the role of surface anisotropy in colloidal aggregation.

The self-assembly pathway of Janus particles has been described in some detail [16] both experimentally and numerically. What was found is a rich behavior in terms of both the dynamics of self-assembly, and the final structure of the aggregates. Specifically, by tuning the repulsion between the hydrophilic hemispheres, one can drive the system into two distinct phases: one in which particles form a gas of small clusters composed of four to thirteen particles, and another, at large salt concentration (screening Coulombic interactions), in which particles organize into long, branched, worm-like structures formed by cooperative fusion of the small clusters. Such particles are a particular type of a wider class of patchy particles, the self-assembly of a wide variety of which has been studied previously [20, 37].

Inspired by these experimental results, in this paper we go one step further and explore the dynamics and structure formation of anisotropic amphiphatic particles. While the dividing surface between hydrophobic and hydrophilic regions in Janus particles is set at the equator, herein particles in which this boundary is located at an arbitrary latitude on the particle’s surface are considered, and the self-assembly of these particles, as a function of the size of the hydrophobic region, is systematically studied. We thus explore a key “anisotropy dimension” (as discussed in Section 1.3) as related to the self-assembly of these particles.

This system is quite interesting because one can easily predict the formation of a wealth of different structures as a function of the location of the dividing surface. For instance, we know that when the hydrophobic region covers a very small area, particles can only assemble into dumbbells (pairs of particles with hydrophobic patches pointing toward each other). We know that when the dividing surface is placed to slightly larger values, so that more particles can share the same hydrophobic surface, particles condense into small stable clusters. We also know the structures resulting from self-assembly of Janus particles, and of course, in the limit of full coverage, we

recover an isotropic potential which is known to lead to the formation of a fcc crystal.

Using this simple system we can systematically study the formation of aggregates whose structure ranges from zero dimensions (dumbbells and meso-particles) to three dimensions (fcc crystals), and we can analyze how the specificity of the local inter-particle interactions correlates to the final self-assembled structure and its dynamics.

2.2 Simulation details

The amphiphilic character of the particles studied herein is modeled via an interaction potential that depends on both the separation between particle surfaces and the angle between particle axes, so that a precise shape and extent of the interaction may be defined. Our choice of the interaction potential is inspired by the model introduced in [16], which has been used to analyze actual experimental data of Janus Particles.

The potential presented in [16] was specifically tailored to describe the physical properties of Janus particles at different salt concentrations, ρ_s . At low and intermediate salt concentrations, the repulsion between the charged hemispheres constrains particles to interact head-on, with angular deviations that depend in a nontrivial way on ρ_s . However, the more interesting structure formation (worm-like clusters) appears at large salt concentrations, where the role of electrostatic interactions becomes negligible. In this limit, particles can freely rotate, once in contact, within the boundaries of the hydrophobic regions. These regions can therefore be appropriately described by a short-ranged, isotropic attractive potential that acts within the boundaries of that region. Similarly, the hydrophilic region is well-characterized by a simple short-ranged repulsive interaction.

Because we desire to study the dynamics of self-assembly, molecular dynamics (MD) simulations were used. MD simulations require smooth potentials (ensuring finite forces), and thus simple square-well potentials are not amenable to this type of simulation – the potential used are essentially smoother versions of these simple

square-well potentials.

The potential used in our paper reflects the phenomenological behavior described above and has the following form:

$$V(r, \theta_1, \theta_2) = V_{\text{rep}}(r) + V_{\text{att}}(r)\phi(\theta_1)\phi(\theta_2), \quad (2.1)$$

where r is the distance between particles, θ_1 is the angle between the axis of particle 1 and the axis between particle centers, and θ_2 is the analogous angle for particle 2. $V_{\text{rep}}(r)$ is a symmetric repulsive interaction that accounts for the particle excluded volume, and has the form of a shifted-truncated Lennard-Jones potential:

$$V_{\text{rep}}(r) = \begin{cases} 4\epsilon_0 \left[\left(\frac{\sigma}{r}\right)^{12} - \left(\frac{\sigma}{r}\right)^6 + \frac{1}{4} \right] & r \leq 2^{\frac{1}{6}}\sigma \\ 0 & r > 2^{\frac{1}{6}}\sigma \end{cases}. \quad (2.2)$$

$V_{\text{att}}(r)$ accounts for the attraction between the hydrophobic *surfaces* on the particles. If $r_s = |r - \sigma|$ is the distance between the particle surfaces,

$$V_{\text{att}}(r) = 4\epsilon \left[\left(\frac{\sigma/2}{r_s + \sigma/2 \times 2^{1/6}} \right)^{12} - 2 \left(\frac{\sigma/2}{r_s + \sigma/2 \times 2^{1/6}} \right)^6 \right], \quad (2.3)$$

and it extends up to $r = 1.5\sigma$. Finally, $\phi(\theta)$ is a smooth step function that modulates the angular dependence of the potential, and is equal to 1 within the region $\theta \leq \theta_{\text{max}}$ and decays to zero following the expression $\cos^2 \left(\pi \left[\frac{\theta - \theta_{\text{max}}}{2\theta_{\text{tail}}} \right] \right)$ at the tail of the angular range, i.e when $\theta_{\text{max}} \leq \theta \leq \theta_{\text{max}} + \theta_{\text{tail}}$ (with $\theta_{\text{tail}} = 10^\circ$). This particular value of θ_{tail} has been selected to generate a sufficiently smooth potential at the Janus interface to allow MD simulation with reasonable time steps. See Figure 2.1 for an illustration of $\phi(\theta)$.

$$\phi(\theta) = \begin{cases} 1 & \theta < \theta_{\text{max}} \\ \cos^2 \left(\pi \left[\frac{\theta - \theta_{\text{max}}}{2\theta_{\text{tail}}} \right] \right) & \theta_{\text{max}} \leq \theta \leq \theta_{\text{max}} + \theta_{\text{tail}} \\ 0 & \text{otherwise} \end{cases} \quad (2.4)$$

The parameters set in our model are compatible with colloidal particles of size 200–400 nm in aqueous solution kept at a salt concentration sufficiently large to screen the electrostatic repulsion between the hydrophilic regions of any two particles [16].

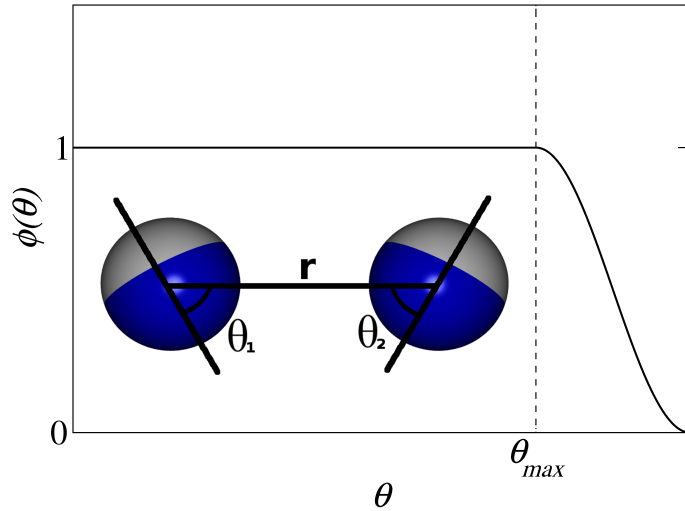


Figure 2.1: Sketch of the angular dependence of the inter-particle potential $\phi(\theta)$. The dark side represents the hydrophobic region and the light side represents the hydrophilic.

The system is evolved using molecular dynamics simulations with a Langevin thermostat at constant room temperature, T , in a cubic box with periodic boundary conditions. Our system contains $N = 10^3$ particles kept at a constant volume fraction $\phi = 0.01$. We have chosen this concentration because it is comparable with those used in experimental studies on Janus particles [16], so that our work could have a grounding experimental reference that our results could be compared to for $\theta_{max} \simeq 90^\circ$. Each simulation runs for a minimum of 10^7 steps with a time step $\delta t = 0.001$. All quantities in this chapter (and throughout the rest of this dissertation) are expressed in standard dimensionless units.

2.3 Structure formation

Our goal is to understand how particles condense into stable three-dimensional aggregates via the process of self-assembly, and how the specificity of the geometry of

the interaction is reflected in the final structure. Figure 2.2 reports one of the main results of our simulations. It shows a diagram indicating the lines in θ_{\max} - ε space separating the different self-assembled structures obtained, with a typical resolution of one degree for θ_{\max} , and $0.1k_B T$ for the binding energy.

As expected, a rich variety of structures arises depending on the position of the dividing surface θ_{\max} , and particles' binding energy, ε . Notice that, consistent with numerical simulations on self-assembly of viral capsids [38] and chaperonins [39], intermediate ordered aggregates are extremely sensitive to the size of the hydrophobic region and self-assembly occurs in a very narrow region.

At low binding energy the system is in a gas state. For small values of θ_{\max} and moderate values of ε (Figure 2.2a) particles aggregate into small clusters of 4 to 13 particles (mesoparticles) including icosahedral structures like those seen in [40]. For $\theta_{\max} \sim 90^\circ$, self-assembly yields worm-like extended structures (Figure 2.2b), as has been observed previously for Janus spheres [16]. As the angular location of dividing surface between the hydrophobic and hydrophilic regions region increases from 90° to 180° we find, in order of appearance, self-connected worm-like structures (Figure 2.2c), flat-crystalline bilayers (Figure 2.2d), faceted hollow cages (Figure 2.2e) (similar to structures seen in the self-assembly of cone-shaped particles [41, 42], yet not restricted to specific magic numbers of particles), amorphous fluid blobs (Figure 2.2f), and finally fcc crystals (Figure 2.2g).

2.4 Self-assembly pathways

Apart from the possible relevance of phases (d) and (e) for practical applications, we want to point out that none of these structures arises following a simple particle-by-particle growth mechanism, but rather by two-to-three step hierarchical self-assembly. The first step typically involves the formation of more- or less-structured mesoparticles (depending on θ_{\max}). Next, small clusters organize into either extended worm-like

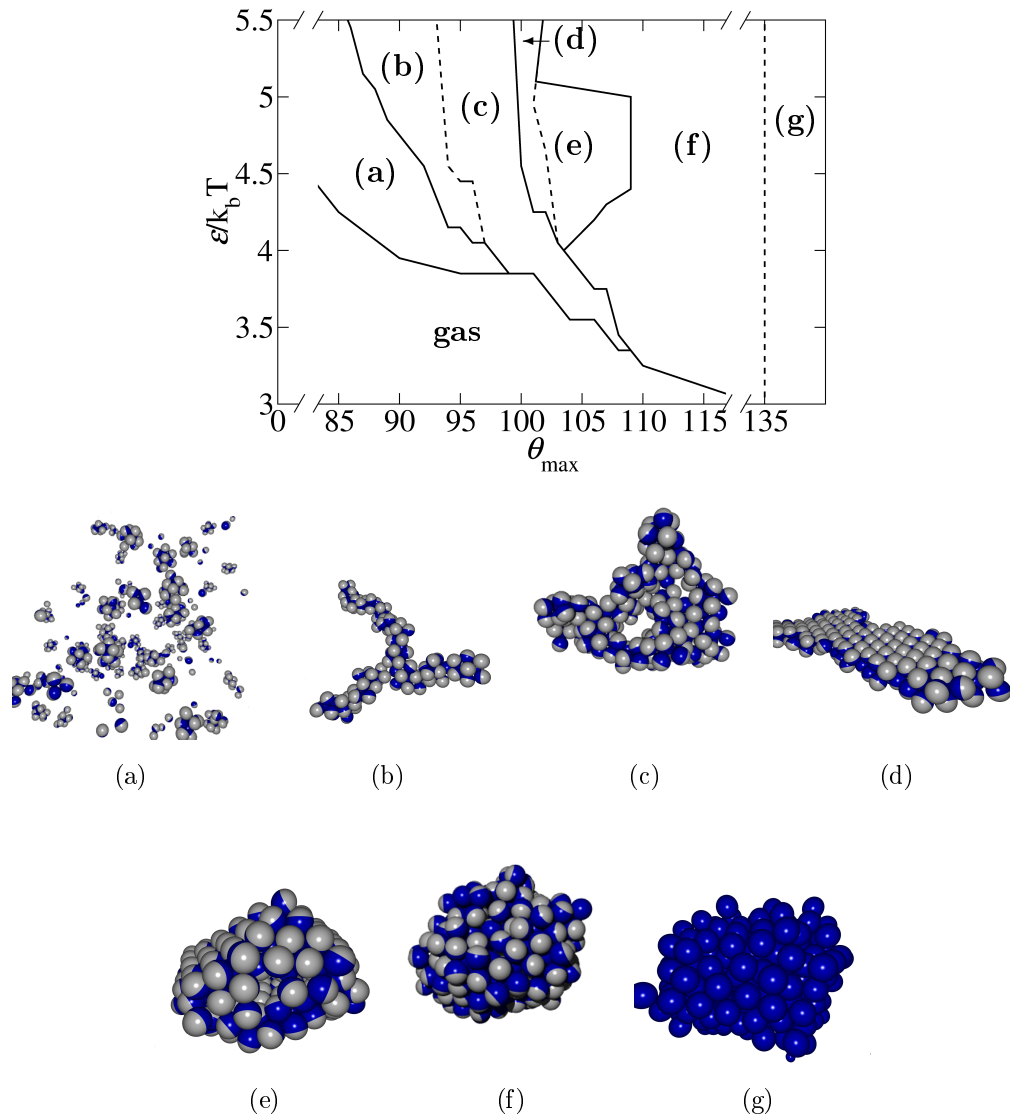


Figure 2.2: Self-assembly diagram of amphiphilic colloidal particles as a function of binding energy ε and size of hydrophobic region θ_{\max} . Region (a) is populated by small micelle-like clusters containing four to thirteen particles. Region (b) contains branched worm-like aggregates. In region (c) we find self-connected worm-like aggregates. Region (d) delimits flat hexagonal bilayers. In region (e) we find faceted hollow cages. Region (f) is populated by fluid amorphous aggregates. Finally, in region (g) we find large clusters with fcc order.

aggregates, which then coalesce or deform to produce the final structure, or into larger fluid clusters that, once beyond some threshold size, spontaneously organize into structured aggregates.

The dynamical pathway leading to structures in region (b) is detailed in reference [16], but in short, these worm-like structures form by the successive fusion of oligomers from trimers to heptamers; the individual particles reorient and rearrange so that they can fit together in a lock-and-key fashion to maintain five-fold rings with hydrophobic regions pointed into the interior of the worm.

It is of particular interest to discuss in some detail the dynamical pathway of structure formation relative to phases (c), (d), and (e) as they all form via a complex three-step mechanism. Surprisingly, the common precursor to all of them is the worm-like structure stable at $\theta_{\max} \simeq 90^\circ$. Self-connected worm-like aggregates are a consequence of the improved flexibility of the worm-like structures. As θ_{\max} increases, so does the ability of particles to rotate about their axes. The net result is that the branching ends of the clusters bend back upon themselves and begin to connect, thus forming topologically nontrivial aggregates.

To quantify the statistical difference between the aggregates found in regions (b) and (c), we measure their average radius of gyration

$$R_G = \left(\frac{1}{N_c} \sum_{i=1}^{N_c} \langle (\mathbf{r}_i - \mathbf{r}_{cm})^2 \rangle \right)^{1/2}, \quad (2.5)$$

where N_c is the number of particles in the cluster, \mathbf{r}_i is the position of particle i , and \mathbf{r}_{cm} is the position of the center of mass of the cluster, as a function of cluster size.

Results are shown in Figure 2.3, and clearly indicate that when θ_{\max} is increased from region (b) to (c), the typical aggregate becomes more compact, showing a significantly smaller exponential dependence on the number of particles. The limited statistics for large clusters prevent us from making any meaningful estimate of the chains' size exponent. However, note that a perfectly linear chain would show an exponent of 1 and a perfectly spherical aggregate would show an exponent of $\frac{1}{2}$. Thus,

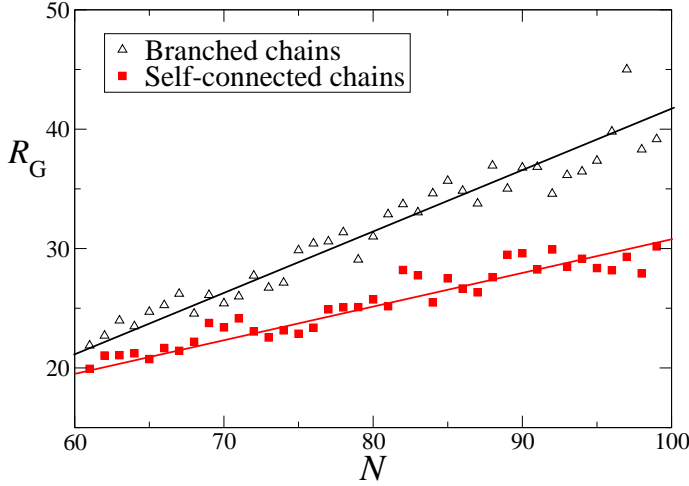


Figure 2.3: Radius of gyration as a function of aggregate size N for worm-like clusters in region (b) and (c) of Figure 2.2. The lines are guides to the eye.

the decreasing exponential dependence indicates a transition from “linear-like” chains towards more “cluster-like” geometry.

We also measure the angular probability distribution function, $P(\cos(\alpha))$, between neighboring particles in clusters containing at least 50 particles. Here α is defined as the angle between the particle axes; $\alpha = 0$ corresponds to particles with their patches pointing in the same direction, and $\alpha = \pi$ corresponds to particles pointing in opposite directions (which would be the case, for example, in two particles in a dumbbell configuration).

Figure 2.4 shows $P(\cos(\alpha))$ in regions (b), (c), and (d). $P(\cos(\alpha))$ shows a clear double peaked shape in region (d), indicating that most neighboring particles face either in the same direction (as would particles in a single monolayer sheet) or in the opposite direction (as would particles in the opposite monolayer of a bilayer structure), where the aggregates assume a planar bilayer configuration.

The more intriguing difference, however, is between region (b) and (c), highlighted in the insert of the figure. Region (b) is characterized by a peak at $\cos(\alpha) \sim -1$, and less distinguishable peaks at $\cos(\alpha) \sim \pm 0.74$ and $\cos(\alpha) \sim -0.5$; overall there

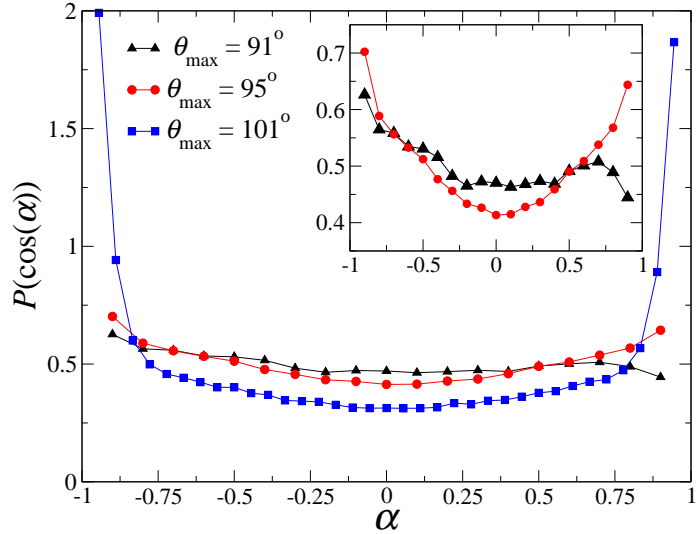


Figure 2.4: Angular probability distribution function, $P(\cos(\alpha))$, between neighboring particles in aggregates containing at least 50 particles in region (b) ($\theta_{\max} = 91^\circ$), (c) ($\theta_{\max} = 95^\circ$), and (d) ($\theta_{\max} = 101^\circ$), of the phase diagram. The insert highlights $P(\cos(\alpha))$ in regions (c) and (d). The data are averaged over 10 different clusters of each kind.

is a large probability for all possible orientations. These data suggest that branched worm-like aggregates have a roughly circular cross-section with particles oriented in a disordered fashion, but for a slight preference for a few selected angles (remnants of the mesoparticle structures from which they self-assembled), and an antiparallel neighbor opposite to most particles.

In contrast, region (c) is characterized by a more distinct double-peaked function, with each peak close to ± 1 . This is consistent with a cross section that has flattened with respect to structures in region (b), and indicates that each branch of the aggregate is acquiring bilayer-like features. The dashed line separating regions (b) and (c) shows where in the diagram the strings acquire sufficient flexibility to begin to form complex self-connected aggregates.

This observation is quite interesting when related to the dynamical pathway lead-

ing to phase (d). Bilayers are formed by either coalescence of co-planar loops, as shown in Figure 2.5, or by branch alignment. This transition occurs at $\theta_{\max} \simeq 110^\circ$, and it is driven by the large energy gain attained by the aggregates when each particle surrounds itself with the suddenly increased number of neighbors compatible with the enlarged hydrophobic region; 110° is roughly the value of θ_{\max} at which neighboring particles in a flat monolayer have a sufficiently favorable free energy to stabilize that geometry. This transition is quite sharp and represents a beautiful example of how a very small perturbation of the geometry of the local interaction can lead to completely different macroscopic structures.

Finally, formation of finite-sized, faceted capsids does not occur by self-assembly of misoriented, disjoined bilayers, but via a mechanism which, once again, involves multiple steps. As we increase the size of the particles' hydrophobic region, short worm-like clusters, which are now very flexible (owing to the highly permissive large hydrophobic patches), immediately fold onto themselves to form small, amorphous fluid blobs. We find that these blobs tend to remain fluid-like, whereas larger ones morph into faceted cages via a mechanism similar to that described for the formation of bilayers. Fusion of fluid blobs, as illustrated in Figure 2.6, is the main mechanism through which large blobs, which eventually turn into faceted cages, are generated.

The dashed line between regions (d) and (e) indicates the onset of cage formation; however, a non-negligible number of planar aggregates are found to coexist with the faceted cages in region (e). It is worth stressing that these faceted cages can be considered as colloidal analogs of the lipid vesicles discussed previously; they are hollow, their inner walls are hydrophilic, and one could in principle consider using them as possible drug carriers, with edges and corners presenting convenient locations for outer surface tagging. Furthermore, while a systematic study of their thermodynamics has not been performed, it would be expected to have features consistent with the calculation of the critical micellar concentration given in Section 1.2.2.

A statistical analysis of our data correlating size and structure for non-planar ag-

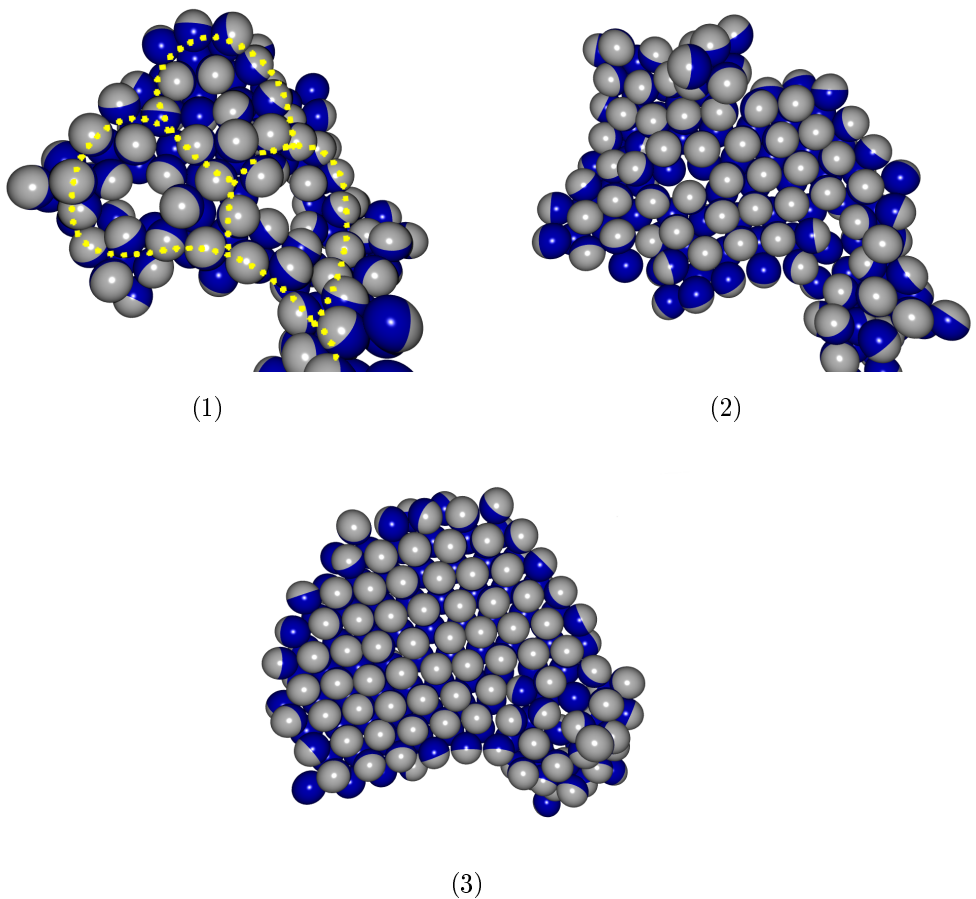


Figure 2.5: Sequence of three snapshots from our simulations showing the mechanism of bilayer formation via coalescence of three coplanar loops.

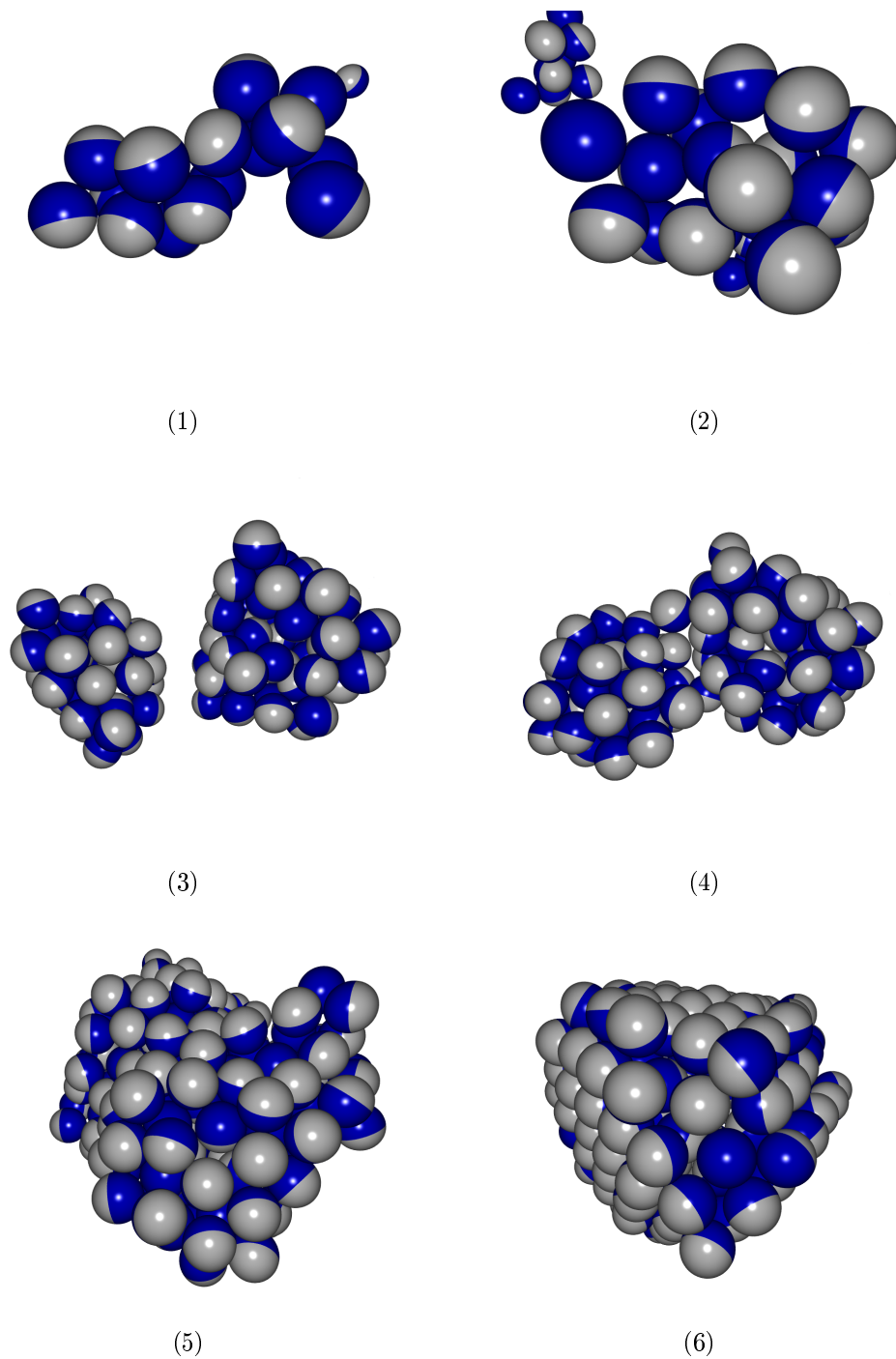


Figure 2.6: Sequence of six snapshots ((1)→(6)) from our simulations showing faceted cage formation via fast folding of short worm-like clusters ((1)-(2)) and subsequent fusion of fluid blobs ((3)-(6)).

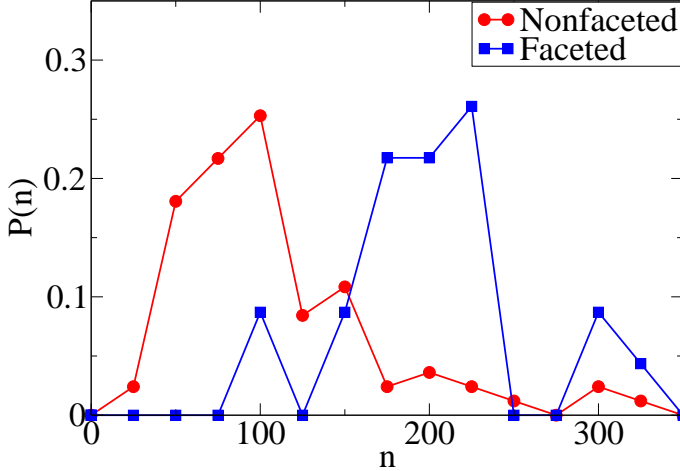


Figure 2.7: Probability distribution function $P(n)$ as a function of cluster size n for fluid and faceted aggregates in region (e) of the phase diagram.

gregates in region (e) indicates a clear preference for large clusters to develop into faceted hollow cages (see Figure 2.7). What sets the onset cluster size for this transformation is a complex compromise between the geometric constraints imposed by the interparticle potential; the energy gain to close-pack particles in a bilayer, which grows with the number of particles N ; the energy cost for sides and corners, which have on average fewer neighbors than in a fluid state and have an energy cost which grows as $N^{1/2}$ and N^0 , respectively; and finally the entropy loss due to particle ordering. Clearly, as N increases, at sufficiently large binding energy, planar configurations become the most stable, and this results in surface faceting.

When θ_{\max} increases to even larger values, the geometric constraints imposed by the interparticle potential become less restrictive, and planar bilayer configurations become less stable. Phase (f) is characterized by fluid, amorphous blobs which remain fluid at all sizes. Large clusters, formed by the smooth fusion of smaller ones, tend to contain smaller sub-clusters in their interior. This is the first sign indicating that aggregates begin to acquire a three-dimensional character, which eventually leads to the formation of clusters with fcc order, as inner and outer clusters begin to interact

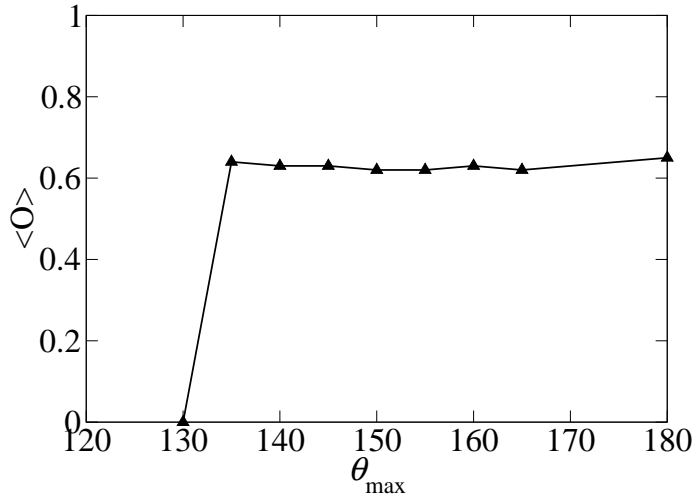


Figure 2.8: Degree of crystallinity of self-assembled aggregates as a function of hydrophobic area θ_{\max} .

with each other.

The location of the fluid to fcc transition is at $\theta_{\max} \simeq 135^\circ$, and was found by performing a structural analysis of the aggregates. Using the order parameters defined in Section 1.4.1, we measure the degree of crystallinity of the self-assembled aggregates. Figure 2.8 shows the degree of crystallinity $\langle O \rangle$ as a function of θ_{\max} across the angular range $\theta_{\max} \in [120 : 180]$. $\langle O \rangle$ is obtained by first averaging $\mathbf{q}_6(i) \cdot \mathbf{q}_6(j)$ over the neighbors of each particle i , and then by taking the average over all crystalline particles in a cluster. Clearly, once crystalline particles are formed, their degree of order in a fcc crystal structure is independent of θ_{\max} .

The explanation of this behavior is purely geometrical. In fact, for sufficiently large θ_{\max} , the hydrophilic area on each particle becomes so small that can be positioned among the 12 particles' contact points resulting from an fcc crystal without affecting its structure. Simple geometric considerations suggest that the onset value should occur for an angular span on the order of 150° . This value is compatible with our result $\theta_{\max} \simeq 135^\circ$, especially considering the extra tail of 10° in our definition of the potential angular dependence. A careful analysis of the model for decreasing values

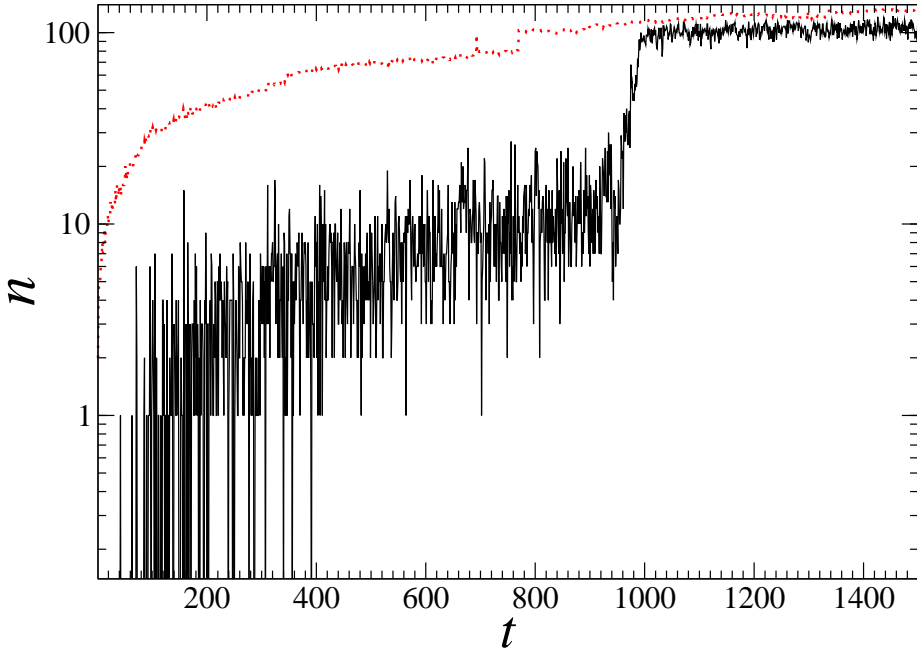


Figure 2.9: Linear-Log plot of the typical aggregate size n as a function of time. The dotted line shows the total number of particles in the aggregate, while the continuous line shows how many of those particles are tagged as crystal-like. These data were collected at $\theta_{\max} = 160^\circ$.

of θ_{tail} , not shown here, does indeed result in a systematic shift of the crystallization onset θ_{\max} to larger values.

Finally, it is important to point out that, once again, the pathway leading to the formation of crystalline aggregates occurs in a two-step fashion. Particles first condense into a large, fluid aggregate, and then crystallize from within the cluster via a standard nucleation process. Figure 2.9 shows in the same plot the aggregate size and the number of crystalline particles in the aggregate versus time for a system with $\theta_{\max} = 160^\circ$. Clearly, crystal formation begins long after the aggregate is formed, and the large fluctuations in the initial stages of crystal growth show the typical signature of crystal nucleation. These results are compatible with nucleation studies of isotropic colloidal particles interacting via a short-range attractive potential first

observed in [22], and highlight the crucial role played by metastable phases in the dynamics of crystal growth. In fact, we believe that this is the overarching physics behind the rich dynamical phenomenology we find throughout this paper.

Self-assembly proceeds, as predicted by Ostwald’s step rule in the context of crystal nucleation [43], in a stepwise fashion that accounts for the complex free energy landscape containing multiple metastable states. Ostwald’s step rule states that, as a general rule, when multiple crystalline phases are possible, it is not the most, but the least stable form which crystallizes first – equilibration may then proceed in steps to the most stable configuration.

Although we have not looked at the stability of the different phases found in our simulations, planar and vesicular structures are also observed in the study of the equilibrium properties of a model system similar to ours [44]. It is also worth mentioning that we expect the precise location of the phase boundaries to be somewhat sensitive to the particular choice of the angular potential. Unfortunately, this is very hard to characterize experimentally near the Janus interface and there is not a unique way of modeling that boundary. Our phase diagram is therefore intended to serve mostly as a guide for experimentalists, and not to model any specific category of amphiphilic particle.

2.5 Conclusions

In this chapter we used molecular dynamics simulations to study the self-assembly pathways of spherical amphiphilic colloidal particles. We uncovered a wealth of different aggregates whose structures span the three-dimensional spectrum. Specifically, depending on the size ratio between the hydrophilic and hydrophobic regions, particles self-assemble into small micellar clusters, worm-like structures, planar bilayers, faceted and fluid cages, and finally fcc crystals. We described the hierarchical self-assembly pathway leading to most of these structures and discussed their connection

to the geometry of local interparticle interactions. Finally, we made precise predictions for the formation of hollow amphiphilic cages.

Although the morphology of some of our aggregates can be predicted by simple geometric considerations, the dynamics leading to their formation is far less trivial, and may play a crucial role in the efficiency of the self-assembly process. We believe that, apart from trivial cases, any procedure attempting to design interparticle interactions to target specific structures could greatly benefit from taking into account the dynamics of structure formation in the design process.

Chapter 3

Phase behavior of hard aspherical particles

3.1 Introduction

Problems of packing and space tiling have fascinated scientists for a very long time. Kepler's 1611 essay "*Strena Seu de Die Nive Sexangula*" ("A New Year's Gift of Hexagonal Snow") [45] is probably one of the earliest publications on the subject. Herein he conjectured that cubic close packing and hexagonal close packing are the most efficient ways to fill a space using equally sized spheres. It wasn't until 1998 that Kepler's conjecture was finally announced to be proven (with a 99% degree of confidence) by Thomas Hales [46].

Most of the work on particle crystallization and self-assembly in the last decade has focused on monodisperse [47] or polydisperse [48, 49] systems of spherical or regularly-shaped particles (see also [7, 15, 20, 26, 38, 39, 42, 50–53] and references therein). Nevertheless, there are several important cases in which the shape of the single components cannot be tailored at will; however, an efficient packing, or an understanding of the physical properties of these densely compressed systems, is highly desirable. Two examples of outstanding problems in this category are the storage of

grains [54] and protein crystallization [55]. Both examples can be ideally thought of as two different aspects of the problem of understanding the role of shape in particle packing. In the first case the goal is to efficiently pack a system of randomly-shaped polydisperse grains; in the second, the aim is to crystallize non-spherical, yet equally shaped monodisperse components. In this chapter, both of these cases will be addressed.

An understanding of the relationship between the ability of particles to form macroscopically-ordered crystal structures and their shape is sought. Specifically, we analyze how random perturbations from the ideal spherical shape affect the crystallizability of a densely packed system of indistinguishable hard particles. Although a few papers have dealt with the thermodynamic behavior of soft/deformable particles as a model for polymer brushes or polymer-coated colloids ([56–59] and references therein), this is the first study where shape distortions, frozen onto the particles, are explicitly and systematically accounted for.

Crystallization in these systems occurs because of the free volume gain associated with the crystal structure, as discussed in Section 1.2.1. However, even in simple systems, precise calculations of the free energies involved in these transitions are very difficult. In complicated systems such as those discussed in this chapter, it is implausible to perform these calculations rigorously, and since the transition depends on small differences between large free energy values, computer simulations are the tool of choice to study and analyze this important process in detail.

3.2 A model of hard aspherical particles

In this chapter, each particle is built by randomly setting the center of N_b ($4 \leq N_b \leq 12$) spheres of diameter σ inside a spherical shell of diameter $\sigma_0 < \sigma$. The overall volume generated from the resulting overlapping aggregate defines our new particle.

Deviations from the ideal spherical shape can be conveniently controlled by varying

σ_0 and N_b . For $\sigma_0 = 0$ one recovers the spherical limit, and as σ_0 increases, particles develop larger and larger shape distortions. In a similar fashion, large values of N_b result in a bumpy but overall isotropic particle, whereas small values of N_b tend to generate very anisotropic shapes.

Once a particle is built, the center of mass of this cluster of balls is determined, and the entire cluster is scaled so that its total volume equals that of a spherical particle of diameter σ , i.e. $\frac{\pi}{6}\sigma^3$. Any two particles i and j interact via a hard repulsive potential defined as

$$U_{ij} = \begin{cases} 0 & \text{if } |r_s - r_t| > \sigma_R \quad \forall s \in i, \forall t \in j \\ \infty & \text{otherwise} \end{cases}, \quad (3.1)$$

where s and t run over all spheres of rescaled diameter σ_R constituting particle i and particle j respectively. Experimental realizations of colloidal particles similar to ours could be generated using the approach described in [7] to create uniform nonspherical particles with tunable shapes.

Figure 3.1 shows a few snapshots of particle shapes obtained for different values of N_b and σ_0 . In Section 3.3, a specific N_b and σ_0 will be chosen and a system will be composed of different random particles generated using the method above with those two parameters as inputs; in Sections 3.4 and 3.5, a system will be made up of identical particles from one specific outcome of the particle generation procedure.

Two order parameters characterizing the degree of asphericity of a particle are useful for relating the shape of particles in a system. The first is its asphericity, A (as opposed to the commonly used sphericity, S [60]), defined in terms of the surface to volume ratio of a particle $\alpha_p = \frac{A_p}{V_p}$ with respect to that of a sphere of diameter σ , $\alpha_s = \frac{6}{\sigma}$, as

$$A = 1 - S = 1 - \frac{\alpha_s}{\alpha_p}. \quad (3.2)$$

Given our model setup, $V_p = V_s$, A simplifies to

$$A = 1 - \frac{\pi\sigma^2}{A_p}. \quad (3.3)$$

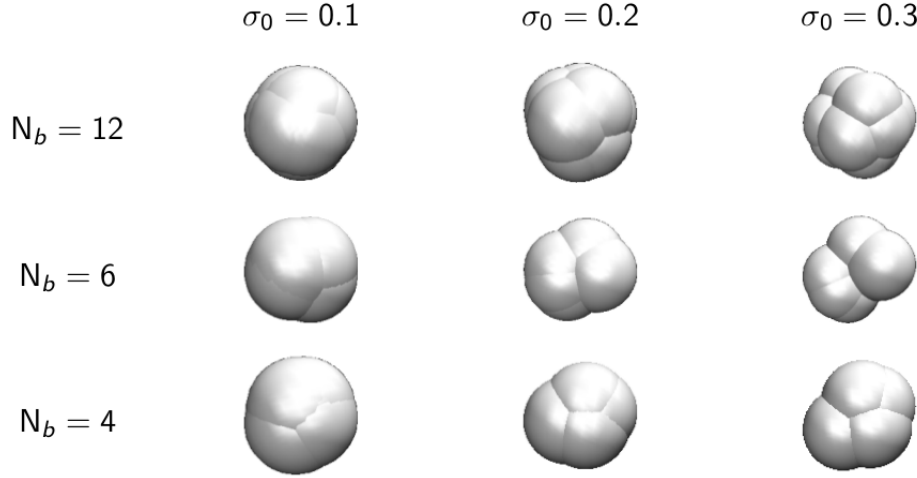


Figure 3.1: Model particles for different values of σ_0 and N_b built according to the scheme described in the text.

The surface area of a particle, A_p , is calculated via a simple Monte Carlo algorithm: a random point on the surface of a random one of the N_b spheres is chosen, and it is determined whether it is inside any of the other spheres or not – only points which do not lie on the inside of any other sphere are on the surface of the overall particle. This is repeated until the proportion of points on the surface of the particle as a fraction of all points chosen converges; using this fraction and the total surface area of all of the spheres combined, $N_b \times \pi\sigma_R^2$, the surface area of the particle can be calculated.

The second parameter, q , measures the orientational symmetry of the particle. It is used to describe the asphericity of random walks [61], and it is obtained by combining invariants of the particle inertia tensor I_{ij} as

$$q = \frac{(R_1^2 - R_2^2)^2 + (R_1^2 - R_3^2)^2 + (R_2^2 - R_3^2)^2}{2(R_1^2 + R_2^2 + R_3^2)}, \quad (3.4)$$

where R_1 , R_2 , and R_3 are the three principal eigenvalues of the inertia tensor of the particle, that is, the three principle radii of gyration of the particle.

Both parameters are defined so that they are equal to 0 for a perfectly spherical particle, and approach 1 for extremely aspherical ones. Note that A depends inti-

mately on the value of σ_0 used to construct the particle, whereas q depends only on the angular distribution of spheres about the center of mass – that is, it is completely independent of σ_0 .

It is worth briefly describing the limits of q , in particular, as its definition is less intuitive than that of A . As defined, the $q \rightarrow 0$ limit is a sphere; $q \simeq \frac{1}{2}$ for a thin, circular plate; and $q \rightarrow 1$ for a long, thin rod.

3.3 Shape-polydisperse systems

The results of simulations of polydisperse systems will be presented first. Such systems could represent, for example, a system of colloidal particle which is “sloppily” synthesized with some tolerance for deviation from a perfect sphere. Polydisperse systems have one major advantage, for a study such as that described below, over monodisperse systems: statistics.

In order to build up the statistical basis necessary to relate order parameters such as those described in Section 3.2, a large number of systems must be simulated for each data point; this severely limits the computational cost that may be expended per system. Polydisperse systems represent a huge decrease in the number of independent variables; because each system is made up of a large number of different particle shapes, one may be confident that the result obtained is not a result of some peculiarity of a specific shape studied. In Sections 3.4 and 3.5, monodisperse systems are studied, both as a comparison with the results attained in this section as well as using less computationally-intensive methods in order to study a larger number of particle shapes.

In order to determine the fluid-solid coexistence pressures for systems of aspherical particle, the method of direct fluid-solid coexistence simulation described in [62] was used. 1024 particles were placed in an fcc crystal lattice (at volume density $\rho_s \simeq 0.545$, the hard sphere crystal coexistence density [63]) centered in a box of dimensions

$L_x \times L_y \times L_z$. An fcc crystal was chosen based upon preliminary work, which indicated that when monodisperse aspherical systems form crystals, they tend to be (apart from a very few particular exceptions) fcc; no evidence has been found supporting the use of any other crystal geometry.

The dimensions of the box were chosen such that L_x and L_y were just large enough to accomodate the fcc crystal, and L_z was roughly four times larger. The crystal lattice was chosen such that the extension of the crystal in the z -direction was roughly twice that in the x - and y -directions, in order to increase the separation between the two fluid-solid interfaces in the system; by decreasing the surface-to-volume ratio of the crystal, one hopes to come as close to a “bulk-like” system as possible.

This crystal lattice was placed into equilibrium with a fluid of 1024 particles at hard sphere fluid coexistence volume density $\rho_l \simeq 0.495$. The fluid and crystal were both briefly allowed to relax in order to relieve any overlap introduced by the “bumpiness” of the particles and to allow the fluid to come fully into contact with the solid interface; because the particles are hard, there must be zero overlap in between particles.

Monte Carlo simulations were then run with constant number of particle N , pressure p , and temperature T (NPT ensemble), where the three box dimensions L_x , L_y , and L_z were allowed to fluctuate independently under the isotropic pressure p .

The number of crystalline particles, N_X , in the system was monitored as a function of Monte Carlo step; this quantity was determined using the standard spherical-harmonics based bond order parameter q_6 described in Section 1.4.1. Simulations were performed starting from a system initialized as desribed above, and N_X was monitored over the course of the simulation to determine whether it decreased (crystal melting) or increased (crystal growth).

Below the coexistence pressure, the crystal will melt, and above it, the crystal will grow; thus, the pressure at which the system transitions (as a function of pressure)

from decreasing N_X to increasing N_X represents the coexistence pressure p^* . This method is known to have a few caveats: slow equilibration, non-negligible finite size effects, dependence of the surface free energy on the specific face the crystal exposes to the fluid [62]. Nevertheless, for this specific system, we find this direct method to be more reliable than the two-step thermodynamic integration scheme described in [64].

Incorporating shape-polydispersity in these systems is not a trivial matter and requires some discussion. Unlike the common notion of polydispersity of spherical particles for which any particle size can be indifferently used as a reference (and thus only the width, not the center, of the distribution matters), each particle shape could be used as a reference shape for this study. The problem is that the phase behavior could be very much dependent on the specific choice of A and q . We therefore adopted a pragmatic approach to describing shape-polydispersity that has a natural experimental counterpart [7].

Namely, we consider the distributions of qs and As arising when constructing our particle using a given number of spheres N_b and a given value of σ_0 . Particles with large values of N_b generate narrow distributions shifted towards small values of q , while small values of N_b ($N_b \geq 4$) result in wide distributions peaked over large values of q . When $\sigma_0 \rightarrow 0$ one recovers the hard sphere limit for any value of N_b , and as σ_0 increases, larger and larger values of A will be sampled (without affecting the q distributions) until approaching the crystallizability boundary. Sample distributions of A and q for varying values of σ_0 and N_b (respectively) are shown in Figure 3.2

We systematically analyzed particles constructed with $N_b = 4, 5, 6, 8$, and 12 , and values of $\sigma_0 \in [0.05, 0.30]$.

All data points have been computed using two different random sets of particle geometries from the given distribution. The difference between the results from the two independent sets is smaller than the error bar associated with the numerical scheme. Figure 3.3 shows our results: the coexistence pressure p^* (as defined above)

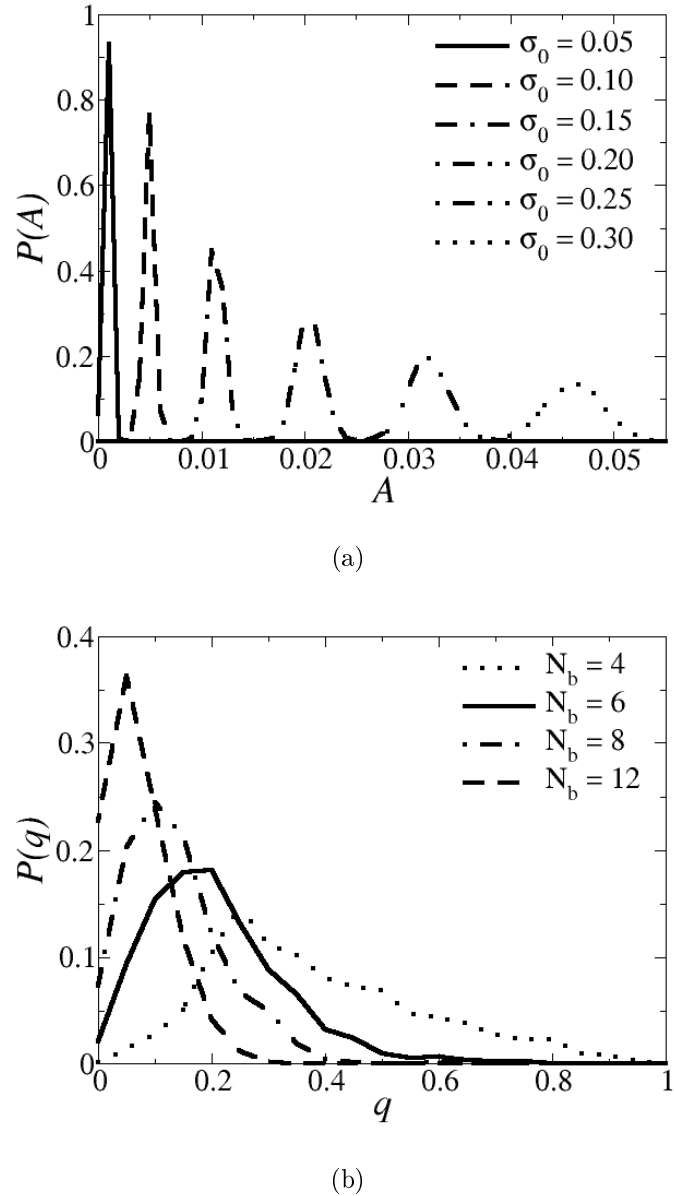


Figure 3.2: (a) Probability distributions of A for polydisperse systems with $N_b = 8$ and various values of $\sigma_0 \in [0.05, 0.30]$. The A distribution is approximately independent of N_b . (b) Distribution of q values for polydisperse systems with $N_b = 4, 6, 8$, and 12. Recall that q is independent of σ_0 . The distribution is significantly larger and broader for $N_b = 4$ than for the larger values of N_b .

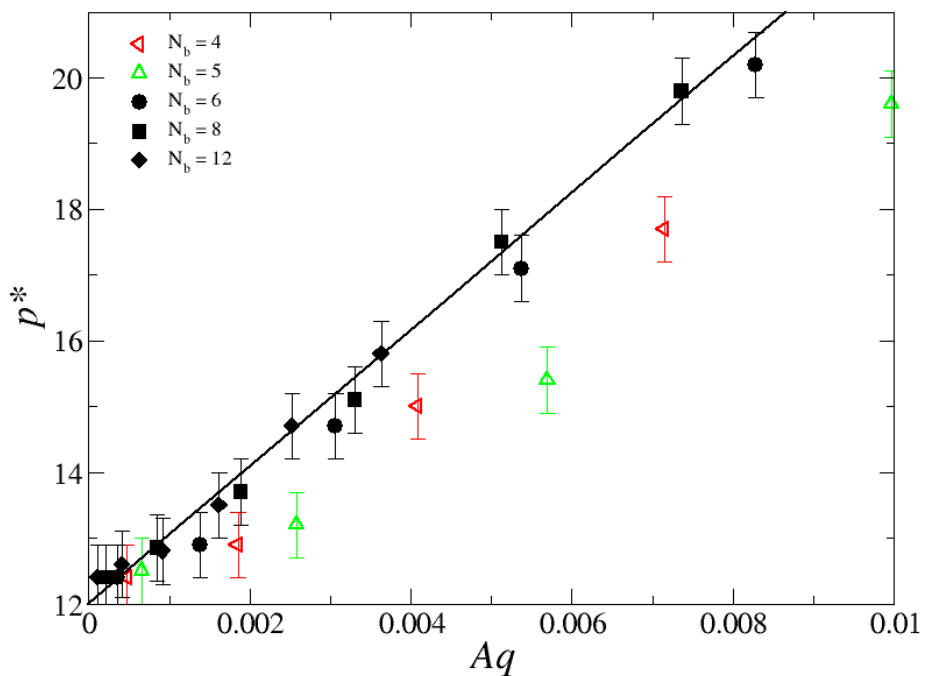


Figure 3.3: Coexistence pressure vs. Aq for shape-polydisperse systems of hard aspherical particles. The solid line is a fit to the data for $N_b \geq 6$.

versus the product Aq for $4 \leq N_b \leq 12$ and $\sigma_0 \in [0.05, 0.30]$.

Unsurprisingly, the coexistence pressure increases with increasing A and q , but remarkably, for $N_b \geq 6$, the relationship between p^* and Aq is simple linear one. We find that the coexistence pressures for these N_b values be fitted to $p^*(A, q) = 991Aq + 12$. Note that the y-intercept is near the hard sphere coexistence pressure of $p_{\text{HS}}^* \simeq 11.7$ [63], as it should be. This should be expected because the $Aq \rightarrow 0$ limit is a system of hard spheres.

These results thus suggests that $p^*(A, q)$ can be expressed in terms of a Taylor expansion in the quantity Aq :

$$\frac{p^*(A, q) - p_{\text{HS}}^*}{p_{\text{HS}}^*} = \alpha Aq + \dots \quad (3.5)$$

Note, however, that significant but systematic deviations from the linear fit are visible for systems of particles obtained with $N_b = 4$ and $N_b = 5$. These values of N_b correspond to particles with relatively large values of q and rather broad distributions (see Figure 3.2b), suggesting that other, higher-order terms in the expansion may be necessary. Furthermore, for such wide distributions fractionation between isotropic and anisotropic particles may become an important factor – this is an effect to which the direct simulation method used here is completely blind, because the system is initialized with a preformed crystalline volume with a random selection of particles. Fractionation would require complete melting of the initial crystal and subsequent formation of a fractionated crystal, which was not allowed in this study.

3.4 Monodisperse systems: coexistence pressures

The existence of a master curve for the coexistence pressure of significantly different particle distributions (provided $N_b \geq 6$), both in terms of their average value and their width, is quite remarkable, and provides a very compact and elegant way of expressing the equilibrium properties of such systems. As a test of the robustness of this relationship, ten monodisperse systems were generated by a single set of parameters:

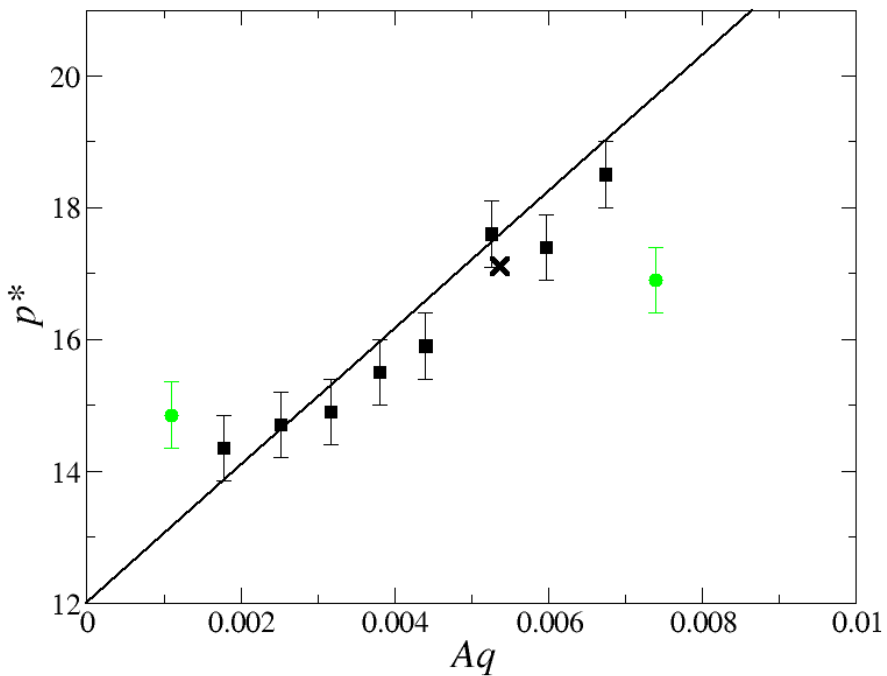


Figure 3.4: Coexistence pressure vs. Aq for monodisperse systems of hard aspherical particles with $N_b = 6$, $\sigma_0 = 0.2$. The line is a fit obtained from the data presented in Figure 3.3 for polydisperse systems with $N_b = 6$, 8, and 12. The cross indicates the position of the polydisperse system with $N_b = 6$, $\sigma_0 = 0.2$. Points at the extremes of the q distribution are shaded with a lighter color.

$N_b = 6$, $\sigma_0 = 0.2$. Each of these systems is characterized, by definition, by an infinitely sharp $P(q)$, and individual configurations were selected to cover a fairly wide range of Aq values, while keeping A roughly constant (because the distribution of A values for a given set (N_b, σ_0) is narrow, see Figure 3.2a). A plot of these data, shown in Figure 3.4, indicates that the relationship adapted unaltered from the polydisperse case is a reasonably good predictor of coexistence pressure for the monodisperse case as well. This is a clear indication that, up to some maximum, the master curve is overall independent of distribution width.

Notice that no coexistence pressures above $p^*(A, q) \simeq 21$ are reported. This is not a coincidence; in general, if a system was going to crystallize at all (that is, if the crystalline region of the simulation box was going to grow), the coexistence pressure p^* was below this value. This is interesting because this value is close to the fluid pressure of a system of hard spheres at the glass transition density [65], $p_G = 22.6$, and it is reasonable to assume that p_G sets an upper bound to the largest accessible fluid coexistence pressure for aspherical particles obtained with direct fluid/solid sampling.

In fact, this method is clearly susceptible to anomalies in system kinetics, thus making coexistence measurements at pressures larger than the ones herein reported quite cumbersome and somewhat unreliable. Nevertheless, if we assume that no aspherical hard particle will easily crystallize above p_G , we can formulate a prediction for whether a system of aspherical particles should be expected to easily crystallize: given $p^* \simeq 991Aq + 12$, and based upon this simple line of reasoning, one should expect, as a first-order approximation, a limit of

$$Aq \lesssim 0.011. \quad (3.6)$$

When the product Aq is below this limit, the system would be expected to easily crystallize at some pressure; above the limit, the system is never expected to crystallize.

3.5 Monodisperse systems: predicting crystallization

In order to test the prediction above, a large number of monodisperse systems was tested for the simple binary question: “Does this system crystallize easily?” In order to answer this question, traditional Monte Carlo simulations were performed in the *NPT* ensemble. Instead of initializing the system to be half crystalline and half fluid, a cubic box was used and the simulations was initialized in a fluid state. Each simulation contained $N = 128$ particles and contained a monodisperse system of aspherical particles constructed with some value of (N_b, σ_0) ; for the purposes of this study, we used $N_b \in \{4, 6, 8, 12\}$ and $\sigma_0 \in (0, 1)$.

The initial pressure was set to $p = 10$ and the pressure was incremented by $\Delta p = 0.5$ or smaller. Each simulation was run for a minimum of $4 \cdot 10^6$ Monte Carlo sweeps after thermalization. The simulation was ended when the system either crystallized or reached a volume fraction $\phi \simeq 0.6$, above the glass transition point of hard sphere, $\phi_G = 0.58$. Crystallization was detected by a combination of (a) the q_6 order parameter, (b) a careful monitoring of the system volume fraction over time for sudden jumps (indicating a phase transition), and (c) visual inspection. We investigated a total of 487 different particle geometries.

Figure 3.5 summarizes the result of this study. It is obtained by collecting the crystallizability of the 487 systems built out of the 487 different particle geometries we have generated across the A, q spectrum. Each point in the A vs q diagram represents the result of a set of simulations at different pressures. As would be expected, crystallization is favored when both A and q are small – that is, when the particles are nearly spherical by both measures. A roughly inverse relationship is clearly evident; particles with large A must have very small q in order to have a hope of crystallization, and vice-versa. But more importantly, we find the existence of a clear boundary delineating the crystallizability limit for every possible shape generated with our model (small deviations at the interface are likely due to finite size effects and/or the limited length of our simulations).

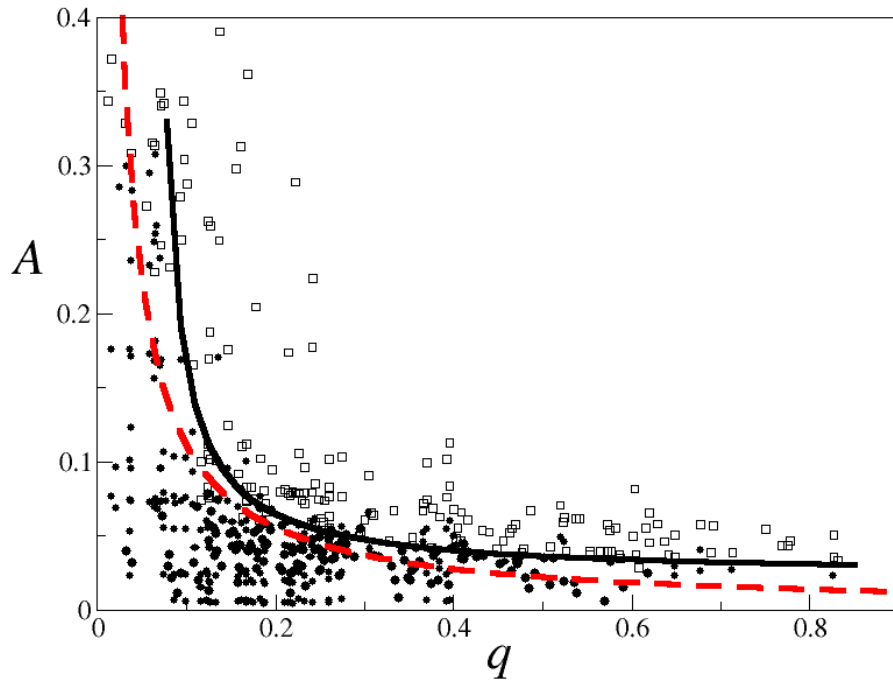


Figure 3.5: Crystallizability of monodisperse aspherical particles characterized in terms of two shape parameters A and q . Filled circles indicate particles that easily crystallized, while open squares indicate particles that did not. The solid line is a guide to the eye constructed between the two distinct regions in which particles crystallize or not. The dashed line represents a prediction of the crystallizability limit from above, $Aq = \simeq 0.011$.

This is quite remarkable because it provides a very useful way of predicting whether a particular particle shape can pack into a crystalline structure by simply measuring the experimentally accessible A and q .

Notice that for smaller values of q our data seem to indicate a sharp end of the crystal boundary. We believe this to be an artifact of our particle model. In fact, that region is where the value of σ_0 becomes sufficiently large ($\sigma_0 > 0.5\sigma$) to break the compactness of the particles generated with our method, especially those with smaller values of N_b . Furthermore, as small values of q indicate a large orientational symmetry, we expect this region to be heavily populated by specific geometric arrangements (as discussed below), whose packing properties, at large values of A , will be extremely sensitive of the particular value of N_b .

As our model is intended to describe randomly shaped particles, our diagram does not include the results for particles designed with very specific shapes such as rods, plates or regular polyhedral geometries that are known to crystallize. These particular cases would generate sharp peaks around specific values of q . Furthermore, is not clear that our two order parameters, which have after all been selected to describe asphericity, would be the most appropriate to study deviations from an arbitrary nonspherical designed shape. We therefore limited our study to $N_b > 3$, to explicitly avoid trivial cases such as rod-like ($N_b = 2$) and plate-like particles ($N_b = 3$).

The dashed line in Figure 3.5 is the limit $Aq \lesssim 0.011$ attained in Section 3.3. Although it is not a perfect division, likely due to many factors (including finite-size effects), this simple prediction provides a reasonable dividing line which would predict the crystallization or non-crystallization of 387 of the 487 systems tested, or almost 80%. Given the uncertainties discussed above associated with the data points, we believe this is a remarkably good rate of success.

3.6 The character of crystals of aspherical particles

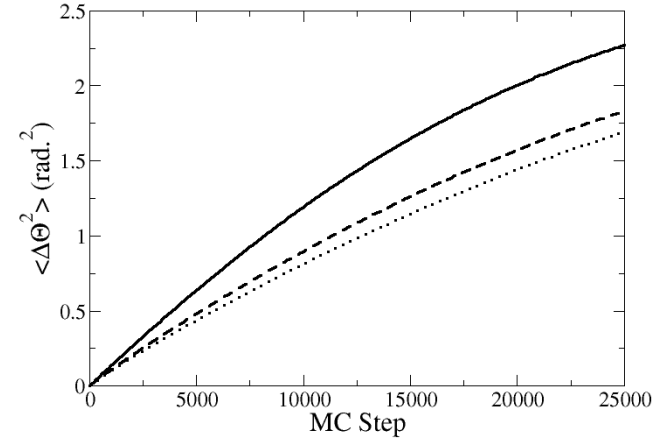
Two obvious questions present themselves in the face of these data. The first is: what is the nature of the crystals formed when particles do crystallize; does the system present translational but not orientational order, as expected for $A \simeq 0$, or does the rotational motion of the particles become restricted for large values of A ? The second is: what sets the boundary between the two phases; do the particles that fail to crystallize do so because they become kinetically trapped or because of the lack of a stable crystal phase?

To address the first question, we measured the rotational diffusion, $\langle \Delta\theta^2 \rangle$, for 20 systems that crystallize, all at a reduced pressure $P^* = 20$ and near the phase boundary. As a reference we also plotted $\langle \Delta\theta^2 \rangle$ for nearly spherical particles, obtained by setting $\sigma_0 = 10^{-4}\sigma$, where we know particles are free to rotate at their lattice sites.

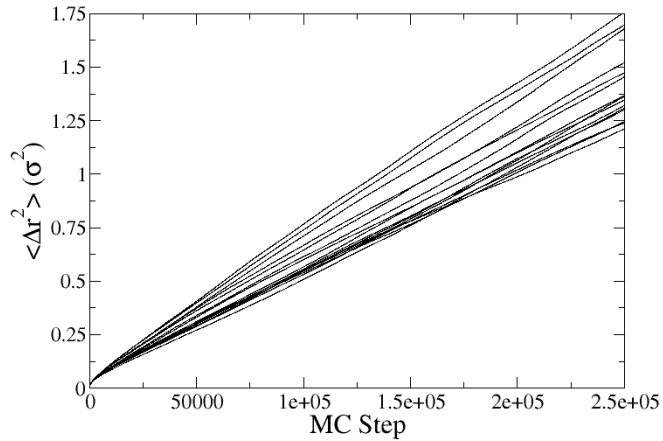
As can be seen in Figure 3.6a, we find no evidence that particles in the crystalline phase become orientationally arrested or manifest an orientationally anomalous behavior. The only effect is that of decreasing their diffusion constant, but this is expected from simple geometrical considerations. It is obvious that at very large densities, regardless of the specific phase a system selects, particles' orientations will manifest a glassy behavior or eventually freeze. [66]

It is therefore of interest to also look at the dynamical properties of those particles in systems which do not crystallize and are located just across the phase boundary from the ones that do crystallize. These results, obtained at the same reduced pressure $P^* = 20$, are also shown in Figure 3.6a. We find no signature of anomalous dynamics, neither in the rotational (Figure 3.6a), nor in the translational (Figure 3.6b) degrees of freedom; that is, such systems behave as regular fluids.

This rotational plasticity in crystals of these aspherical particles provides an explanation for why the results of the polydisperse systems studied in Section 3.3 applied to the monodisperse systems studied in Sections 3.4 and 3.5. The practical effect of this fact is that any two identical neighboring particles will typically be



(a)



(b)

Figure 3.6: (a) Rotational mean square displacement for a subset of the particles considered. The solid line is a reference for nearly spherical particles. The dashed line is the result for those particles that crystallized and the dotted line shows $\langle \Delta\theta^2 \rangle$ for those that did not. The data were averaged over 20 realizations in each region under the same pressure $P^* = 20$. (b) Translational mean square displacement for 20 different particle shapes that failed to crystallize.

misoriented and face each other with random regions of their respective surfaces. As a consequence, their mutual interaction becomes hardly distinguishable, on average, from that of two particles with different shape, thus explaining why monodisperse and polydisperse systems may indeed present analogous equilibrium properties.

Note, however, the deviations from the predicted pattern in Figure 3.4 at the extreme ends of Aq , corresponding to particle shapes that have values of q significantly different from the average q of the distribution. The deviation at large q is expected as the analogous behavior is observed for polydisperse systems; as particles become more anisotropic their rotational degrees of freedom are reduced until they perfectly align in the $q \rightarrow 1$ (rod) limit, making the averaged random-shape argument described above inappropriate.

A bit more surprising is the deviation for very small values of q , for which we find that the polydisperse system with $N_b = 12$ nicely follows the master curve. To rationalize this behavior one has to realize that for small values of N_b , when $q \rightarrow 0$, particles tend to acquire rather symmetric and specific geometries, such as platonic solids, which also require orientational ordering to tile the space as soon as A becomes sufficiently large. These specific particle shapes dominate the shape space for $q \sim 0$ and small values of N_b , and lead to deviations from the inverse power law behavior.

This result is by no means conclusive, as a thorough investigation of this last point would require larger system sizes and an event-driven dynamics of the components. Our results seem to suggest that what sets the location of the phase boundary is not a sudden slowdown of the dynamics of the system, but more likely an increase of the Gibbs free energy difference between the crystalline and the fluid phase, analogous to that found for polydisperse spherical particles [48]. It would be interesting to investigate the equilibrium properties and the stability of candidate crystalline structures for different values of A and q to investigate whether our boundary line coincides with the onset of crystal instability, but for the reasons given above, we have not attempted to do so.

3.7 Conclusions

To conclude, our data represent a first step in attempting to understand how deviations from asphericity affect the thermodynamics of crystallization of particle systems. Our results show that the coexistence pressure of systems of monodisperse and shape-polydisperse particles is remarkably well-described, within the limits described above, by a simple first order Taylor expansion in terms of Aq , $\frac{p^* - p_{HS}^*}{p_{HS}^*} = \alpha Aq + \dots$

Apart from the details concerning the dynamics of these systems, our results show that, for aspherical particles, shape and crystallizability can be directly and easily correlated when particles are characterized in terms of their asphericity via q and A . Our data suggest precise limits for the manufacture of nanocomponents expected to crystallize, which should be experimentally testable, and may have important implications for the problem of protein crystallization. The latter system is clearly far more complex than the one explored here, since not only shape, but also interparticle direct interactions (which are not necessarily isotropic), are responsible for the organization of proteins into large macroscopic crystals. Nevertheless, it would be interesting to systematically explore to what extent a similar correlation exists in this case.

Finally, a further avenue of study, and one that is vital to truly understanding phenomena surrounding crystallization of these particles, has to do with the free volume available in a crystal. As discussed in Section 1.2.1, the chemical potential difference between the fluid and crystalline phases, which is a vital consideration in the crystallization, is determined, in purely repulsive systems such as these, by the free volume available per particle in the crystal versus that available to the “jammed” fluid at the same density.

This is not a trivial quantity to compute in complicated systems such as these, and will be very sensitive to details about how, precisely, it is calculated. For example, it might be necessary to attempt to calculate an “accessible” volume of each particle, in analogy to solvent-accessible volumes in proteins, which accounts for the fact that

a narrow, deep cleft, for example, should have no bearing on the way in which two particles of the same size interact with each other. However, this would be a vital step toward a complete theoretical understanding of the problem, and work in this direction is currently underway.

Chapter 4

Two-dimensional packing of soft particles on planes and spheres

4.1 Introduction

Understanding how nanocomponents spontaneously organize into complex macroscopic structures is one of the great challenges in the field of soft matter today. Indeed, the ability to predict and control the phase behavior of a solution, given a set of components, may open the way to the development of materials with novel optical, mechanical, and electronic properties.

Of particular interest for optical applications are the crystalline phases. Until recently, it was believed that shape anisotropy and/or directional interactions were key elements for the formation of crystals with complex symmetries commonly observed, for instance, in atomic solids.

The study of the phase behavior of components interacting with exotic (yet isotropic) potentials has proven this belief to be incorrect. For instance, Torquato *et al.* have shown, using inverse optimization techniques, that it is possible to achieve non-close-packed structures such as simple cubic, hexagonal, wurtzite and even diamond phases with isotropic pair potentials (see ref [50] for a review on the subject).

Furthermore, spherical particles interacting via a hard core and a repulsive shoulder potential are known to organize into complex mesophases not unlike those found with diblock copolymers [67].

One class of pair potentials that has recently attracted much attention is that describing the interactions between soft/deformable mesoparticles. Unlike typical colloidal particles for which excluded volume interactions are strictly enforced via a hard-core or a Lennard-Jones potential, complex mesoparticles such as charged or neutral star polymers, dendrimers or microgels present a more peculiar pair potential describing their volume interactions. Surprisingly, the simple relaxation of the constraint of mutual impenetrability between isotropic components gives access to several non-close-packed crystalline structures at high densities.

Given the complexity of these mesoparticles, their interactions are usually extracted via an explicit coarse-grained procedure to obtain ad hoc effective pair potentials. What emerges is a great variety of nontrivial interactions, some of which allow for even complete overlap among the components, resulting in a very rich phenomenological behavior. Remarkably, it is feasible to engineer interactions between star polymers or dendrimers by controlling their overall chemical and topological properties [10].

The phase behavior of several systems adopting these exotic, but physically inspired, interactions has been the subject of several publications [57–59, 68–75]. Notably, it was found that some classes of soft interactions lead to reentrant melting transitions, others to polymorphic cluster phases [76], and in general to multiple transitions involving close-packed and non-close-packed crystalline phases [77–79] as a function of the system density.

Remarkably, the phase behavior of these systems is very much dependent on the shape of the pair potential. Likos *et al.* [80] established a criterion to predict whether for a bounded and repulsive potential reentrant melting or cluster phases will occur based on the sign of the Fourier transform of the interaction. Nevertheless, there is

currently no method to predict *a priori* what specific crystal structures may become accessible for a given potential. For a recent review on the subject we refer the reader to reference [81].

The main idea behind the formulation of the criterion is that at large densities each particle is typically interacting with such a significant number of neighbors that the simple mean field approximation (MFA) for the excess free energy of the system becomes quite accurate. Under this approximation, the internal energy of the system

$$F_{\text{ex}} [\rho(\mathbf{r})] \simeq \frac{1}{2} \int d\mathbf{r} d\mathbf{r}' V(|\mathbf{r} - \mathbf{r}'|) \rho(\mathbf{r}) \rho(\mathbf{r}'), \quad (4.1)$$

where $\rho(\mathbf{r})$ is the density profile of the system and is assumed not to vary too rapidly with respect to the particle size σ , and the approximation for F_{ex} gets more accurate for higher densities ρ . This leads to a pair correlation function with a very simple form

$$c(|\mathbf{r} - \mathbf{r}'|; \rho) \equiv \lim_{\rho(\mathbf{r}) \rightarrow \rho} \frac{\partial^2 \beta F_{\text{ex}} [\rho(\mathbf{r})]}{\partial \rho(\mathbf{r}) \partial \rho(\mathbf{r}')} = -\beta V(r). \quad (4.2)$$

The Ornstein-Zernike relation, which relates the Fourier transform of the total correlation function, $\tilde{h}(q)$, to the Fourier transform of the pair correlation function, $\tilde{c}(q)$, takes the form

$$\tilde{h}(q) = \frac{\tilde{c}(q)}{1 - \rho \tilde{c}(q)}. \quad (4.3)$$

The static structure factor $S(q)$ can then be related to $\tilde{h}(q)$, resulting in a simple functional form

$$\begin{aligned} S(q) &\equiv 1 + \rho \tilde{h}(q) = 1 + \frac{-\rho \beta \tilde{V}(q)}{1 - \rho \beta \tilde{V}(q)} \\ &= \frac{1}{1 + \beta \rho \tilde{V}(q)}. \end{aligned} \quad (4.4)$$

This simple expression for $S(q)$ allows one to deduce several properties of the fluid phase.

For instance, the instability of the fluid phase (and thus crystallization of the fluid) is indicating by a singularity in $S(q)$. However, when the MFA holds, Equation 4.4 indicates that a singularity in $S(q)$ will occur when $\beta \rho \tilde{V}(q) = -1$.

This means that, if $\tilde{V}(q)$ is positive defined for all q , then for any temperature or density at which the MFA becomes exact, the fluid phase will be the most stable phase. Solid phases are possible when the MFA becomes inaccurate or for potentials which have non-positive-defined Fourier transform. Thus, if a potential with a positive-defined Fourier transform passes from a state in which the MFA is inaccurate to one in which it holds, it is possible to have reentrant melting, in which, as a function of increasing density (for example), the system passes from the fluid phase, through a crystalline phases, and then back to the fluid phase. For more details on the subject we refer the reader to [80].

In this chapter we focus on two-dimensional systems. Although much of the research in this field has focused on three-dimensional systems, earlier numerical work on particles interacting via a hard core plus a shoulder potential in two dimensions has revealed a phenomenological behavior that can be as rich as that observed at higher dimensionality [82–85].

Here we focus on bounded soft potentials. Specifically, expanding on recent results on Hertzian spheres [79] and dumbbells [86] in three dimensions, we analyze the phase behavior of soft elastic particles in two dimensions. We generalize our results to spherical surfaces, and discuss the generalized Thomson problem for our soft potentials by identifying novel polyhedral structures representing minimal energy configurations formed by soft particles constrained on the surface of a sphere at different packing densities. Although the term “packing” generally refers to hard-particle or weakly compressed systems, here it should be understood to be describing the ordering of highly compressed soft and deformable particles.

4.2 Simulation details

To study the phase behavior of soft nanoparticles in two dimensions we performed numerical simulations. We considered systems of at least $N = 1000$ spherical particles

and used the standard Monte Carlo method with random initial configuration in the NPT and NVT ensemble for the planar and spherical case, respectively. Results for two-dimensional systems were reproduced starting from a square-crystal initial configuration. All simulations where run for a minimum of 10^6 iterations.

Any two particles in our system interact via a generalized version of Hertz potential. The Hertz potential describes the elastic energy penalty associated with an axial compression of two deformable spheres. Its functional form can be generalized as follows

$$V(r) = \begin{cases} \varepsilon(1 - \frac{r}{\sigma})^\alpha & \text{for } r \leq \sigma \\ 0 & \text{for } r > \sigma \end{cases}, \quad (4.5)$$

where σ is the particle diameter, r is the interparticle distance, ε is the unit of energy, and α is a parameter that we control to modulate the shape of the interaction. The elastic (Hertzian) case is recovered for $\alpha = \frac{5}{2}$.

The Hertz model, developed to account for small elastic deformations, becomes inaccurate when associated to the large overlaps among particles that is achieved at large densities, which will be discussed further in Section 4.5; nevertheless, it provides us with a simple representation of a finite-ranged, bounded soft potential with a positive definite Fourier transform (a condition that guarantees reentrant melting in the phase diagram [80]). We included in our study two more values of α to account for a slightly harder ($\alpha = \frac{3}{2}$) and a slightly weaker ($\alpha = \frac{7}{2}$) potential than the elastic one ($\alpha = \frac{5}{2}$). Figure 4.1 shows these potentials.

Crystallization in our simulations was determined using a combination of visual inspection and numerical order parameters similar to those described in [87], which can be seen as a simpler, two-dimensional version of those described in Section 1.4.1. Specifically, given a randomly chosen particle j , and a reference direction set to be along the bond between this particle and one of its nearest neighbors, we can define an order parameter sensitive to a crystal of D -fold symmetry (specifically six-fold hexagonal and four-fold square crystals) as follows.

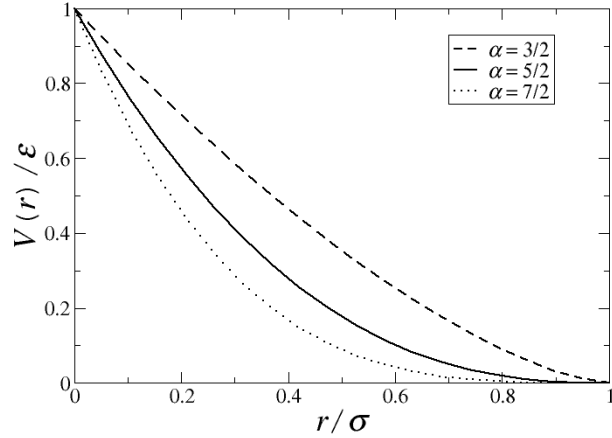


Figure 4.1: Plot of the rescaled pair potential $\frac{V(r)}{\varepsilon} = (1 - \frac{r}{\sigma})^\alpha$ for the three values of α used in this study: $\alpha = \{\frac{3}{2}, \frac{5}{2}, \frac{7}{2}\}$

For all particles k within a radius of some cutoff r_c of j (including j itself), we calculate the angle ϕ_{lk} between the bond joining each of the D nearest neighbors l of k to k and the reference direction. If the number of particles within r_c of j is N_k , then the order parameter Ψ_D^j is given by:

$$\Psi_D^j = \frac{1}{N_k} \frac{1}{D} \left| \sum_k \sum_l e^{i D \phi_{lk}} \right|. \quad (4.6)$$

This process is then repeated N times and an average Ψ_D is calculated, yielding a value between 0 (for completely disordered systems) and 1 (for perfectly crystalline systems).

This order parameter is analogous to that defined in [87] except that instead of Ψ_D^i being an average over all particles k in the system, it is only over particles k within r_c ($= 1.65\sigma$ in our case); thus it is “semi-local” and allows crystalline order to be detected even in the presence of metastable grain boundaries. The order parameter in [87] represents the $r_c \rightarrow \infty$ limit of the above method.

To draw the phase diagrams we scan the phase space defined by the rescaled

temperature $T_r = \frac{k_B T}{\varepsilon}$ and the rescaled number density $\rho_r = \frac{N\sigma^2}{A}$ (where A is the area of the system) to evaluate the several phases of the system in terms (when possible) of its order parameter Ψ_D . The phase of the system was evaluated on a grid with a resolution of 0.001 in T_r and roughly 0.25 in ρ_r . The lines separating the different regions are guides to the eye, and are placed between data points relative to structures having different symmetry.

Given the peculiarities of phase transitions in two dimensions, and the richness in the phases behavior reported, we have not attempted to establish equilibrium boundaries between the different phases, yet we have reproduced our results using molecular dynamics simulations with a Langevin thermostat performed in key regions of the phase space, and compared the stability of the crystalline structures by measuring their relative energies at $T_r \rightarrow 0$.

Because thermodynamic phase diagrams are not presented, the phase diagrams that follow should be considered as semi-qualitative illustrations of the variety of phases which occur and the trend with which their occurrence follows the system density; specifics of the slopes and the precise location of the dividing lines between phases would require a more accurate study of the thermodynamic stability of the phases.

For the simulations of the generalized Thomson problem in the latter half of the chapter (Section 4.4), a temperature quench was performed from a relatively high temperature ($T_r = 0.1$) to a very low temperature ($T_r = 10^{-7}$) in order to approach the zero-temperature limit. For each r_0 , the system was simulated with three initial configurations; one random, and one each from the structure obtained at slightly larger and slightly smaller r_0 .

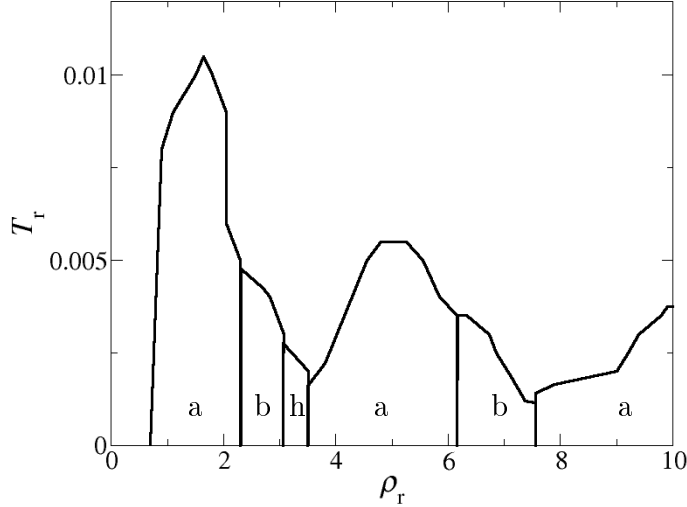


Figure 4.2: Temperature vs. number density phase diagrams for two-dimensional particles interacting via a Hertz potential ($\alpha = \frac{5}{2}$). Labels on the plots refer to the labels of the phases in Figure 4.4.

4.3 Soft particles in planar geometries

We begin by presenting the phase diagram for the case of Hertzian (elastic) spheres. The result is shown in Figure 4.2. The labels in the figure refer to the structures shown in Figure 4.4. As expected from Likos' criterion [80] our system shows reentrant melting behavior and a maximum temperature above which the system remains fluid at all densities.

The phase behavior reported here is qualitatively similar to that observed in three dimensions; however, the two-dimensional system does not produce a phase space that is as structurally rich as its three dimensional counterpart. Across the spectrum of densities (up to $\rho_r = 10$) and temperatures (down to $T_r = 10^{-6}$) that we explored, we find multiple crystal-to-crystal transitions from hexagonal (phase (a)) to square symmetry (phase (b)). Interestingly, the occurrence of the two phases has an alternating periodic pattern, and no isostructural transition was detected in our system [88]. The

multiple occurrences of a single phase (for example, phases (a) and (b) in Figure 4.2) are identical except for uniform scaling of the interparticle distances as the density of the system is changed.

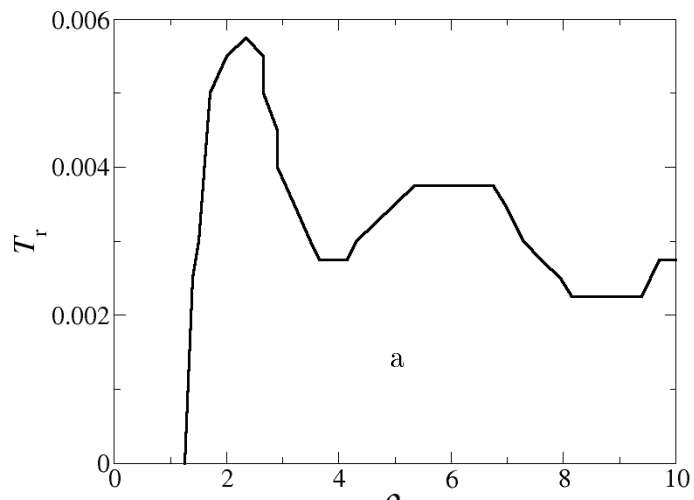
This pattern is only broken at a small range of densities centered around $\rho_r \simeq 3.25$. This region (phase (h)) is characterized by a complex structure dominated by particles arranged mostly into pentagonal units. The color coding of the phase shown in Figure 4.4h helps in rationalizing the overall symmetry of the structure which in this representation can be thought of as the combination of four square lattices. Three lattices are generated by pentagonal units, displaced with respect to each other but oriented along the same axis. The fourth lattice is built out of the non-connected particles and is oriented along an axis that forms an angle of 45 degrees with the other lattices.

To understand how the phase behavior is affected by the specific choice of the functional form of the potential, we repeated the calculation of the phase diagram for $\alpha = \frac{7}{2}$ and $\alpha = \frac{3}{2}$. The results are presented in Figure 4.3.

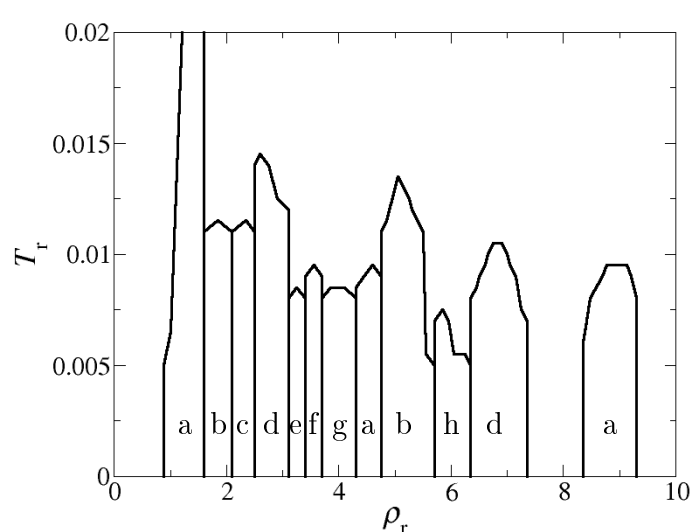
Although the overall trend is very similar, the number and the sequence of phases that we find are significantly different. Namely, $\alpha = \frac{3}{2}$ leads to a significantly richer structural behavior, while the larger value of α results in a single hexagonal crystalline structure; however, even for the $\alpha = \frac{7}{2}$ case, we observe a complicated variety of reentrant behaviors.

As a reference, notice that our potential tends to the linear-ramp potential for $\alpha = 1$ (for which a large number of phases including quasi-crystals have been observed [84]), we recover the square-shoulder potential for $\alpha \rightarrow 0$ (for which a cascade of cluster phases are expected), and tends to a Kronecker delta potential for $\alpha \rightarrow \infty$ (for which no crystallization is expected at any finite density).

At least as a general trend, it is therefore not surprising that structural variety increases for smaller values of α . In this regard, it is interesting to estimate the critical power above which the hexagonal lattice becomes the only stable lattice as observed



(a)



(b)

Figure 4.3: Temperature vs. number density phase diagrams for two-dimensional particles interacting via the generalized Hertz potential with (a) $\alpha = \frac{7}{2}$ and (b) $\alpha = \frac{3}{2}$. Labels on the plots refer to the labels of the phases in Figure 4.4.

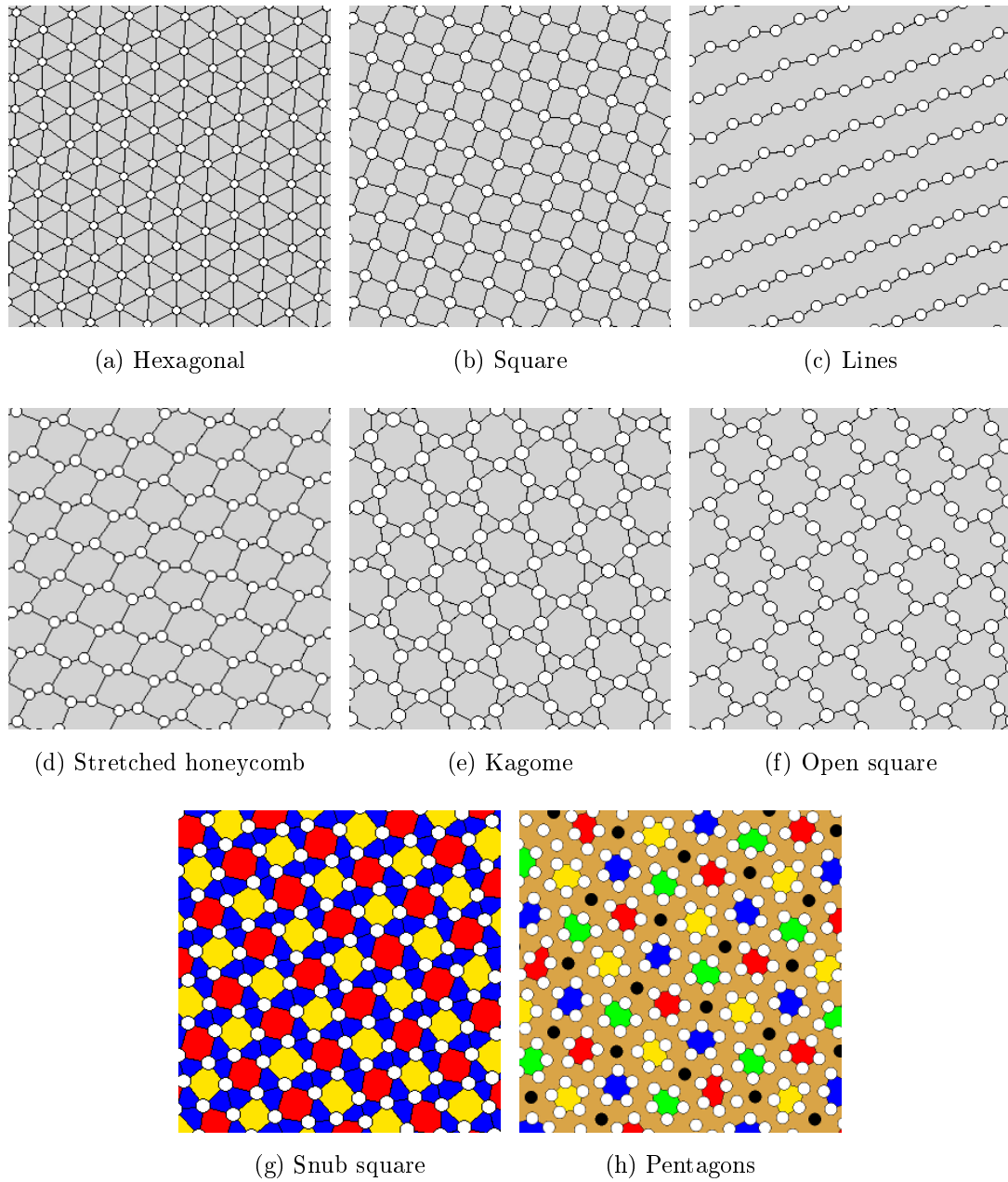


Figure 4.4: Two-dimensional crystal phases formed in these systems.

in Figure 4.3a.

Given that the only other competing structure at large values of α is the square lattice, we computed the energy density difference between hexagonal and square lattices as a function of density and at zero temperature for different values of α . The result is presented in Figure 4.5 for densities up to $\rho_r = 25$ (our full numerical data extend up to $\rho_r = 100$, but are not shown for the sake of clarity). We find that the hexagonal lattice becomes more stable than the square lattice at all densities for any powers above the onset value $\alpha^* \simeq 3.182$.

Several numerical simulations at finite densities for powers ranging from $\alpha = 10$ to $\alpha = 50$ were carried out, and indeed only hexagonal structures were observed upon system ordering. The presence of reentrant melting was also established for $\alpha = 5$ and $\alpha = 10$. The oscillating behavior of the energy density difference for $\alpha < \alpha^*$ also explains qualitatively the periodic structural pattern observed in the phase diagram for $\alpha = \frac{5}{2}$.

The precise underlying physical origin of this periodic structural pattern is currently under further investigation. Early results indicate that the finite range of the potential is a significant contributor to the behavior; in particular, the fact that as the density of the system increases, the number of particles with which each particle in the system can interact increases in a stepwise fashion.

4.4 Soft particles on spheres: the soft generalized Thomson problem

We now turn to the discussion of the second part of this chapter. Given the structural variety observed in the two-dimensional compression of soft nanoparticles, it is interesting to extend our results to other geometries. The spherical case is of particular interest because a large body of work has been dedicated to finding and enumerating minimal energy conformations of particles constrained over a spherical shell, and

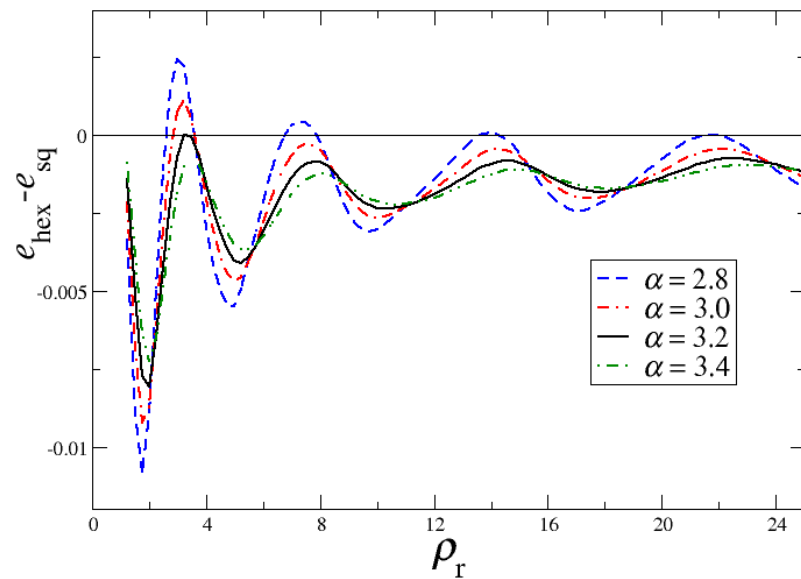


Figure 4.5: Energy density difference between hexagonal and square lattice at $T_r = 0$ as a function of system density at different values of α . The critical α is estimated to be around $\alpha \simeq 3.1822$.

repelling each other via an electrostatic repulsion [89–100].

This is what Thomson asked in 1904 [101] when attempting to construct his plum pudding model of the atom. Although there is consensus on the minimal energy structures for $N < 100$, the problem becomes more involved for large values of N for which an exponentially large number of low energy configurations becomes available. In this regime, lattices with overall icosahedral symmetry (*icosadeltahedra*) have been initially postulated as possible global minima for specific magic number of particles [95], but eventually it was shown that it is possible to lower the energy of these configurations by adding dislocation defects [98, 102]. Grain boundary scars have also been observed in experiments [103]. It is important to note that the lowest-energy structure depends only on the number of particles, not the size of the sphere on which they are fixed.

Although we confirm that the same pattern of phases obtained in two dimensions also develops on large areas of spherical shells – apart from the topologically required defects – as a function of the radius of the sphere (see Figure 4.6 for a sample of these configurations), we have not attempted to enumerate all possible low energy states for large N . It is, however, clear that considering soft potentials introduces two new parameters to the system: namely the packing density and the shape of the potential. A careful analysis of the defects and symmetries arising in this regime is the subject of future investigation; here we focus on the case of small number of particles $N \leq 12$ for $\alpha = \frac{3}{2}$ and $\alpha = \frac{5}{2}$.

Figures 4.7 and 4.8 show the results of our analysis for $N \in \{5, 12\}$. The rescaled configurational energy E , defined as the total internal energy divided by ε , and the reduced radius $r_0 = \frac{R}{\sigma}$ of the spherical surface are also given. The reference configurations for the electrostatic problem are highlighted with a dark frame.

These data are obtained using both Monte Carlo and molecular dynamics simulations with a standard temperature annealing procedure down to $T_r \rightarrow 0$. For each r_0 shown in the table, the depicted configuration was reached from at least three separate

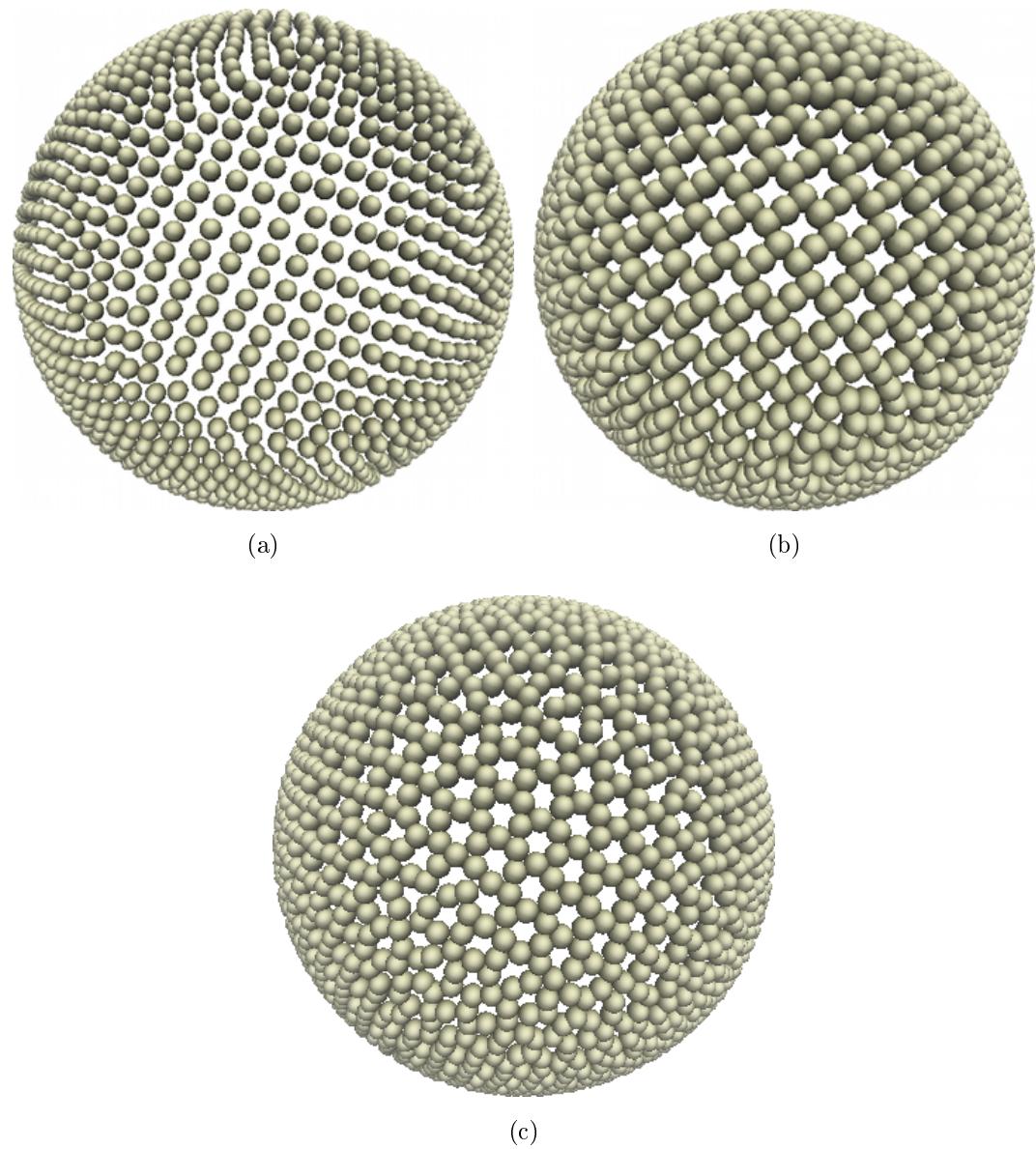


Figure 4.6: Snapshots of soft particles packing on a spherical surface. Here we show (a) square, (b) open square and (c) kagome lattices.

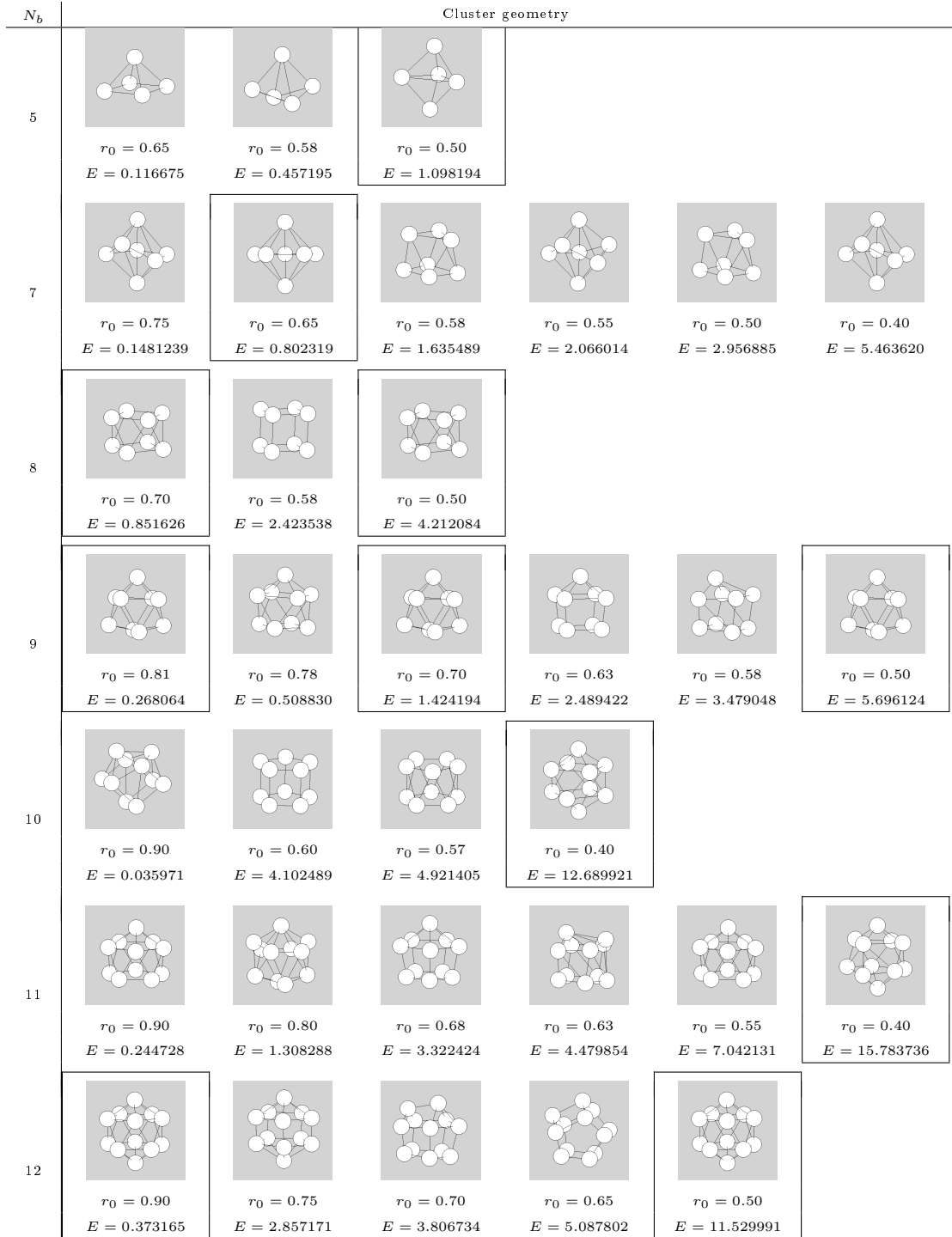


Figure 4.7: Global minima for small numbers of particles on a sphere with $\alpha = \frac{3}{2}$, with reference sphere radii and reduced energies.

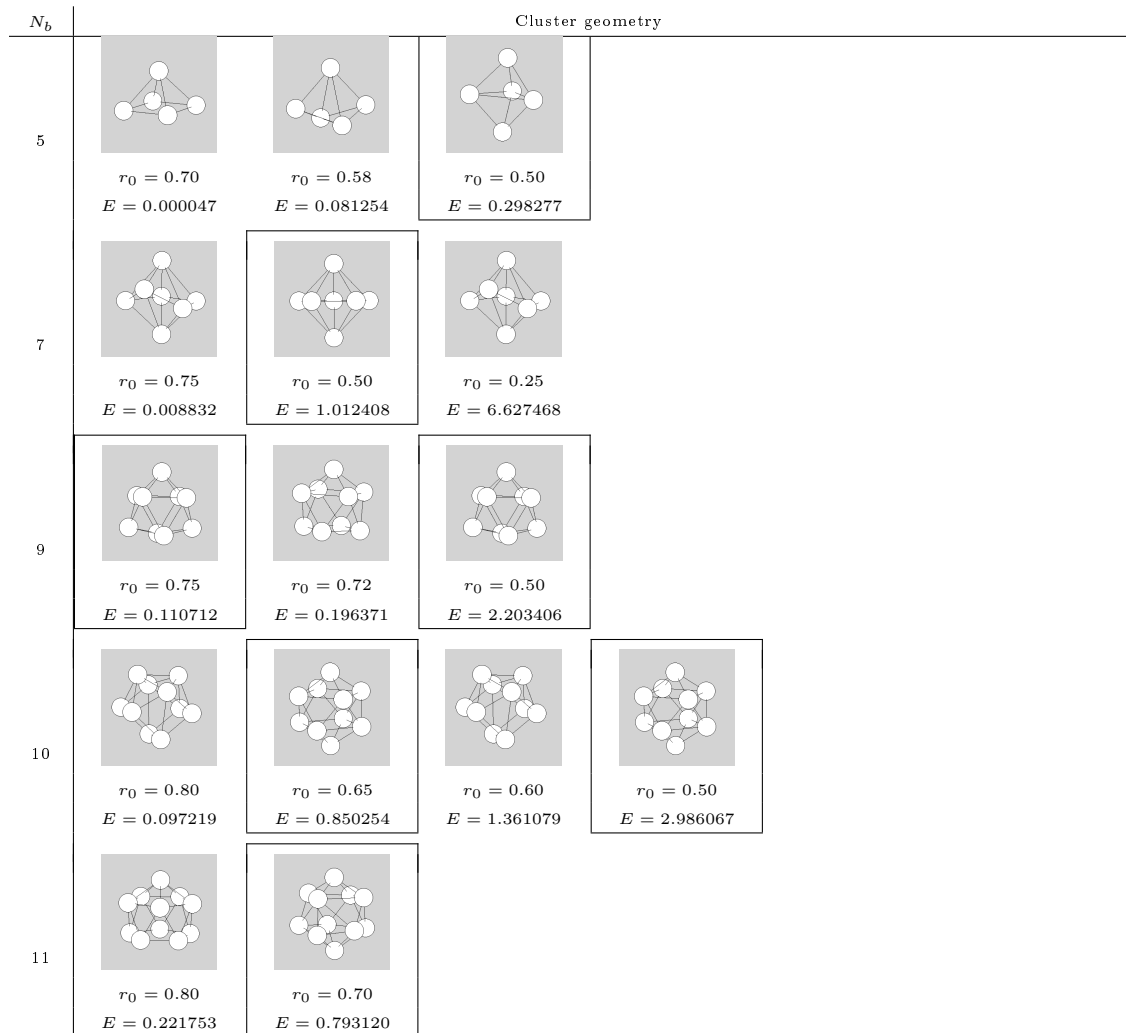


Figure 4.8: Global minima for small numbers of particles on a sphere with $\alpha = \frac{5}{2}$, with reference sphere radii and reduced energies. Reference configurations for long-range potentials have been highlighted with a dark border.

starting configurations, indicating that competing metastable states are not a major concern. Note that Figures 4.7 and 4.8 do no represent a complete enumeration of every cluster symmetry that may be obtained. They show the subset of configuration which are stable over some range of r_0 ; regions in which the particle configuration changes continuously with r_0 exist but have not been tabulated.

Unlike the case of charged point particles, we find that indeed the number and the nature of the structures is very much dependent on the radius of the sphere. The overall trend follows that found in the analysis of the planar two-dimensional system; namely, smaller values of α lead to richer structural diversity.

In all cases we were able to recover the global minima of the electrostatic system for at least one spherical radius. Interestingly, $N = 4$ and $N = 6$ are the only cases in which for both powers we obtain only one structure, a tetrahedron and a octahedron respectively (not shown), which are stable for any value of r_0 explored (down to $r_0 = 0.10$). The stability of the octahedron ($N = 6$) was also confirmed for values of α up to 10. Low energy configurations for values of N larger than 12 have also been considered, however, given the large variety and the complexity of the structures arising upon increasing N , we have not attempted to enumerate them. In fact, more sophisticated algorithms than the one used in this work would be necessary to thoroughly explore the energy landscape in search of a global minimum.

4.5 Polymers at high density: shortfalls of the Hertzian model

It is important to discuss the limits of the applicability of these generalized Hertzian models to actual physical systems. The traditional, $\alpha = \frac{5}{2}$, Hertzian model is intended to model deformable particles; in general, the class of soft potentials are used as coarse-grained models of polymers in different solvent environments.

An important consideration in evaluating the applicability of these models is the

limit in which they were derived: soft models used for both deformable particles and polymers are intended to model behavior in the *low-density limit*. Care must be taken in extending these potential to higher densities, as was demonstrated by, among others, Bozorgui *et al.* [59]. In this study, polymers tethered at one end to hard colloids were studied under external pressure, and phase diagrams were constructed.

The results of that study were compared to results obtained by Capone *et al.* [57]. It was discovered that, at reasonable densities, ideal polymer chains were modeled fairly well by Hertzian potentials; the phase diagrams qualitatively matched in this case. However, when polymers become self-avoiding rather than ideal ($\nu < 0.5$, see Section 5.3 for details), a reduction in the number of available phases occurred, and the phase behavior of this system was not well-described by a soft-sphere model.

Furthermore, as shown by Šarić *et al.* [86], there is a huge variety of phases available to soft “dumbbells” at high densities, which can be seen as a generalization of the polymer-tethered colloid model. However, this huge number of phases is not accompanied by examples of such phases in actual polymer systems, in either numerical or physical experiments.

Thus, it is important to consider the results of studies such as this and [86] in the proper context – the phase diagrams presented are for particle exhibiting the soft potentials studied *at the densities presented*. It may not be possible to directly relate the results, especially at high density, to the systems they are traditionally used to model at low density. Figure 4.9 illustrates this point with results from [59] and [86].

4.6 Conclusions

In this chapter we explore the phase behavior of model colloidal particles interacting via a generalized soft (Hertz) potential. Specifically, we analyze how structural diversity depends on the particular choice of the functional form of the potential for particles constrained on a two-dimensional plane and on the surface of a spherical

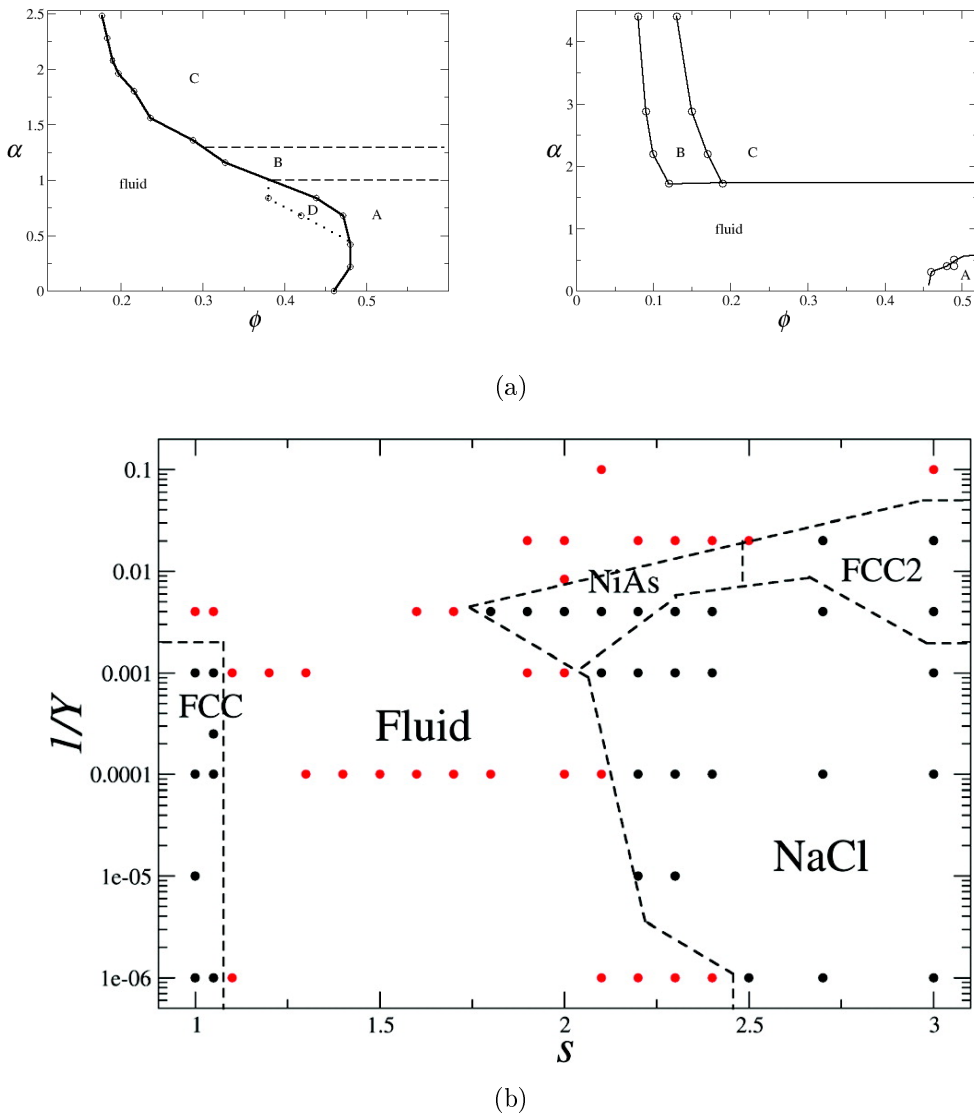


Figure 4.9: (a) Phase diagrams for ideal and self-avoiding polymers, respectively, tethered to colloids (figure used with permission from Bozorgui *et al.* [59]). The ideal polymer phase diagram is qualitatively reproducible using a soft sphere model. (b) An example of the variety of phases available to dumbbells composed of two Hertzian ($\alpha = \frac{5}{2}$) spheres – most of which do not have analogs in systems actual ideal or self-avoiding polymers (figure used with permission from Šarić *et al.* [86]).

shell. For the planar case we compute how the phase diagram of the system changes with the functional form of the pair potential, and establish a limit above which (for the class of potentials explored) hexagonal packing becomes the only allowed symmetry of the ordered phase. For small number of particles ($N \leq 12$), we identify on a spherical shell the polyhedral configurations establishing global energy minima for different pair potentials, and compare the results to the global minima corresponding to the classic Thomson problem. We show that unlike the electrostatic case, for the same number of particles the system presents more than one global minimum depending on the radius of the sphere.

It would be interesting to study the geometry of the defects arising for larger number of particles on the spherical shell, analyze the overall symmetry of the ground states, and explore whether patterns of grain boundaries, expected for large values of N in the electrostatic system, would also manifest for soft potentials. This is a very challenging problem that we have already begun to investigate and requires more sophisticated minimization techniques than the ones employed in this study. For the time being, we have established that the same phases observed in the planar geometry do develop on the spherical shell at comparable number densities.

Finally, given the sensitivity of the phase behavior on the specific choice of the pair potential, it becomes critical at this point to develop sophisticated and reliable coarse-graining procedures able to capture accurate interactions between dendrimers or star polymers, but also the inverse problem, i.e. the design of polymeric structures able to reproduce desired functional forms for the pair potential, is in great need of a better theoretical understanding.

Chapter 5

Free energy of alternating two-component polymer brushes on cylindrical templates

5.1 Introduction

Polymer brushes are highly tunable systems that have recently attracted considerable attention in the scientific community. This is mainly due to the already large number of technological applications in which they are used, but also to the promising role these materials hold for the future. Apart from their well known role in the stabilization of colloidal particles [104], polymer brushes are also used as lubricants, in chromatographic devices, and in adhesives, and their use has recently been proposed in a variety of biotechnological applications including drug delivery and drug-biocompatibility enhancers [105–108]. Generally speaking, they offer an ideal platform that provides control over the physical and chemical properties of solid and fluid surfaces.

Polymer brushes are basically dense systems of polymer chains having one end tethered to a non-adsorbing surface, and they have been thoroughly studied the-

oretically and numerically on different geometries (see [54, 109–117] and references therein). The equilibrium properties of these systems typically depend on the molecular weight of the chains, their grafting density, and the quality of the solvent. Although we have a good qualitative understanding of homogeneous and single-component brushes, for which scaling arguments have been successfully put forward, the problem becomes very complex as soon as we deal with heterogeneous systems with multicomponent or nonlinear chains [118, 119].

Of particular relevance for the present chapter is the work done by Stellacci and collaborators [120–124] where basically a two-component brush of immiscible ligands having different length has been shown to phase separate into striped phases of different widths when anchored to spherical and cylindrical templates. What is surprising is not the phase separation in itself, but rather the formation of the striped phase and its poorly-understood dependence on the mismatch in polymer length. Microphase separation is also expected in more traditional mismatched two-component polymer brushes [125], where potential applications in stimuli-responsive systems and nanotemplating have recently attracted great attention to the field (see ref [126] and references therein). Being able to control pattern formation at the nanoscale is a core element in the production of novel materials via the process of self-assembly.

Direct coarse grained molecular dynamics simulations by Glotzer *et al.* have clearly indicated the driving forces behind the formation of these phases as the difference between the chains' molecular weight, and the overall height of the brush itself [121, 123, 124, 127, 128]. Very recently, a coarse-grained model for two-component polymer mixtures of different length has also been put forward, and the formation of different phases as a function of length mismatch on a planar geometry has been analyzed, revealing the presence of striped phases in these systems as well [125].

Unlike other numerical work that focused on the details of the demixing transition, in this paper we focus exclusively on the origin of the microphase separation. We use

numerical simulations to compute free energies of an inhomogeneous two-component polymer brush to understand how molecular weight and overall brush height affect the stability and width of the striped phases. Specifically, we focus on the case of a cylindrical solid template where stripes have been shown to form promptly both numerically and experimentally [124, 128], and we compute, at constant grafting density and template radius, how the system free energy changes when imposing stripes of different width and height on the template. Our results indicate that what limits macrophase separation into a two-phase region, thus leading to the stabilization of the striped phase, is the elastic strain that builds up in the polymer brush formed by the mismatched (exposed) polymer segments.

Note that this system does not as straightforwardly fit into the framework of anisotropy space discussed in Section 1.3 as the previous chapters of this dissertation. In this case, rather than simple hard spheres or something similar, one can imagine that the origin of the space is a one-component polymer brush consisting of polymers with one monomer each on a cylinder; the axes of interest include the lengths of the two different types of polymers and the stripe width.

5.2 Simulation details

To ensure that our data are not affected by the lateral tension due to the immiscibility of the two polymer types, and that we are indeed measuring exclusively the free energy difference arising from the chains' length mismatch and overall brush morphology, we simulate systems in which the only difference between the two polymer types is their length. This is equivalent to setting the line tension between the stripe's boundaries that comes directly from the immiscibility term in the pair potential between the two polymer types equal to zero. As a consequence, we are required to lock in place the position of the anchoring monomers to prevent the different chains from trivially mixing – as will be shown below, the striped configuration with the lowest free energy,

for all chain length combinations, is alternating stripes of width unity.

Polymers are modeled as sequences of spherical beads of radius σ linearly connected via a harmonic potential

$$V_{\text{bond}}(r) = \kappa \left(\frac{r}{\sigma} - 1 \right)^2, \quad (5.1)$$

with $\kappa = 800k_B T$. Any two monomers in the system interact via the soft and purely repulsive dissipative particle dynamics (DPD) simulation potential:

$$V^{ij}(r_{mn}) = \begin{cases} \epsilon_{ij} \left(1 - \frac{r_{mn}}{\sigma} \right)^2 & \text{if } r \leq \sigma \\ 0 & \text{otherwise} \end{cases}, \quad (5.2)$$

where i and j indicate the identity of the polymer $i, j \in \{1, 2\}$ and $m, n \in \{1, N_i\}$ refers to the identity of the monomer. Here N_i is the length of a polymer of type i .

All the results that follow use $\epsilon_{11} = \epsilon_{22} = \epsilon_{12} = 5k_B T$. Each polymer is grafted to a fixed point on the outer surface of a cylindrical template of radius $R = 2.5\sigma$ via the same harmonic potential tethering the consecutive monomers in a chain. In all our simulations we considered a total number of polymers $n_p = 2580$ arranged in a homogeneous grid having square symmetry. The polymer identity is finally selected to generate alternating stripes of width L_p .

For a lateral grafting density of the polymers equal to $2.74/\sigma$, our system contains 60 one-polymer-wide rings, making the possible values of $L_p \in \{1, 2, 3, 5, 6, 10, 15, 30\}$, when equal number of polymer types are considered $n_p^{(1)} = n_p^{(2)} = \frac{n_p}{2}$. Figure 5.1 shows snapshots of typical initial and equilibrium configurations for $L_p = 6$ and $L_p = 30$. This particular geometry is selected because we find that unconstrained test simulations of immiscible chains always lead to stripe formation perpendicular to the cylindrical axis. This result has also been observed in [128].

Given the size of the system we carried out our simulations using the molecular dynamics package LAMMPS [129], which efficiently handles molecular dynamics simulations of thousands of particles. All simulations were performed using Langevin

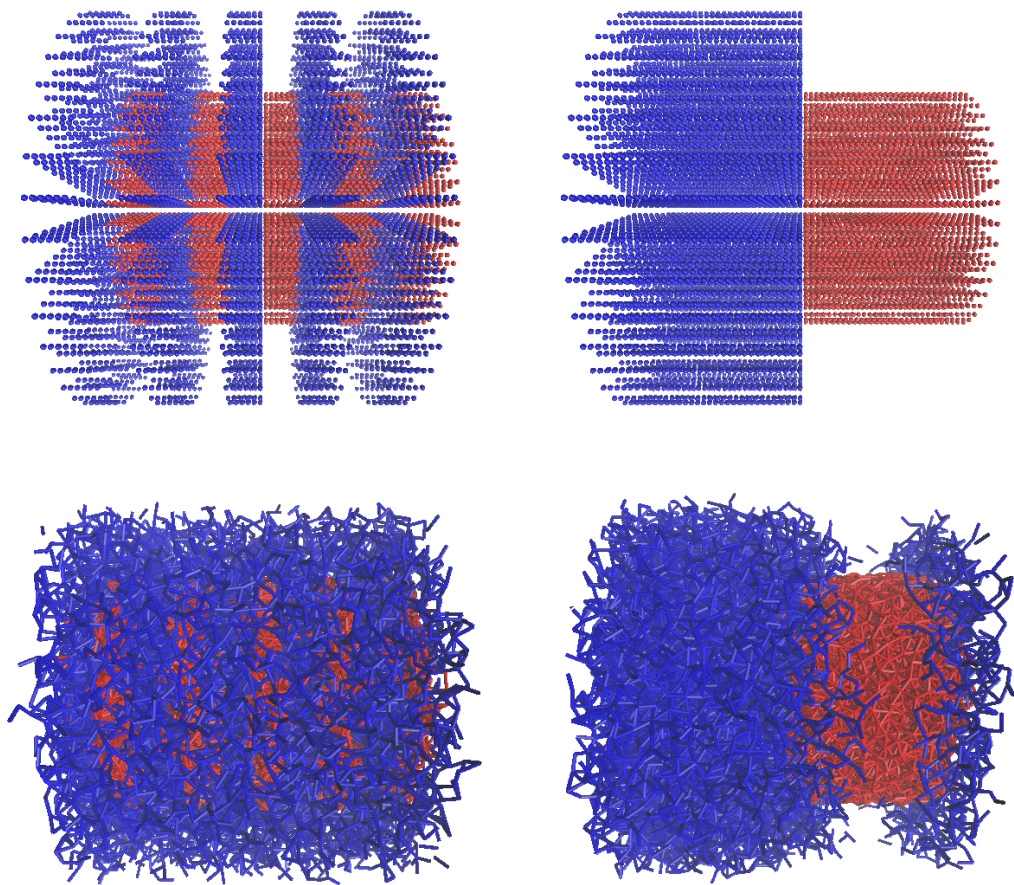


Figure 5.1: Snapshots of typical (top) initial and (bottom) equilibrium configurations for $L_p = 6$ and $L_p = 30$, respectively. The blue polymers are 20 and the red are 10 monomers long.

dynamics in the NVT ensemble. Dimensionless units are used throughout this chapter. The time step size was set to $dt = 0.0025\tau_0$ (τ_0 is the dimensionless time).

Our goal is to compute the free energy difference $\Delta F(L_p)$ between systems having different stripe width L_p , while keeping everything else unaltered, as a function of the polymer lengths N_1 and N_2 . We will perform these calculations using the thermodynamic integration method described in Section 1.4.2

In this particular case, the reference system is the ideal system in which polymers are tethered to the surface but do not interact with one another, and the fictitious potential V_λ between monomers is given by

$$V_\lambda^{ij}(r_{mn}) = \lambda \begin{cases} \epsilon_{ij} \left(1 - \frac{r_{mn}}{\sigma}\right)^2 & \text{if } r_{mn} \leq \sigma \\ 0 & \text{otherwise} \end{cases}, \quad (5.3)$$

where i, j, m and n are defined as in Equation 5.2. Thus, the total potential of the system is

$$V_{ij} = V_{\text{id}} + \sum_{m \neq n} V_\lambda^{ij}(r_{mn}) \equiv V_{\text{id}} + V_\lambda, \quad (5.4)$$

where V_{id} is the total energy of the ideal reference system and V_λ is the total potential due to interparticle interactions.

For $\lambda = 0$ the chains are ideal and the system free energy is independent of the specific grouping of the polymer types; as $\lambda \rightarrow 1$, we recover the system of interest. The free energy of the full system with respect to the ideal system can then be extracted by performing the integration in Equation 1.21

We perform simulations for several values of λ (for example, $\lambda \in \{0, 0.1, 0.2, 0.4, 0.6, 0.8, 1\}$) and numerically compute the integral above by fitting the resulting points to a polynomial.

5.3 One-component systems: $N_2 = 0$

To get insight into the problem we first consider the case in which $N_2 = 0$; that is, only one chain type is present in the system. Figure 5.2a shows our numerical data

for the free energy cost $F(L_p)$ associated with the partitioning of the two polymer species into alternate stripes of different L_p on a cylinder of radius 2.5σ and lateral grafting density $2.74/\sigma$, as a function of L_p and for polymer lengths $N_1 \in [10, 30]$ and $N_2 = 0$.

This specific lateral grafting density was selected because unconstrained simulations under this condition lead to prompt microphase separation for moderate values of polymer immiscibility. Furthermore, a sufficiently large value of lateral grafting density guarantees large enough differences in free energies as a function length mismatch; widely-spaced polymers would yield free energy differences that were too small to measure effectively.

Our data show that the most favorable state corresponds to that having the largest number of stripes (i.e. the smallest value of L_p). The inset on the same figure shows how the free energy difference $\Delta F^{\max} \equiv F(L_p = 30) - F(L_p = 1)$ grows with the length of the chain N_1 . These results can be qualitatively understood by referring back to the theory of polymer brushes on flat surfaces and its extension to spherical and cylindrical surfaces [111, 130].

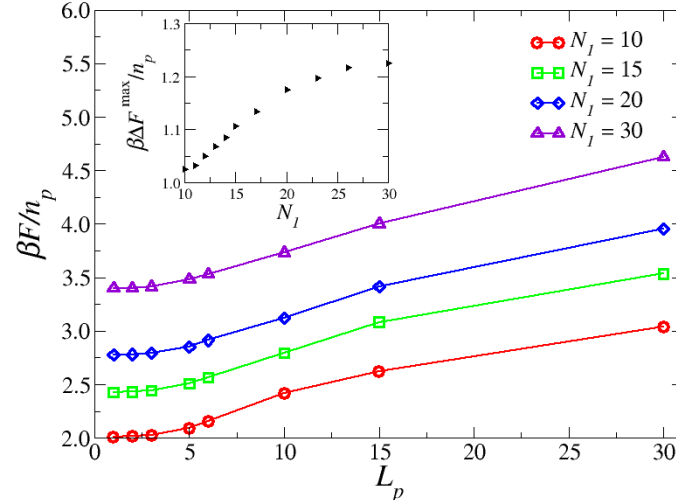
The key point is that the main contribution to the free energy cost per chain associated with a polymer brush has an inverse dependence on the lateral chain-to-chain grafting distance D_0 :

$$F_{\text{cyl}} \simeq 2k_{\text{B}}T \left(\frac{R}{D_0} \right) \left[\left(1 + \frac{4h_0}{3R} \right)^{3/8} - 1 \right], \quad (5.5)$$

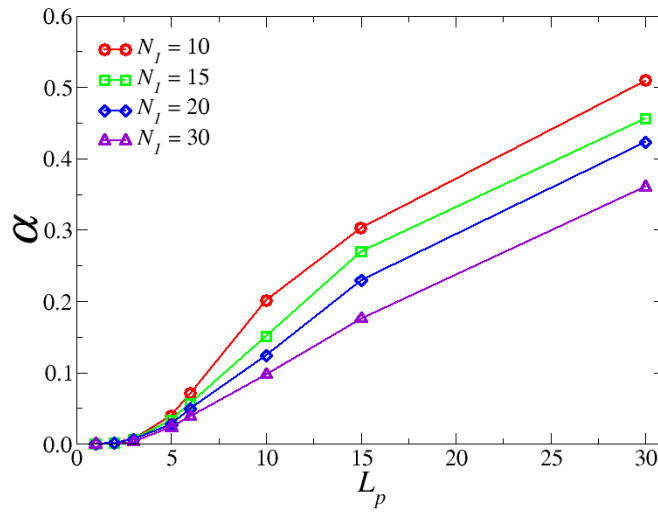
where $h_0 \sim \sigma N D_0^{-2/3}$ is the height of a brush made with polymers of length N grafted on a planar surface, σ is the monomer radius, and R is the cylinder radius.

Although in our system the location of the grafting lattice on the cylindrical surface is independent of L_p and therefore the total grafting density of the system is kept constant at all times, different distributions of the chains on the lattice result in different local densities.

Crucially, when considering the free energy contribution due to the different lateral



(a)



(b)

Figure 5.2: (a) Free energy per polymer $\frac{F}{n_p}$ vs. L_p for a cylinder of radius 2.5σ , for various values of $N_1 \in [10, 30]$ with $N_2 = 0$. Each line represents a different value of N_1 ; increasing N_1 leads to an increase in free energy F at every value of L_p . The inset shows how the free energy gap ΔF^{\max} defined as the free energy difference between $L_p = 30$ and $L_p = 1$ depends on the overall length of the chains N_1 . (b) The same data plotted as $\alpha = \frac{F(L_p) - F(1)}{F(1)}$ vs. L_p .

organization of the chains, one can consider our system with $L_p = 1$ as a polymer brush with twice the lateral grafting distance of that relative to $L_p = 30$. Clearly the latter system cannot be straightforwardly described with Equation 5.5 due to the free boundaries of the brush. The chains near the boundary between the region containing polymers and the empty region can relax laterally into the empty space, decreasing the free energy; nevertheless, we expect that for $L_p \rightarrow \infty$ the role of the boundary should become negligible.

If we now introduce the dimensionless parameter $\alpha(L_p)$ defined as

$$\alpha \equiv \frac{F(L_p) - F(1)}{F(1)}, \quad (5.6)$$

the argument above leads to clear upper bounds on the value of α .

Substituting Equation 5.5 into Equation 5.6, we obtain, for the limit $L_p \rightarrow \infty$, the following expression for α_{\max} :

$$\begin{aligned} \alpha &= \frac{2(1+A)^{3/8} - (1+2^{-2/3}A)^{3/8} - 1}{(1+2^{-2/3}A)^{3/8} - 1} \\ &= 2 \left[\frac{(1+A)^{3/8} - 1}{(1+2^{-2/3}A)^{3/8} - 1} \right] - 1, \end{aligned} \quad (5.7)$$

where $A = \frac{4h_0^\infty}{3R} = \frac{4\sigma ND^{-2/3}}{3R}$. Consider the two limits: the flat plane ($R \rightarrow \infty$) and the narrow cylinder ($h_0 \gg R$).

In the flat plane limit, we have $h_0 \ll R$, so $A \ll 1$. Thus, we can Taylor expand each term in Equation 5.7 to first order in A :

$$\begin{aligned} \alpha &\simeq 2 \left[\frac{1 + \frac{3}{8}A - 1}{1 + \frac{3}{8}2^{-2/3}A - 1} \right] - 1 \\ &= 2 \left[\frac{1}{2^{-2/3}} \right] - 1 = 2^{5/3} - 1. \end{aligned} \quad (5.8)$$

In the opposite limit, when the cylinder is very narrow, we have $h_0 \gg R$ and thus $A \gg 1$; in this case, Equation 5.7 can simply be estimated

$$\begin{aligned} \alpha &\simeq 2 \left[\frac{A^{3/8} - 1}{2^{-1/4}A^{3/8} - 1} \right] - 1 \simeq 2 \left[\frac{A^{3/8}}{2^{-1/4}A^{3/8}} \right] - 1 \\ &= 2 \left[\frac{1}{2^{-1/4}} \right] - 1 = 2^{5/4} - 1. \end{aligned} \quad (5.9)$$

We find that our numerical results are, indeed, within these bounds of $\alpha_{\max} = 2^{5/3} - 1$ and $\alpha_{\max} = 2^{5/4} - 1$.

Figure 5.2b shows α plotted as a function of L_p for different values of N_1 . α has a nontrivial dependence on L_p ; nevertheless, simple geometrical arguments can be used to understand, at least qualitatively, the overall behavior of these curves. Figure 5.3 shows a sketch of the expected chain distributions for $L_p = 1, 2$ and 4 for the simpler case of a flat surface. For small values of L_p the problem is dominated by boundary effects, and we can imagine the chains equally sharing the overall space $2L_p$ per stripe available to them.

It is immediately obvious that the free energy difference between $L_p = 1$ and $L_p = 2$ per chain should be very small indeed. In both cases the chains can be accommodated into space as a sequence of blobs of diameter equal to twice the grafting distance D . A similar argument can be made for $L_p = 4$. The main extra cost in free energy per polymer for a growing L_p should come from the weak entropic stretching of the polymers next to the grafting surface; in the weak limit, the stretching energy follows Hooke's law and grows as the square of the stretching distance, which is proportional to L_p in this case; thus, the free energy for small L_p should weakly grow as L_p^2 .

When L_p becomes large, the free energy of the system is dominated by chains in the bulk of the stripe. In this regime the blob size of the outer chains is larger than that of the inner chains. Assume that each chain in the polymer brush behaves roughly as a polymer confined in a cylinder (where the surrounding polymers act as the cylinder's walls). Then, as shown in Figure 5.3, a chain may be visualized as a series of blobs of diameter D , and the free energy of confinement may be estimated, following de Gennes [54].

The radius of gyration, R_G of a polymer is a measure of the size of an unconstrained polymer, defined as

$$R_G \equiv \frac{1}{N} \sum_{k=1}^N (\mathbf{r}_k - \mathbf{r}_{\text{com}})^2, \quad (5.10)$$

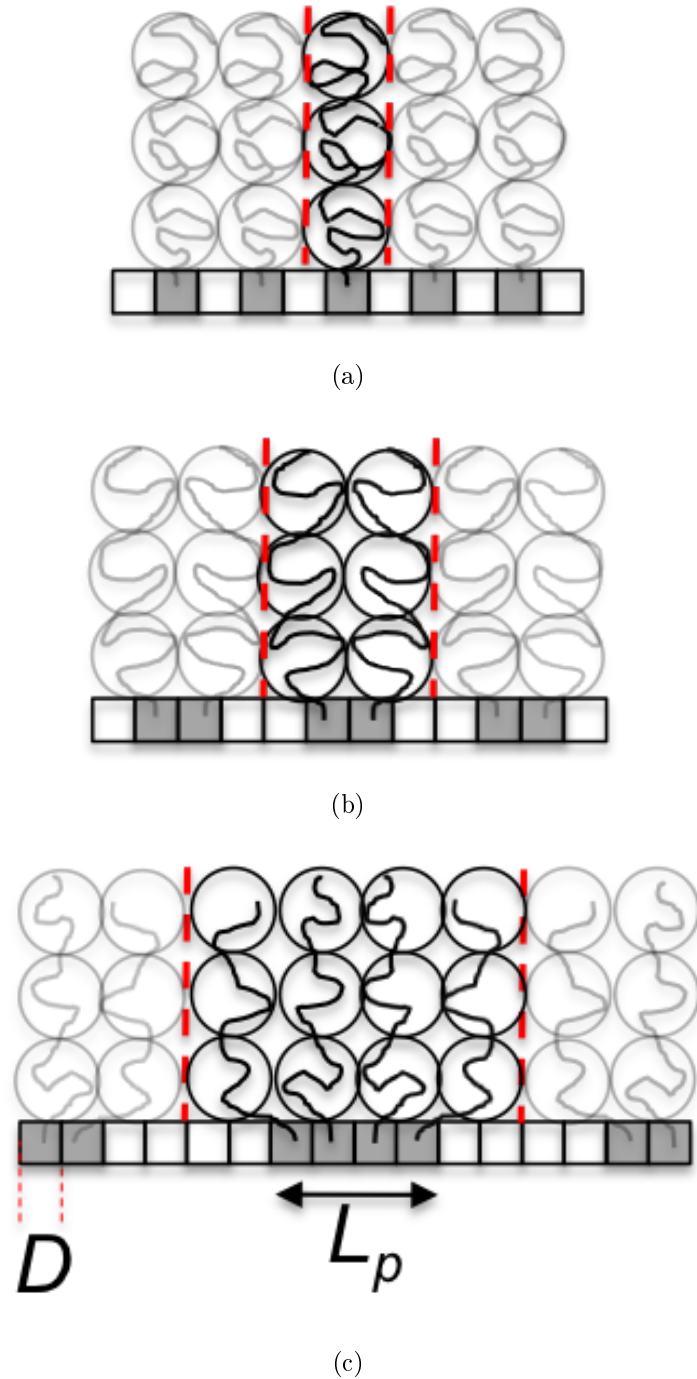


Figure 5.3: Sketch of expected chain configurations for L_p = (a) 1, (b) 2, and (c) 4.

where N is the polymer length, the \mathbf{r}_k are the monomer positions, and \mathbf{r}_{com} is the center of mass of the polymer. The radius of gyration for a given polymer can be approximated by

$$R_G \simeq \sigma N^\nu, \quad (5.11)$$

where σ is the monomer diameter and ν is an exponent particular to the polymer and its surroundings; for real chains in good solvent, $\nu = \frac{3}{5}$, and in bad, $\nu = \frac{1}{3}$. The actual ν for a given polymer varies between those two values depending on the solvent; this means there is some solvent, known as the θ solvent, in which $\nu = \frac{1}{2}$ and the polymer behaves as if it were an ideal polymer with R_G simply the result of a random walk.

Assume that the free energy of confinement of a given blob depends only on the temperature and the ratio $\frac{R_G}{D} \equiv x$. In the limit $x \rightarrow \infty$ (very highly confined polymers), the polymer becomes fully extended, and thus the free energy must be a linear function of N . But $x \propto N^\nu$; so the free energy $F \propto x^{1/\nu}$:

$$F \simeq k_B T \phi \left(\frac{R_G}{D} \right) \simeq k_B T \left(\frac{R_G}{D} \right)^{1/\nu} \simeq k_B T N \left(\frac{\sigma}{D} \right)^{1/\nu}. \quad (5.12)$$

Assuming a generic size profile for the blobs of the form $D(i) = D(1 + c i^\beta)$ where $i \in [1, L_p]$ and c is fixed by the constraint $\sum_1^{L_p} D(i) = 2D_0 L_p$, one can estimate the free energy per stripe (referring to Equation 5.12) as

$$F_s \simeq k_B T N_1 \sigma^{1/\nu} \sum_1^{L_p} \frac{1}{D(i)^{1/\nu}}. \quad (5.13)$$

Given that there are $\frac{n_p}{L_p}$ polymers in each stripe, the free energy per particle on a flat interface reads as

$$F \simeq k_B T N_1 \frac{\sigma^{1/\nu}}{L_p} \sum_1^{L_p} \frac{1}{D(i)^{1/\nu}}. \quad (5.14)$$

It is difficult to extract β from our simulations, but from visual inspection of the brush profiles one should expect $\beta \geq 2$, leading to functional forms for F having the typical saturating behavior shown in our data.

In the current form the data do not collapse onto a universal master curve. In fact, the free energy difference of shorter chains tends to grow faster than that of

the longer ones. This result is quite revealing as it directly reflects on the nontrivial interactions between neighboring regions of grafted polymers.

Such interactions will cease as soon as the mutual distance between two neighboring regions is larger than twice the side spread of the polymers at the boundaries. Clearly this will happen sooner for the short polymer than for the longer ones. We should be able to account for this difference by rescaling of L_p by $\frac{L_p}{N_1^\gamma}$. We find the best collapse for $\gamma = 0.4$.

This result suggests a length-scale, h_B , controlling the extent of the side interactions that scales as

$$h_B = \frac{h_0}{N_1^{0.4}}, \quad (5.15)$$

which means that h_B is can be roughly approximated as $h_B \simeq \frac{\sigma h_0}{R_G}$. Figure 5.4 shows the data collapse into a universal master curve $\alpha = \tilde{\Phi}\left(\frac{L_p}{h_B}\right)$ with h_B defined as in Equation 5.15.

5.4 Two-component systems: $N_2 \neq 0$

We now turn our attention to the case in which $N_2 \neq 0$. It would be desirable to develop a simple way of extending our results to the more general $N_2 \neq 0$ case. In particular, we are interested in understanding whether it is possible to map a system having different polymer lengths $N_1 > N_2 \neq 0$ to a system of a single polymer type of length $N'_1 = N_1 - N_2$ (and $N'_2 = 0$.)

Figure 5.5 shows α as a function of L_p/h_B for different values of N_1 at $N_2 = 5$ and $N_2 = 10$. The results for $N_2 = 0$ are also shown as a reference. As the cause for the free energy gap between the different configurations rests in the difference $N_1 - N_2$, to properly compare the data coming from systems having different values of N_2 , when computing α we subtracted from the measured free energies $F(L_p)$ the constant core free energy of the underlying full brush of height N_2 , $F_{\text{core}}(N_2)$. When $N_2 \neq 0$, we

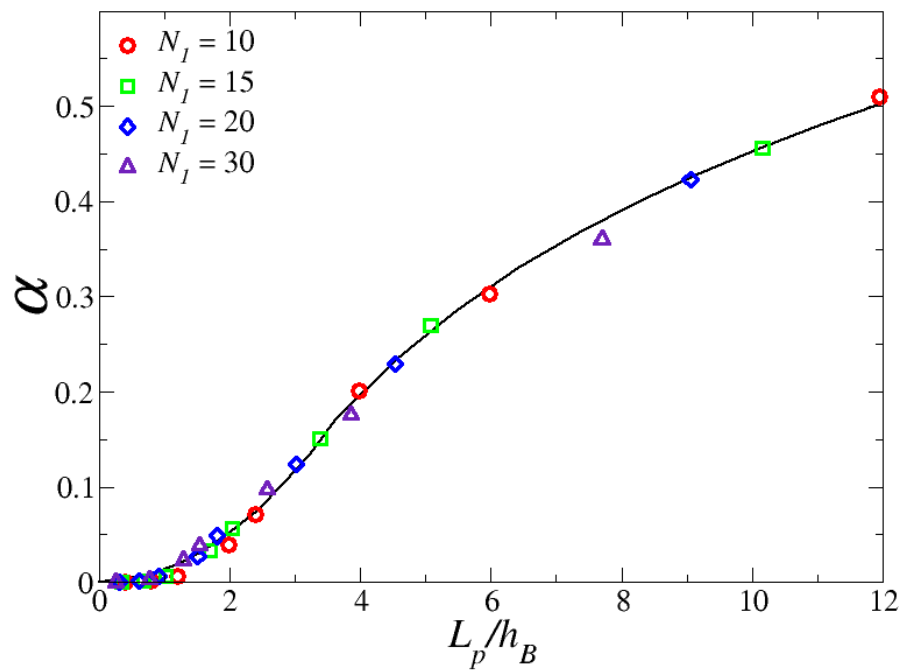


Figure 5.4: α vs. the rescaled $\frac{L_p}{h_B}$. The black line is a guide to the eye.

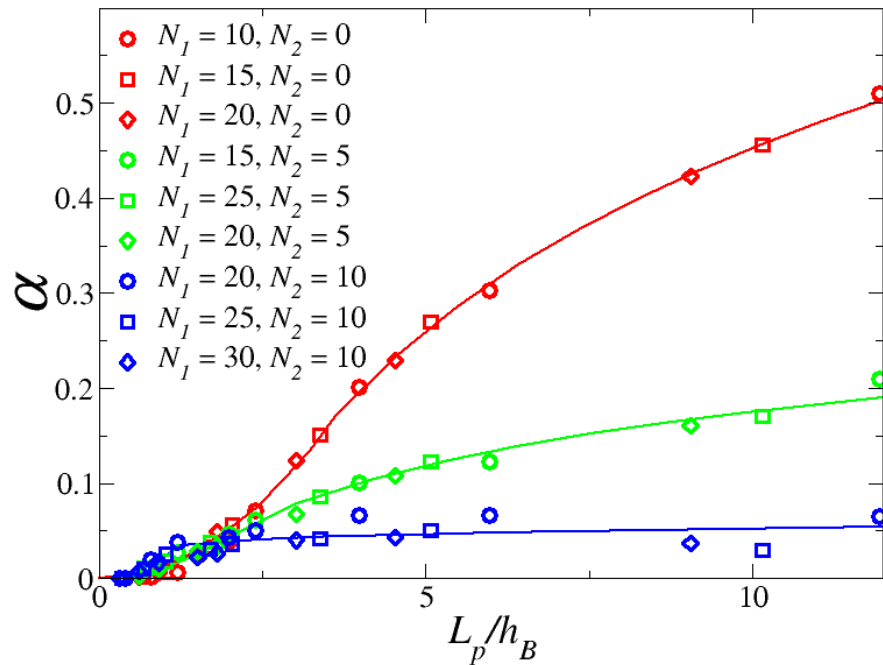


Figure 5.5: α vs. the rescaled $\frac{L_p}{h_B}$ for different values of N_2 . The different colors represent different values of N_2 . The lines are guides to the eye.

define α as

$$\alpha(L_p) = \frac{F(L_p) - F(1)}{F(1) - F_{\text{core}}(N_2)}. \quad (5.16)$$

It is possible to systematically collapse all of the data corresponding to different values of N_1 at a given (fixed) N_2 into unique curves; however, we cannot collapse data coming from different values of N_2 . This result clearly points to the fact that the universal curve previously described for $N_2 = 0$ also has a nontrivial dependence on N_2 : $\tilde{\Phi} = \tilde{\Phi}\left(\frac{L_p}{h_B}, N_2\right)$.

In principle, this shouldn't come as a surprise for brushes grafted on a curved surface; in fact, the effect of the "interior" layer of N_2 monomers is to increase the effective radius of the cylinder to which the reduced system would be grafted, and to decrease the grafting density of the effective brush of length $N_1 - N_2$; both are variables on which the free energy depends (see Equation 5.5).

Simple geometrical arguments can be used to estimate the change in lateral grafting distance. Following [130], we can write the change in lateral grafting spacing as we radially move away from the cylinder surface of an amount r as $D(r) = D_0 \left(\frac{r}{R}\right)^{1/2}$. For short polymers and at the relatively high densities of our systems (so that the polymers are almost completely elongated), we have $r \simeq R + \sigma N_2$. It follows that

$$D(r) = D_0 \left(1 + \frac{\sigma N_2}{R}\right)^{1/2}. \quad (5.17)$$

Simultaneously, the effective polymer of length $N_1 - N_2$ would be grafted onto a cylinder of radius $R' \simeq R + \sigma N_2$. The ratio $\frac{R'}{\xi}$ appearing in the brush free energy should then be adjusted to

$$\frac{R'}{\xi(r)} \rightarrow \frac{R}{D} \left(1 + \frac{\sigma N_2}{R}\right)^{1/2}, \quad (5.18)$$

introducing a predictable dependence on N_2 in the problem. Although this argument suggests an overall increase in free energy for the system at a given L_p , it isn't obvious how it will affect the dimensionless ratio $\alpha(L_p)$. Clearly this correction should factor out in the large R limit or for $h_0 \gg R$.

Our numerical data show that α is quite sensitive to N_2 . Specifically, $\alpha(L_p)$ tends to flatten as N_2 increases. This is most likely explained by the fact that the base of the effective chain of length $N_1 - N_2$ is not really grafted in place, but the layer of polymers below allows for significant reorganization of the base due, for instance, to their compressibility.

Because the blobs in the polymer become larger on a convex template as one moves away from the surface, they also become more laterally compressible as N_2 is increased. The net result is a flattening of the free energy difference as a function of L_p . Unfortunately, we find that our data for different values of N_2 cannot be collapsed by a simple rescaling of the free energy with a power of N_2 , indicating a subtle interplay between $F(L_p)$ and the height of the bottom layer.

5.5 Conclusions

In summary, we have analyzed the relative stability of the striped phases arising from the demixing of immiscible polymers on a cylindrical template as a function of the width of the stripe, the length mismatch between the chains, and the overall length of the brush. We set numerical bounds for the free energy gap between an alternating (many thin stripes) and a fully demixed (two wide stripes) phase, and found that indeed the former becomes more and more favorable as the mismatch between the chains' lengths, ΔN is increased.

We also found that when appropriately normalized the free energies as a function of stripe width for different values of ΔN can be collapsed into unique master curves that only depend on the overall length of the lower brush N_2 . Finally we discussed the possibility of reducing a two-component system of chains having lengths $N_1 > N_2$ into a simpler single component system of chains of length ΔN . Our results are fully consistent with previous molecular dynamics simulations on this problem in identifying the key parameters setting the width of the stripes in the polymer length

mismatch $N_1 - N_2$, and the overall length of the shorter brush N_2 together with the degree of chain immiscibility.

In all our data the direct line tension γ coming from the pair potential between chains of different types has been set to zero. To first order, one might predict an addition to the free energy of the type

$$F_l(L_p, N_2) \simeq \gamma h_0(N_2) \left(\frac{N_p}{L_p} \right), \quad (5.19)$$

where $h_0(N_2)$ is the height of the polymer brush formed by the lower chains and $\frac{N_p}{L_p}$ is the number of phase boundaries. Preliminary work in this area indicates that contribution is not so straightforward; there is likely a much more complex interplay as polymers at the edges reconfigure themselves to increase their distance from the neighboring chains of the other type, resulting in a decrease in the line energy but also an increase in the free energy due to compression of the chain within each stripe.

Regardless, clearly $F_l(L_p, N_2)$ has a minimum for $L_p \rightarrow \infty$ and is large for small L_p . The balance between the line tension and the configurational free energy computed in this paper should therefore set the width of the stripe. More work in this direction is currently underway.

Chapter 6

Exploiting classical nucleation theory for reverse self-assembly

6.1 Introduction

Not only is understanding, controlling and predicting the phenomenological behavior of particle self-assembly one of the great mathematical challenges for the twenty-first century, but its applications in materials science and engineering hold promise for the development of materials with novel electronic, mechanical, and optical properties. Although most of the work performed in this field is historically rooted in the self-assembly of small molecules, the last decade has witnessed extraordinary advances in particle synthesis at the mesoscale [2–6], making possible the production of building blocks with complex chemical and geometrical properties with an unprecedented degree of precision. Unfortunately, a coherent theoretical framework around the problem of self-assembly is still missing, and numerical simulations have taken the lead in exploring the wealth of new phenomenological behavior arising from the collective behavior of nonisotropic components.

Most numerical studies on self-assembly of nanoparticles performed so far have adopted the patchy sphere model [131]. In this model, the isotropicity of a particle is

broken by placing on its surface regions (patches) with different physical properties; for example, hydrophobic chemical groups or single-stranded DNA chains. Theoretically, these regions are incorporated into the interparticle potential by a simple angular dependence which favors or disfavors the alignment of such patches – in practice, the patchy sphere model can be thought of as a generalization of the amphiphilic model used in Chapter 2 to include more than one hydrophilic region.

Although self-assembly of several simple structures has been achieved with patchy models (references [26, 52, 132] are just a few examples of the large body of work published on the subject; for a recent review see references [133, 134]), a general modeling approach to the problem is missing. Shape and position of the interaction sites is either guessed using physical arguments, or inspired by known molecules or protein structures aggregating into a similar target crystal.

There are three notable exceptions. Torquato [50] proposed an inverse optimization technique. In this technique, an isotropic (two-dimensional) interaction potential is sought by choosing a family of functions $\phi(r; a_0, a_1, \dots, a_n)$, parametrized by the a_i s. Reverse self-assembly is achieved either by choosing an objective function such that the energetic stability of the target crystal is maximized with respect to competitor lattices (“zero-temperature”) or by running finite temperature simulations and minimizing the Lindemann parameter Θ_2 . The success of this method relies on a suitable choice of ϕ . Furthermore, this technique is specific to nondirectional interactions, and while examples are provided of such potentials yielding complex and surprising self-assembled structures, these potentials are sufficiently complicated that they are not achievable experimentally.

Additionally, Jankowski and Glotzer have developed so-called “bottom-up building block assembly,” or BUBBA [135, 136]. This method requires the construction of the entire self-assembly pathway up to the target structure, and thus is primarily applicable to simple cases in which particles interact in a very defined way, such as the so-called tetrominoes on a grid, for which it has been demonstrated. Further-

more, BUBBA requires construction of the partition function of the system, starting from individual particles; while the authors have demonstrated in [136] a method for choosing the most relevant terms of the partition function and thus reducing the computational complexity, the degree of allowable complexity is currently very low.

Finally, Hormoz and Brenner [137] have described a method by which the yields of specific, finite clusters (for example, a tetrahedral T_d cluster) can be enhanced by using nonidentical spheres. In the case of a T_d cluster, eight different particle types are used, and an 8×8 matrix of particle interaction energies is constructed. Given this matrix, the total energy of all possible configurations of eight-particle clusters given those interparticle interactions are calculated (totalling 504,000 configurations for eight-particle clusters). The optimal set of particle interactions is the one in which the desired cluster is the ground state and the standard deviation σ is less than some critical value (set by the parameters of the system). While this method is useful for designing interactions for yielding finite structures, it has a similar limitation to the BUBBA method: it requires the enumeration and energy calculation of all possible competing structures, which is unfeasible for even moderately complex or large structures.

The development of an efficient numerical procedure to design interactions between nanoparticles that targets specific crystal structures via the process of self-assembly would therefore be a result of great importance.

As discussed in Chapter 2, while the generic features of particle aggregation can be described in terms of simple thermodynamic arguments, the details of the process can be very complex and multi-faceted. In fact, a full theoretical description of this problem must incorporate critical kinetic effects which are not captured by classical thermodynamics, and which have dramatic macroscopic consequences [26, 38, 138].

It is now understood that for self-assembly to take place, a very delicate balance between entropic and energetic contributions, coupled to a precise geometric character of the components, must be satisfied. In general, self-assembly of nanocomponents is

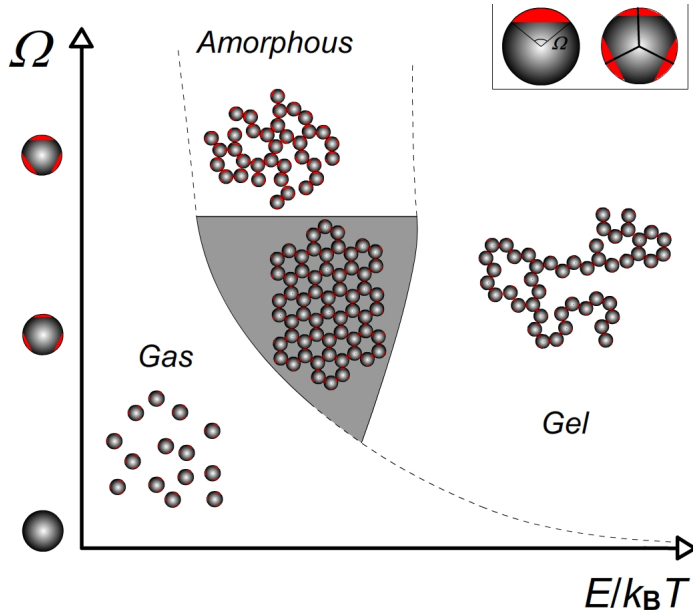


Figure 6.1: Illustration of a generic self-assembly diagram for patchy spherical particles expected to aggregate into a honeycomb lattice. E is the interparticle attraction strength and Ω is the angular size of the patches.

not to be expected unless a careful design of the building blocks has been performed beforehand [26, 38].

Figure 6.1 illustrates the problem for a simple model: spherical particles with attractive patches oriented to form a two dimensional honeycomb lattice. When the angular size Ω of each patch is too large, the interaction is not specific enough to select the desired crystal, resulting in amorphous structures originating from the competition of multiple fitting geometries. If Ω is too small (too specific), the probability that two particles in close proximity are properly aligned to interact becomes negligible, and the system is found in a gas phase unless a very large interparticle energy E is provided, which in turn drives the system into a gel phase.

Analogous arguments can be made for the overall strength of the interaction that, for a reasonable patch size, should be neither too strong nor too weak. The net result is that self-assembly is a very elusive process that requires a careful design and

fine tuning of the interparticle interactions, and typically the target region in the interaction space is quite narrow.

Our interest is in the problem of “reverse self-assembly,” in analogy to the problem of “reverse protein folding” in which protein sequences are designed to yield a desired ground-state folded structure [139, 140]. The problem can be formulated as follows: given an arbitrary final structure, is there an efficient method by which interparticle interactions may be designed so that the particles spontaneously self-assemble into the given structure?

In this chapter we use simple physical arguments to develop a numerical procedure capable of sampling the space of interactions, in terms of both patch geometry and binding energy, to generate nanoparticle interactions leading to self-assembly of desired crystal structures. Without loss of generality, we limit our discussion to spherical particles interacting via anisotropic short-range attractive pair potentials mimicking the hydrophobic interactions, such as those used in Chapter 2, driving self-assembly of Janus particles [16, 26].

Classical nucleation theory provides a simple framework within which to think about crystal formation. Recall from Section 1.2.1 that the free energy ΔG associated with crystal nucleation is given by

$$\Delta G \simeq \frac{4}{3}\pi r^3 \rho \Delta\mu + 4\pi r^2 \gamma. \quad (6.1)$$

This leads to the critical nucleus size, $n^* = \frac{32\pi}{3\rho} \left(\frac{\gamma}{|\Delta\mu|} \right)^3$, above which the crystal will grow until the phase transition is completed and below which the crystal will vanish. Thus, we have a curve as illustrated in Figure 1.2, where the maximum in ΔG (and thus the point where $\frac{d\Delta G}{dn} = 0$) occurs at that point n^* .

We argue that a successful strategy for crystal design should take into account the physical properties of the parent fluid phase, and our working hypothesis is that the free energy of crystal nucleation can be exploited to design interactions to target arbitrary crystal structures. The main idea is to force a crystal nucleus of desired symmetry to be in contact with its own fluid and use a numerical procedure to select

for those interactions between the particles that minimize the free energy cost required to hold that nucleus in place. Our scheme consists of two parts: 1) we determine the optimal shape of the hydrophobic regions (Ω) satisfying the condition stated above, and 2) given Ω , we find the interaction strength (E) for which the system is likely to nucleate into the target (defect-free) crystal phase.

6.2 Sampling the interaction shape Ω

Consider a system of N identical particles with a given interparticle potential $U(\Omega_i, r)$, where Ω_i is the interaction shape (which will be kept to a very general definition at this point) and r is the interparticle distance, set in a volume V . Define an order parameter q capable of detecting the symmetry of the desired crystal phase (an example of such an order parameter for fcc crystals is described in Section 1.4.1; other order parameters are described below).

Grow from the fluid and equilibrate a crystalline nucleus of size n_0 using a standard biased Monte Carlo method targeting the size of the largest crystalline cluster in the system, n , via a potential [24]

$$V_B(n) = \frac{\kappa}{2}(n - n_0)^2. \quad (6.2)$$

Set the binding energy among the particles to a sufficiently small value to ensure that the nucleus melts once the bias is removed, and compute from a full, but short, simulation in the presence of the bias the average crystal size $\bar{n}(\Omega_i)$.

Now define a (fictitious) design potential

$$V_D[\bar{n}(\Omega_i)] = -\alpha \bar{n}(\Omega_i), \quad (6.3)$$

where α is a numerical constant. At this point the idea is to sample over the space of interactions using V_D as a driving force. Specifically, we generate an alternative (trial) shape for the interaction between any two particles in the system $\Omega_j = \Omega_i + \Delta\Omega$ and repeat the previous steps to obtain a new estimate for $V_D[\bar{n}(\Omega_j)]$. Ω_j is accepted

or rejected based on a standard Metropolis criterion, thus ensuring that the Ω will be driven towards values that maximize the size \bar{n} . Because the interaction energy has been set in such a way that the thermodynamic force on the system is in the direction of melting the crystal, maximization of \bar{n} is equivalent to minimization of the load requested of the bias to hold the crystal in place.

6.3 Sampling the interaction strength E

Unfortunately, our method does not allow easy measurement of the height of the nucleation barrier given an interaction strength E . This is mostly because the surface tension between the crystal and the fluid phase is unknown. Nevertheless, we have direct access to the slope of the free energy barrier.

Therefore, although one cannot design the system to comply with a specific nucleation rate ν , by modulating E one can design the size of the critical nucleus n^* . A critical nucleus that is too small will result in the almost instantaneous nucleation of several crystallites that will form defects and grain boundaries as they meet while growing. The opposite scenario will lead to absence of crystallization within the experimental time frame. For the systems we have examined, we find that $15 \lesssim n^* \lesssim 30$ results in nucleation events that are quick, yet sufficiently rare to prevent formation of multiple crystals. The choice of n^* may require a few iterations depending on the details and the size of the system.

The strategy behind the design of the critical nucleus size is analogous to that described in the previous case, except that the design potential in this case has a harmonic functional form defined as

$$V_D[\bar{n}(E_i)] = \alpha(\bar{n}(E_i) - n^*)^2, \quad (6.4)$$

and we sample over the interaction strength E . Minimizing V_D implies that the system will be driven towards that value of E (defined as E^*) for which the nucleus has the same probability of growing or shrinking, yielding, on average, $\bar{n}(E_i) = n^*$.

This condition guarantees that the system is at the top of the nucleation free energy barrier, since to either side of the critical point there is a definite direction in which the value of \bar{n} will move. Thus, n^* has indeed become the critical nucleus by definition.

Note that in principle, the interaction geometry could have an arbitrary number of parameters that could all be optimized simultaneously; however, it is crucial that the optimization of the geometry precedes the optimization of the strength of the potential. The algorithm for the optimization of interaction geometry relies upon the nucleus being precritical; otherwise, it will be completely ineffective.

6.4 Numerical tests

As a proof of concept for our method we consider the design of two distinct crystal structures for which we can guess the solution in the interaction space and know how to define an order parameter q : a simple cubic crystal (SC) and a two dimensional sheet with square symmetry embedded in a three dimensional environment (2SQ).

For both systems we adopt the Kern-Frenkel model [131]. Particles are described as hard spheres of diameter σ interacting via a short-range attractive interaction that is turned on whenever hydrophobic regions (the patches) on different particles face each other. For each pair of particles i and j with patch indices α and β , the interaction is defined as

$$u(\mathbf{r}_{ij}) = u_{\text{SW}}(r_{ij}) \sum_{\alpha,\beta} f^{\alpha\beta}(\Theta_{ij}), \quad (6.5)$$

where $u_{\text{SW}}(r_{ij})$ is a standard attractive isotropic square well potential of depth ε and range 1.15σ , and $f^{\alpha\beta}(\Theta_{ij})$ depends on the particles' mutual orientations and is defined as

$$f^{\alpha\beta}(\Theta_{ij}) = \begin{cases} 1 & \text{if } \begin{cases} \mathbf{r}_{ij} \cdot \mathbf{e}_\alpha > \cos \theta \\ \text{and } \mathbf{r}_{ji} \cdot \mathbf{e}_\beta > \cos \theta \end{cases} \\ 0 & \text{otherwise} \end{cases}. \quad (6.6)$$

Here θ is the angular size of the hydrophobic regions (selected to be all identical in size and circular in shape), \mathbf{r}_{ij} is the unit vector along the direction of the interparticle separation, and \mathbf{e}_α is the unit vector connecting the center of a particle to the center of the patch α on its surface.

In these simple systems θ and ε are the design parameters we need to tune for self-assembly to take place. All simulations are performed in the NVT ensemble using a minimum of 256 particles in a box with periodic boundary conditions. A good order parameter to detect SC crystals is the standard local bond order based on spherical harmonics, \bar{q}_4 ; that is, q_l from Section 1.4.1, where $l = 4$ for the detection of crystals of four-fold symmetry. A particle i is tagged as crystalline if \bar{q}_4 is greater than a chosen cutoff, q_{cut} – the sensitivity of the technique to the choice of order parameter is discussed in Section 6.5.

For the 2SQ case we used \bar{q}_4 with the added constraint that a particle must have interactions with no more than four neighbors in order to be considered “crystalline.” The location of the patches – or, in particular, the absence of patches on the “poles” of the particles – automatically prevents the formation of SC crystals in this case. The insets in Figure 6.2 sketch the patch positions over the particles.

Figures 6.2a and 6.2b illustrate how the force $F(\theta) = -\kappa(n - n_0)$ required to hold a nucleus of n_0 particles immersed in its fluid phase depends on the size of the circular regions θ for the SC and the 2SQ crystals, respectively.

The corresponding simulations were performed at densities of $\rho_{SC} = 0.1$ and $\rho_{2SQ} = 0.01$, binding strength $\varepsilon_{SC} = 3.5k_B T$ and $\varepsilon_{2SQ} = 5.75k_B T$, and a harmonic bias potential of spring constant $k_{SC} \simeq 0.2k_B T$ and $k_{2SQ} = 0.4k_B T$. Clearly, $F(\theta)$ is a sufficiently sensitive parameter to discriminate among the different angular sizes, and presents in both cases a distinct optimal value; $\theta_{SC}^* \simeq 22^\circ$ and $\theta_{2SQ}^* \simeq 20^\circ$. Figure 6.2a also shows that the optimal value is fairly independent of the particular average size n_0 of the nucleus held in contact with the fluid. Figure 6.3 shows how the location of θ^* and ε^* can be obtained automatically by using the Monte Carlo scheme in the

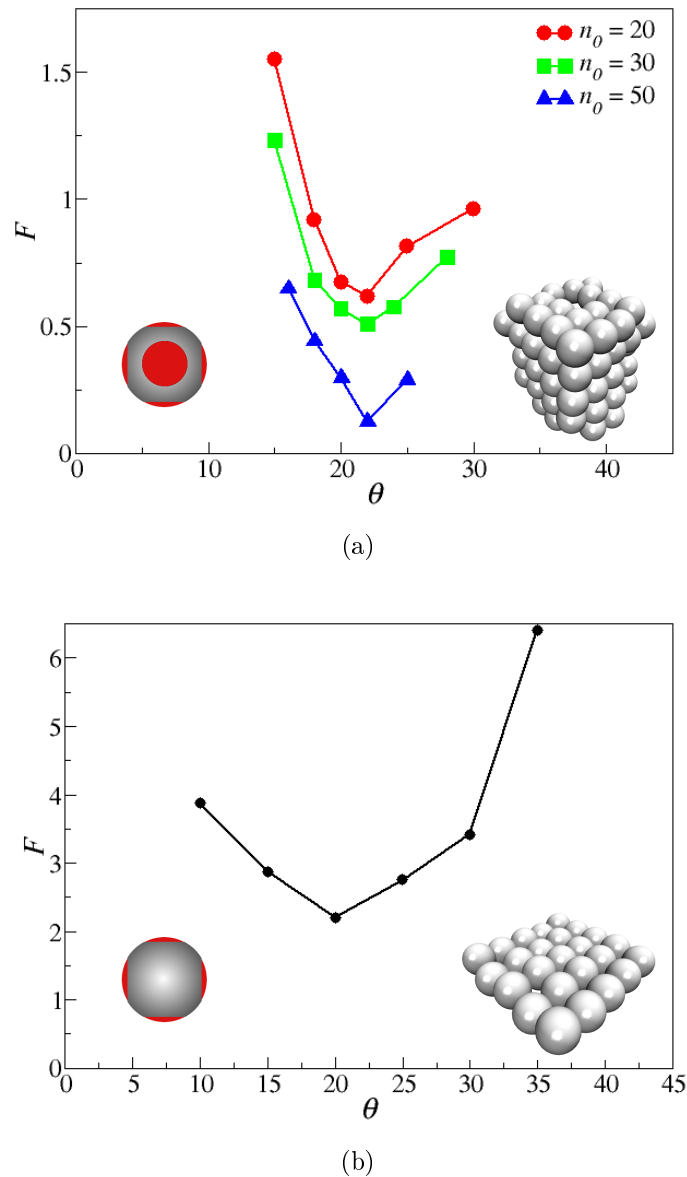


Figure 6.2: Force vs. θ for (a) SC and (b) 2SQ crystals. The insets show snapshots of the target crystals, and sketches of the locations of the patches in our particle model. In (a), the different lines represent data obtained by imposing different nucleus sizes n_0 as indicated in the legend.

space of interactions, using $n^* = 20$.

It should be stressed that the minimization of $V_D[\bar{n}(\Omega_i)]$ can be achieved using any minimization algorithm; nevertheless, we find that the Monte Carlo scheme allows us to use shorter simulations, for each trial θ_i , than would be necessary for other direct minimization schemes. The reason is related to the precision of the estimate of \bar{n} for relatively short trajectories, which could be over- or underestimated. This could lead to fictitious local minima, which could trap a direct minimization scheme, but are easily overcome with a standard Monte Carlo method.

In order to check our method, $\varepsilon - \theta$ phase diagrams were constructed using the traditional, “forward” method of trial-and-error, running Monte Carlo simulations for 10^7 steps and determining whether crystallization into the desired structure occurred using the order parameters discussed above as well as direct inspection. As shown in Figure 6.4, the parameters detected by our methods are within the crystallization regions for the two target crystals. Unsurprisingly, the result falls roughly to the high- θ , low- ε edge of the crystallization region; recall that θ was selected using a value of ε too low for crystallization, which would be expected to result in a larger θ (note the roughly inverse $\varepsilon - \theta$ relationship in Figure 6.4); ε was then selected using the θ found in the first step.

6.5 Limitations

It is important to discuss the limitations of the method. First of all, in its actual formulation, our method only works for systems that will self-assemble into an infinitely large aggregate via the process of nucleation. It is not obvious how to generalize it to include self-assembly into finite size aggregates such as, for instance, viral capsids, although this is obviously a regime in which such design would be very desirable.

The second limitation is that although the method provides a solution to the reverse self-assembly problem, there is no guarantee that the solution is the optimal

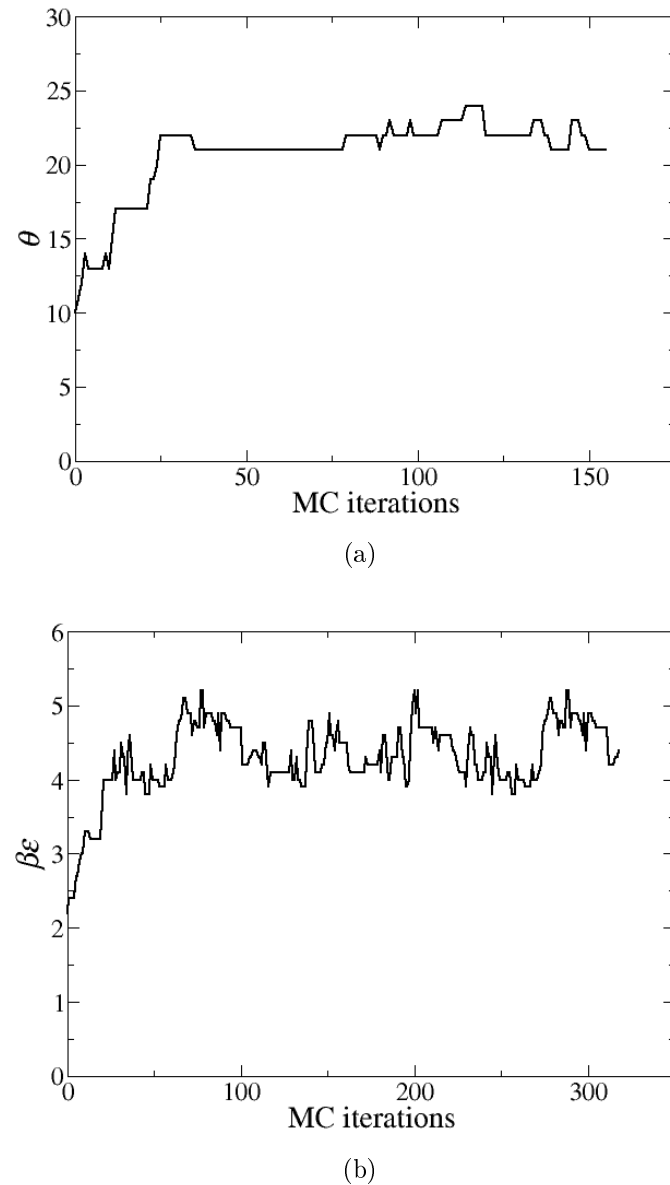


Figure 6.3: Monte Carlo trajectories in the space of interactions for the design of the simple cubic crystal. In (a) the shape of the patches defined by the solid angle θ is allowed to fluctuate while keeping the strength of the interaction ε constant. In (b) ε fluctuates while keeping θ constant and at the optimal value found in (a).

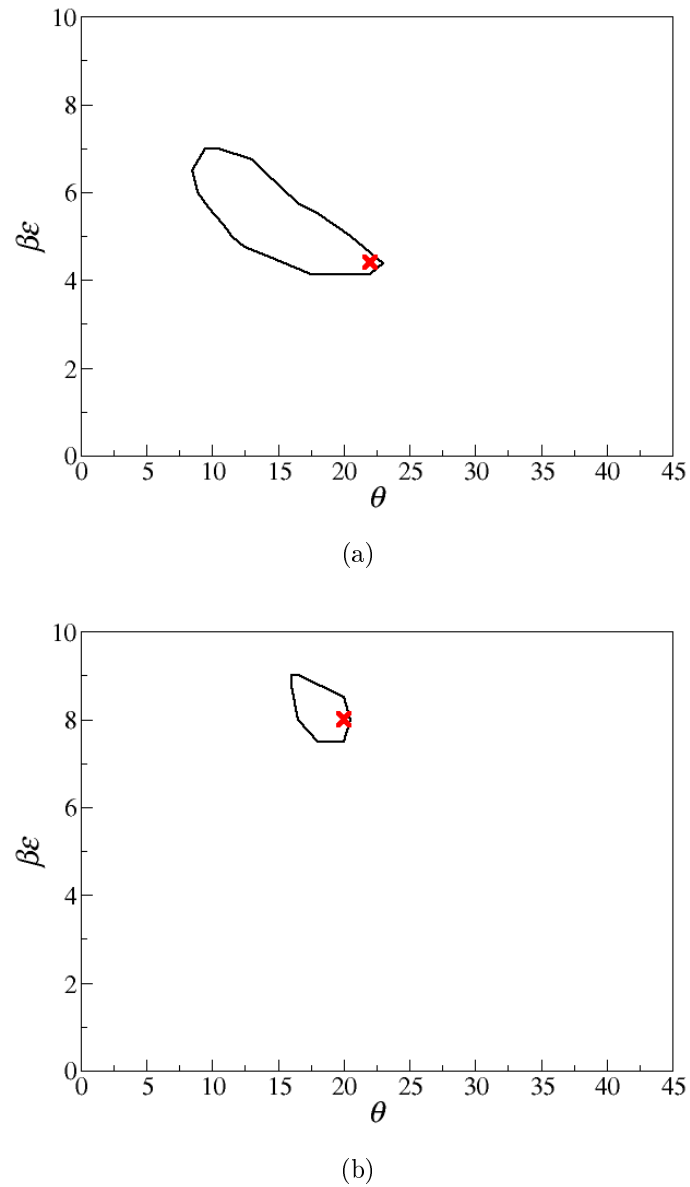


Figure 6.4: Phase diagrams for (a) SC and (b) 2SQ crystals. Lines show the border around the phase region in which particle form the desired crystal; the points marked by an ‘X’ are the $(\theta, \beta\varepsilon)$ combinations found to be optimal by our method.

one. This is because our method forces the nucleation process to follow the classical route, i.e. the forming nucleus has the same structure as the target crystal; however, there are several examples [22, 138, 141, 142] where the nucleation barrier may be lowered by following a more complex dynamical pathway that may include metastable states having different symmetry than that of the target crystal – Chapter 2 clearly illustrates this principle for asymmetric Janus particles. For instance, it is possible to imagine that the formation of the SC crystal could benefit from an additional weak, non-specific, isotropic interaction, on top of that provided by the patches, that may initially lead the system into a high-density metastable fluid phase from which nucleation into the final structure may proceed at a faster rate than that predicted otherwise (analogous to the dense fluid aggregates that formed in Chapter 2 from which fcc crystals nucleated).

Finally, it is crucial to develop a good order parameter q to describe the desired crystal structure. Figure 6.5 illustrates how an inefficient order parameter may lead to fictitious minimization in the space of interactions while designing the 2SQ crystal. The different lines in the F vs. θ diagram represent different values of q_{cut} (defining how restrictive the order parameter is) from 0.8 to 0.99.

We find that a cutoff in the order parameter of at least 0.97 is required to adequately distinguish between the square and hexagonal symmetries for large values of θ . The curves related to the less restrictive order parameters would in fact misleadingly indicate a flatter bottom of the curve, while in reality we find that any angle larger than $\sim 25^\circ$ will lead to nucleation into a two-dimensional crystal with hexagonal symmetry. Adding an energy penalty to prevent arrangements compatible with the competing six-fold symmetry (apart from imposing a limit to the number of neighbors), using an order parameter such as the familiar \bar{q}_6 , may also be considered as a means of improving the design procedure.

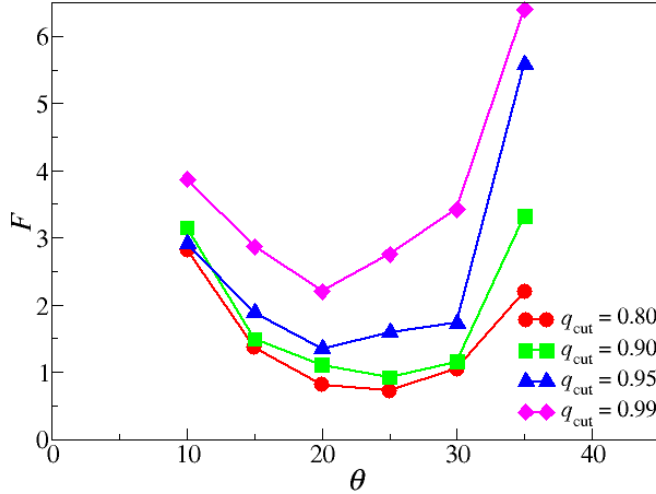


Figure 6.5: F vs. θ diagrams. The dependence of the method on the order parameter used. Different curves correspond to different values of the cutoff q_{cut} .

6.6 Beyond the Kern-Frenkel model

Here we propose a more general model to describe interparticle interactions that we name the *Adaptive Pixel Model*. The idea stems from the need to devise a way of sampling over different geometric patterns (beyond circular) in search of those which can efficiently hold the single components into a desired target structure. The first step is the discretization of the surface of the particle.

For spherical building blocks, we cover the surface of each particle with a large number, N_p , of regularly-spaced interaction sites (pixels) as illustrated in Figure 6.6. A good arrangement of the pixels can be obtained by using the spherical triangulation provided by an (n, m) delta-icosahedron [143], and N_p is selected depending on the complexity of the target structure. Euler's theorem imposes the following constraint on N_p : $N_p = 10(n^2 + nm + m^2) + 2$ [143], where n and m indicate that one has to move n pixels along the row of neighboring bonds on the sphere, and then after a turn of 120° , move for m extra pixels.

In the simplest version of the model, to each pixel k on a particle i is assigned

a variable s_i^k which has a binary character, $s_i^k \in \{1, 0\}$ depending on whether that interaction site is switched *on* or *off*. Whenever two particles i and j are within a given distance of each other, the axis between them, \mathbf{r}_{ij} , is calculated. If the nearest digit to the point where \mathbf{r}_{ij} crosses the surface of each particle is *on*, then the particles feel an overall short-range attractive interaction.

Pixels on the same particle do not interact with each other. The interaction pair potential between any two particles, i and j , of diameter σ , set at a distance r_{ij} from each other, then takes the form

$$V(r_{ij}) = V_{\text{HS}} + \begin{cases} -s_i^k s_j^l \varepsilon & \text{if } |r_{ij}| \leq r_0 \\ 0 & \text{otherwise} \end{cases}, \quad (6.7)$$

where s_i^k and s_j^l are the binary variables corresponding to the digits intersected by r_{ij} on particles i and j , respectively, as described above. Excluded volume between the particles is enforced via a standard hard-sphere potential, V_{HS} .

The main advantage of this setup is that once particles are held into place at given positions, the geometry of the interacting regions emerges as a result of a simple Monte Carlo simulation on s_i^k which samples different states according to Equation 6.7. Such a simulation is analogous to the simulation of a simple Ising model, but in which the energy depends not on the neighboring pixels on the same particle but on pixels on neighboring particles.

Crucial to the efficiency of the model is the independence of the interaction strength of the total area of the attracting region. This condition, also assumed in the Kern-Frenkel model, is appropriate when considering interactions that have a range of action that is small compared to the colloidal diameter ($(r_0 - \sigma) \lesssim 0.15\sigma$), and allows us to circumvent the overwhelming cost related to the computation of the N_k^2 distances between the pixels.

Furthermore, as the relative distances of on-particle pixels are frozen and only active pixels need to be tracked, it is possible to perform the search of the nearest pixel to any point on the sphere very efficiently. This is achieved by creating a cell

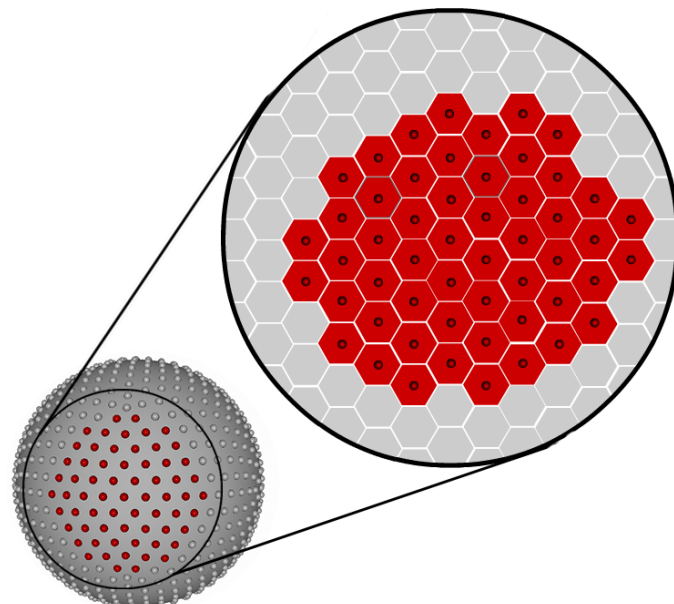


Figure 6.6: Illustration of the structure of the *Adaptive Pixel Model*. *On* pixels are depicted in red while *off* pixels are in gray. The magnification in the top image shows the Voronoi tessellation around the pixels (computed as described in the text). The effective geometry of the active sites in this representation is a hexagon.

list over the spherical particle surface in θ and ϕ (the spherical coordinates), and by associating with each cell the identity of the nearest pixel. This is equivalent to generating a discrete Voronoi tessellation [143] of the spherical surface based on the pixel locations (see sketch in Figure 6.6), which needs to be performed only once at the beginning of the simulation. Any shape for the interaction regions can be achieved by simply switching *on* or *off* pixels or groups of pixels.

6.7 Conclusions

In this chapter we have proposed a simple two-step method for the problem of reverse self-assembly. The idea is to exploit the curvature of the nucleation free-energy barrier to sample and select optimal interparticle interactions for self-assembly into a target structure. Numerical simulations have been presented to test the efficacy of our method, as well as detailed discussion of its limitations and its potential. These simulations show that our method reduces the time to solve the problem of determining optimal interaction parameter from on the order of weeks (for trial-and-error approaches) to hours.

Finally, we proposed a new model, the *Adaptive Pixel Model*, by which almost any interaction geometry can be realized in a simple and efficient way. It should be stressed that our method is not limited to spherical particles but can be applied to any particle shape; in principle, particle shape could be introduced as a new parameter in the interaction space and be sampled over using the scheme proposed in this paper.

Although our method does not capture the dynamical subtleties of the crystal formation process, it does provide a very efficient way of screening over a large number of given interaction geometries that can be mapped onto the pixels. Efficient ways of sampling the interaction space could be obtained using genetic algorithms that can be used to evolve optimal interaction patterns given a set of initial shapes.

References

- [1] D. Frenkel, *Nature Mater.* **5**, 85 (2006).
- [2] G. A. DeVries *et al.*, *Science* **315**, 358 (2007).
- [3] M. Li, H. Schnablegger, and S. Mann, *Nature* **402**, 393 (1999).
- [4] L. Hong, S. Jiang, and S. Granick, *Langmuir* **22**, 9495 (2006).
- [5] H. Weller, *Phil. Trans. R. Soc. A* **361**, 229 (2003).
- [6] E. K. Hobbie *et al.*, *Langmuir* **21**, 10284 (2005).
- [7] J. W. Kim, R. J. Larsen, and D. A. Weitz, *Adv. Mater.* **19**, 2005 (2007).
- [8] Y.-S. Cho *et al.*, *Chem. Mater.* **17**, 5006 (2005).
- [9] J. A. Champion, Y. K. Katare, and S. Mitragotri, *Proc. Natl. Acad. Sci.* **104**, 11901 (2007).
- [10] B. M. Mladek, G. Kahl, and C. N. Likos, *Phys. Rev. Lett.* **100**, 028301 (2008).
- [11] J. N. Israelachvili, D. J. Mitchell, and B. W. Ninham, *J. Chem. Soc., Faraday Trans. 2* **72**, 1525 (1976).
- [12] T. Hu, R. Zhang, and B. I. Schovskii, *Physica A* **387**, 3059 (2008).
- [13] D. Leckband and J. Israelachvili, *Quart. Rev. Biophys.* **34**, 105 (2001).

- [14] R. Nagarajan and E. Ruckenstein, *Langmuir* **7**, 2934 (1991).
- [15] C. A. Iacovella, M. A. Horsch, and S. C. Glotzer, *J. Chem. Phys.* **129**, 044902 (2008).
- [16] L. Hong *et al.*, *Langmuir* **24**, 621 (2008).
- [17] W. W. Wood and J. D. Jacobson, *J. Chem. Phys.* **27**, 1207 (1957).
- [18] B. J. Alder and T. E. Wainwright, *J. Chem. Phys.* **27**, 1208 (1957).
- [19] S. Auer, *Quantitative Prediction of Crystal Nucleation Rates for Spherical Colloids: A Computational Study*, Ph.D. thesis, Universiteit van Amsterdam (2002).
- [20] S. C. Glotzer and M. J. Solomon, *Nature Mater.* **6**, 557 (2007).
- [21] P. J. Steinhardt, D. R. Nelson, and M. Ronchetti, *Phys. Rev. B* **28**, 784 (1983).
- [22] P. R. ten Wolde and D. Frenkel, *Science* **277**, 1975 (1997).
- [23] S. Auer and D. Frenkel, *Annu. Rev. Phys. Chem.* **55**, 333 (2004).
- [24] P. R. ten Wolde, M. J. Ruiz-Montero, and D. Frenkel, *J. Chem. Phys.* **104**, 9932 (1996).
- [25] D. Frenkel and B. Smit, *Understanding Molecular Simulation: From Algorithms to Applications*, 2nd ed. (Academic Press, San Diego, 2002).
- [26] W. L. Miller and A. Cacciuto, *Phys. Rev. E* **80**, 021404 (2009).
- [27] W. L. Miller, B. Bozorgui, and A. Cacciuto, *J. Chem. Phys.* **132**, 134901 (2010).
- [28] W. L. Miller and A. Cacciuto, *J. Chem. Phys.* **133**, 234903 (2010).
- [29] W. L. Miller and A. Cacciuto, *Soft Matter* **7**, 7552 (2011).

- [30] W. L. Miller *et al.*, J. Chem. Phys. **135**, 244902 (2011).
- [31] W. L. Miller and A. Cacciuto, J. Chem. Phys. **133**, 134901 (2010).
- [32] B. Alberts *et al.*, *Molecular Biology of the Cell*, 5th ed. (Garland Science, New York & Oxford, 2008).
- [33] F. H. C. Crick and J. D. Watson, Nature **177**, 473 (1956).
- [34] A. Klug and D. L. D. Caspar, Adv. Virus Res. **7**, 225 (1961).
- [35] E. Sackmann, Can. J. Phys. **68**, 999 (1990).
- [36] G. Subramanian *et al.*, Adv. Mater. **11**, 1261 (1999).
- [37] H. Liu, , *et al.*, J. Chem. Phys. **130**, 174501 (2009).
- [38] M. F. Hagan and D. Chandler, Biophys. J. **91**, 42 (2006).
- [39] S. Whitelam and P. L. Geissler, J. Chem. Phys. **127**, 154101 (2007).
- [40] A. W. Wilber *et al.*, J. Chem. Phys. **127**, 085106 (2007).
- [41] T. Chen, Z. Zhang, and S. C. Glotzer, Proc. Natl. Acad. Sci. **104**, 717 (2007).
- [42] T. Chen, Z. L. Zhang, and S. C. Glotzer, Langmuir **23**, 6598 (2007).
- [43] W. Z. Ostwald, Phys. Chem. **22**, 289 (1879).
- [44] F. Sciortino, private communication (2009).
- [45] J. Kepler, *The Six-Cornered Snowflake: A New Year's Gift*, 1st ed. (Paul Dry Books, Philadelphia, 2010) (originally published 1611; translated from the Latin by Jacques Bromberg).
- [46] T. C. Hales, Annals of Mathematics **162**, 1063 (2005).
- [47] S. Auer and D. Frenkel, Nature **409**, 1020 (2001).

- [48] S. Auer and D. Frenkel, *Nature* **413**, 711 (2001).
- [49] E. Zaccarelli *et al.*, *Phys. Rev. Lett.* **103**, 135704 (2009).
- [50] S. Torquato, *Soft Matter* **5**, 1157 (2009).
- [51] P. Bolhuis and D. Frenkel, *J. Chem. Phys.* **106**, 666 (1997).
- [52] X. Zhang, Z. L. Zhang, and S. C. Glotzer, *J. Phys. Chem. C* **111**, 4132 (2007).
- [53] B. S. John and F. A. Escobedo, *J. Phys. Chem. B* **109**, 23008 (2005).
- [54] P.-G. de Gennes, *Scaling Concepts in Polymer Physics* (Cornell University Press, Ithaca, NY, 1979).
- [55] F. Rosenberger, *J. Crystal Growth* **166**, 40 (1996).
- [56] J. C. Pámies, A. Cacciuto, and D. Frenkel, *J. Chem. Phys.* **131**, 044514 (2009).
- [57] B. Capone *et al.*, *J. Phys. Chem. B* **113**, 3629 (2008).
- [58] C. N. Likos *et al.*, *Phys. Rev. Lett.* **80**, 4450 (1998).
- [59] B. Bozorgui *et al.*, *J. Chem. Phys.* **132**, 014901 (2010).
- [60] M. C. Powers, *J. Sediment Petrol.* **23**, 117 (1953).
- [61] J. Rudnick and G. Gaspari, *J. Phys. A: Math. Gen.* **19**, L191 (1986).
- [62] C. Vega, E. Sanz, J. L. F. Abascal, and E. G. Noya, *J. Phys.: Condens. Matter* **20**, 153101 (2008).
- [63] W. G. Hoover and F. H. Ree, *J. Chem. Phys.* **49**, 3609 (1968).
- [64] M. Marechal and M. Dijkstra, *Phys. Rev. E* **77**, 061405 (2008).
- [65] R. J. Speedy, *Mol. Phys.* **95**, 169 (1998).

- [66] M. Tripathy and K. S. Schweitzer, J. Chem. Phys. **130**, 244907 (2009).
- [67] M. Glaser *et al.*, Europhysics Lett. **78**, 46004 (2007).
- [68] A. A. Louis *et al.*, Phys. Rev. Lett. **85**, 2522 (2000).
- [69] I. O. Götze, H. M. Harreis, and C. N. Likos, J. Chem. Phys. **120**, 7761 (2004).
- [70] A. Jusufi, C. N. Likos, and H. Löwen, Phys. Rev. Lett. **88**, 018301 (2002).
- [71] A. R. Denton, Phys. Rev. E **67**, 11804 (2003).
- [72] D. Gottwald *et al.*, Phys. Rev. Lett. **92**, 68301 (2004).
- [73] C. Pierleoni *et al.*, Phys. Rev. Lett. **96**, 128302 (2006).
- [74] C. Zhao, K. Tian, and N. Xu, Phys. Rev. Lett. **106**, 125503 (2011).
- [75] S. Prestipino, F. Saija, and G. Malescio, Soft Matter **5**, 2795 (2009).
- [76] B. M. Mladek *et al.*, Phys. Rev. Lett. **96**, 045701 (2006).
- [77] A. Sütő, Phys. Rev. B **74**, 104117 (2006).
- [78] C. N. Likos, Nature **440**, 433 (2006).
- [79] J. C. Pàmies, A. Cacciuto, and D. Frenkel, J. Chem. Phys. **131**, 044514 (2009).
- [80] C. N. Likos *et al.*, Phys. Rev. E **63**, 031206 (2001).
- [81] C. N. Likos, Soft Matter **2**, 478 (2006).
- [82] G. Malescio and G. Pellicane, Nature Mater. **2**, 97 (2003).
- [83] G. Stell and P. C. Hemmer, J. Chem. Phys. **56**, 4274 (1970).
- [84] E. A. Jagla, Phys. Rev. E **58**, 1478 (1998).
- [85] M. Glaser, private communication (2011).

- [86] A. Šarić, B. Bozorgui, and A. Cacciuto, J. Phys. Chem. B **8**, 1 (2011).
- [87] K. Binder, S. Sengupta, and P. Nielaba, J. Phys.: Condens. Matter **14**, 2323 (2002).
- [88] K. Zhang, P. Charbonneau, and B. Mladek, Phys. Rev. Lett. **105**, 245701 (2010).
- [89] E. L. Altschuler *et al.*, Phys. Rev. Lett. **72**, 2671 (1994).
- [90] T. Erber and G. M. Hockney, Phys. Rev. Lett. **74**, 1482 (1995).
- [91] A. Pérez-Garrido *et al.*, J. Phys. A: Math. Gen. **29**, 1973 (1996).
- [92] J. R. Morris, D. M. Deaven, and K. M. Ho, Phys. Rev. B **53**, R1740 (1996).
- [93] T. Erber and G. M. Hockney, “Complex systems: Equilibrium configurations of n equal charges on a sphere ($2 \leq n \leq 112$),” in *Advances in Chemical Physics* (John Wiley & Sons, Inc., 2007) pp. 495–594.
- [94] J. R. Edmundson, Acta Cryst. **A49**, 648 (1993).
- [95] E. L. Altschuler *et al.*, Phys. Rev. Lett. **78**, 2681 (1997).
- [96] M. J. W. Dodgson and M. A. Moore, Phys. Rev. B **55**, 3816 (1997).
- [97] A. Pérez-Garrido *et al.*, Phys. Rev. Lett. **79**, 1417 (1997).
- [98] A. Pérez-Garrido, M. J. W. Dodgson, and M. A. Moore, Phys. Rev. B **56**, 3640 (1997).
- [99] M. J. Bowick *et al.*, Phys. Rev. B **73**, 024115 (2006).
- [100] M. Bowick *et al.*, Phys. Rev. Lett. **89**, 185502 (2002).
- [101] J. J. Thomson, Philos. Mag. **7**, 237 (1904).

- [102] M. J. Bowick, D. R. Nelson, and A. Travesset, Phys. Rev. B **62**, 8738 (2000).
- [103] A. R. Bausch *et al.*, Science **299**, 1716 (2003).
- [104] D. H. Napper, *Polymeric Stabilization of Colloidal Dispersions* (Academic Press, London, 1983).
- [105] E. S. Dragan, ed., *New trends in ionic (Co)polymers and hybrids* (Nova Science, New York, 2007).
- [106] R. C. Advincula, W. J. Brittain, and K. C. Caster, eds., *Polymer Brushes* (Wiley-VCH, Weinheim, 2004).
- [107] P. Somasundaran, ed., *Polymer Brushes: Applications in Biotechnology* (Taylor & Francis, 2006).
- [108] M. A. C. Stuart *et al.*, Nature Materials **9**, 101 (2010).
- [109] S. T. Milner, Science **251**, 905 (1991).
- [110] K. Binder, ed., *Monte Carlo and Molecular Dynamics Simulations in Polymer Science* (Oxford University Press, 1995).
- [111] M. Daoud and J. P. Cotton, J. Phys. (Paris) **43**, 531 (1982).
- [112] S. Alexander, J. Phys. (Paris) **38**, 983 (1977).
- [113] A. Halperin, M. Tirrell, and T. P. Lodge, Adv. Polym. Sci. **100**, 31 (1992).
- [114] S. T. Milner, T. A. Witten, and M. E. Cates, Macromolecules **21**, 2610 (1988).
- [115] C. M. Wijmans and E. B. Zhulina, Macromolecules **26**, 7214 (1993).
- [116] C. Biver, R. Hariharan, J. Mays, and W. B. Russel, Macromolecules **30**, 1787 (1997).
- [117] D. Dimitrov, A. Milchev, and K. Binder, Macromol. Symp. **252**, 47 (2007).

- [118] A. G. Koutsoubas and A. G. Vanakaras, *Langmuir* **24**, 13717 (2008).
- [119] M. Patra and P. Linse, *Nano Lett.* **6**, 133 (2006).
- [120] A. M. Jackson, J. W. Myerson, and F. Stellacci, *Nature Materials* **3**, 330 (2004).
- [121] C. Singh *et al.*, *Physical Review Letters* **99**, 226106 (2007).
- [122] J. J. Kuna *et al.*, *Nature Materials* **8**, 837 (2009).
- [123] R. P. Carney *et al.*, *J. Am. Chem. Soc.* **139**, 798 (2008).
- [124] C. Singh, A. M. Jackson, F. Stellacci, and S. C. Glotzer, *J. Am. Chem. Soc.* **131**, 16377 (2009).
- [125] R. C. Van Lehn and A. Alexander-Katz, *J. Chem. Phys.* **135**, 141106 (2011).
- [126] N. Ayres, *Poly. Chem.* **1**, 769 (2010).
- [127] A. Santos, C. Singh, and S. C. Glotzer, *Physical Review E* **81**, 011113 (2010).
- [128] C. Singh *et al.*, *Nanoscale* **3**, 3244 (2011).
- [129] S. J. Plimpton, *J. Comp. Phys.* **117**, 1 (1995).
- [130] C. Hiergeist and R. Lipowsky, *J. Phys. II (France)* **6**, 1465 (1996).
- [131] N. Kern and D. Frenkel, *J. Chem. Phys.* **118**, 9882 (2003).
- [132] H. Liu *et al.*, *J. Chem. Phys.* **130**, 044902 (2009).
- [133] E. Zaccarelli, F. Sciortino, and P. Tartaglia, *J. Chem. Phys.* **127**, 174501 (2007).
- [134] C. Mayer *et al.*, *J. Phys.: Condens. Matter* **22**, 104110 (2010).
- [135] E. Jankowski and S. C. Glotzer, *J. Chem. Phys.* **131**, 104104 (2009).
- [136] E. Jankowski and S. C. Glotzer, *J. Phys. Chem. B* **115**, 14321 (2011).

- [137] S. Hormoz and M. P. Brenner, Proc. Natl. Acad. Sci. **108**, 5193 (2011).
- [138] S. Whitelam, J. Chem. Phys. **132**, 194901 (2010).
- [139] K. Yue and K. A. Dill, Proc. Natl. Acad. Sci. **89**, 4163 (1992).
- [140] J. M. Deutsch and T. Kurosaki, Phys. Rev. Lett. **76**, 323 (1996).
- [141] A. Cacciuto, S. Auer, and D. Frenkel, Phys. Rev. Lett. **93**, 166105 (2004).
- [142] H. Liu, S. K. Kumar, and J. F. Douglas, Phys. Rev. Lett. **103**, 018101 (2009).
- [143] H. M. S. Coxeter, *Introduction to Geometry* (Wiley, New York, 1969).